# POLITECNICO DI MILANO

Scuola di Ingegneria dei Processi Industriali

Corso di Laurea in
Ingegneria Nucleare


Vibrational characterization of nanostructured films
by Brillouin spectroscopy

Relatore: Prof. Marco G. BEGHI
Correlatore: Ing. Fabio Di FONZO

Tesi di laurea di:
Annacaterina SALERI Matr. 748642

Anno Accademico 2011 - 2012

# General Index

# Index of Figures and Tables

# Abstract

Brillouin spectroscopy (BS) is an established optical, contact-less and non-destructive technique which provides a full elastic characterization of both bulk materials and thin films. This technique measures acoustic excitations at submicrometric wavelengths without requiring sample manipulations. In the present work, the whole process of Brillouin spectroscopy is analysed, from the theory to the experimental set-up and applied to the analysis of nanostructured films of titanum dioxide, produced with PLD (pulse laser deposition) at different pressures. The direct outcome of the measurements is the frequency or the propagation velocity of the vibrational modes supported by the film. The obtained data, recovered as spectra, are analysed from different point of view trying to explain the vibrational behaviour of the material structure, through the comparison to the morphological structure probed with SEM (scanning electron microscopy). BS will prove to be a very sensitive measurement technique able to catch very dissimilar vibrational behaviours even with a strong similarity between the crystallinity and the morphology of the samples investigated. Together with the main physics and morphological characteristics, some practical applications of $TiO_2$ are reported to give an idea of the importance of surface and bulk characterization of materials to reach the precise results required in technological applications.

**Keywords:** Acoustic Waves, Brillouin Spectroscopy, Titanium Dioxide, Film Characterization.

# Estratto

La spettroscopia Brillouin (BS) è una tecnica ottica che misura le eccitazioni ultrasoniche a lunghezze d'onda sub-micrometriche, attraverso lo scattering inelastico di luce laser. Si tratta di una tecnica di misura senza contatto e non distruttiva che viene sfruttata soprattutto per misurare le proprietà elastiche di film sottili omogenei.

I recenti sviluppi nelle tecniche di fabbricazione dei materiali hanno portato alla produzione di vari tipi di film nanostrutturati. L'estrema varietà di morfologie e di proprietà che si possono ottenere sottolinea la necessità di avere a disposizione strumenti di caratterizzazione adeguati. Il biossido di titanio, $TiO_2$, è un materiale particolarmente versatile, che si presta a molteplici applicazioni; alcune di queste possono trarre vantaggio dal fatto di avere a disposizione un film nanostrutturato piuttosto che un film compatto.

Questo lavoro è probabilmente un primo tentativo di sfruttare in maniera sistematica la spettroscopia Brillouin per ottenere la caratterizzazione di film nanostrutturati di biossido di titanio. Questa tecnica risulta essere molto potente, in quanto è in grado di individuare comportamenti vibrazionali significativamente diversi in campioni dotati di morfologia simile, prodotti in condizioni non particolarmente differenti.

I primi due capitoli introducono i fondamenti base della teoria elastica e delle onde elastiche, sia nel caso di mezzi isotropi che anisotropi. Lo scattering Brillouin viene poi descritto in dettaglio nel corso del capitolo 3, insieme al relativo apparato sperimentale. Il capitolo 4 contiene una descrizione generale delle proprietà del biossido di titanio e illustra alcuni esempi delle sue numerose applicazioni, incluse quelle che traggono vantaggio dalla nanostruttura dei film.

Il capitolo 5 presenta in dettaglio la campagna sperimentale, condotta in modo sistematico su due gruppi di campioni di biossido di titanio nanostrutturato prodotti tramite PLD.

I risultati più interessanti derivano dall'analisi degli effetti della pressione di base nella camera di deposizione. L'attenzione si concentra su un intervallo di pressioni abbastanza limitato (da 5 a 15 Pa). La microscopia a scansione

elettronica (SEM) rivela che i film cresciuti a pressioni crescenti presentano morfologie che evolvono in modo progressivo senza differenze particolarmente nette. L'analisi vibrazionale mostra invece forti differenze tra questi campioni: picchi che sono presenti negli spettri ottenuti da campioni ad una certa pressione di deposizione, ma non in altri campioni prodotti a pressioni diverse e, cosa ancora più interessante, picchi che, per diverse pressioni di deposizione, hanno frequenze simili ma una dipendenza diversa dall'angolo di scattering.

Nel capitolo 6 vengono discussi i tentativi fatti per comprendere il comportamento osservato, attribuendo i picchi a possibili modi di vibrazione del film nanostrutturato. Per alcuni sembra essere possibile trovare una descrizione consistente mentre altri rimangono di dubbia attribuzione.

Questo tentativo di utilizzare lo scattering Brillouin per caratterizzare film nanostrutturati mostra come tale tecnica sia uno strumento sensibile, in grado di discriminare comportamenti vibrazionali diversi tra campioni prodotti in condizioni non particolarmente differenti e con simili morfologie. La complessità dei modi vibrazionali nei film nanostrutturati, e le difficoltà riscontrate nel modellizzarli, suggerisce la necessità di uno studio interpretativo più approfondito e apre la strada alla possibilità di ottenere una migliore comprensione delle proprietà caratteristiche di questi film.

# Chapter 1

This first chapter contains some fundamentals concepts that are necessary to have a good comprehension of the physics of elastic wave propagation in solid materials. It is divided into three focus areas. The first part is devoted to the introduction of the theory of elasticity, with the derivation of the relation between stress and strain, especially in the case of isotropic materials. We will take for granted the concepts of displacement vectors and of stress and strain tensors. Then we present the description of the elastic constants and their number, which is different from a material to another, depending on the number of axes and planes of symmetry.

The second part presents the basic equation of elastic wave, derived in a dynamic problem, where a force is applied to a body which generates a displacement and a stress field propagating in the medium with a certain velocity. The two kinds of waves propagating in a medium are introduced, P-waves and S-waves respectively, with their own characteristics velocities. It is also introduced a mathematical tool, the Stokes-Helmholtz decomposition which is very useful in treating the elastic problem especially in the case of a 2-D or 3-D one, which are very difficult to solve directly from Navier's equation of equilibrium, reminded in the first part of the chapter.

The third and last part takes in consideration the phenomena of interaction of light with matter, especially reflection and refraction, whose insertion in this introductive chapter is useful to understand some aspects of Brillouin spectroscopy, which is an optical tecnique with a complex experimental apparatus equiped with many optical devices. We briefly describe these physics phenomena, introducting the laws of reflection and refraction, also known as Snell's law.

## 1.1 Fundamentals of the Theory of Elasticity

In this first part of Chapter 1 we are going to introduce the principal characteristics of elastic materials with a special attention for linear elastic materials. We will derive the relation between stress and strain in the simplest case of linear elastic material, introducing the concept of elastic constants, whose number depends on the symmetry characteristics of the considered material. These concepts turn out to be very important because the central theme of this work is the film characterization of thin films through Brilluoin spectroscopy, which is one of the most used method to obtain en estimation of the elastic properties of solids and so of the elastic constants. We will present Hooke's generalized law and the Navier's equation of equilibrium which are two basic tools needed to understand the elastic problem and the derivation of the equation of elastic waves.

### 1.1.1 Definition of Elastic Material and Stress-Strain Relation

Elastic material can be defined in many ways:

- The material that has one-to-one correspondence between stress and strain.
- The material that follows the same stress-strain path during loading and unloading.
- The material for which the strain energy density function $U_0$ exists and can be expressed in terms of the state of current strain only $U_0 = U_0(\varepsilon_{ij})$, and independent of the strain history.

If the stress-strain relation is linear the material is called linear elastic material. Otherwise it is nonlinear elastic material.

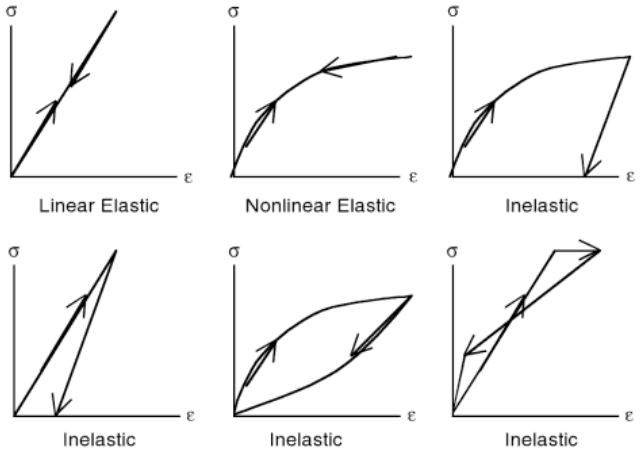


**Fig.1.1** Stress-strain relations for elastic and inelastic material.

If the stress-strain path is different during loading and unloading, then the material is inelastic even if the path is linear.

For elastic materials, the external work done on the material must be equal to the total increase in the strain energy of the material, $\delta W = \delta U$. If we express $\delta U$ in terms of the strain energy density variation $\delta U_0$ and $\delta W$ in terms of the applied body force $f_i$, the surface traction $T_i$ and the variation of displacement $\delta u_i$, thus we can write:

$$\delta U = \int_V \delta U_0 \, dV$$
$$\delta W = \int_V f_i \delta u_i dV + \int_S T_i \, \delta u_i dS \qquad \textbf{(1.1)}$$

From Equation 1.1 one can write

$$\int_V \delta U_0 dV = \int_V f_i \delta u_i dV + \int_S T_i \delta u_i dS = \int_V f_i \delta u_i dV + \int_S \sigma_{ij} n_j \, \delta u_i dS$$
$$= \int_V f_i \, \delta u_i dV + \int_S \, (\sigma_{ij} \delta u_i) n_j dS \qquad \textbf{(1.2)}$$

Applying Gauss' divergence theorem on the surface integral one obtains

$$\int_V \delta U_0 dV = \int_V f_i \delta u_i dV + \int_V (\sigma_{ij}\,\delta u_i)_{,j} dV = \int_V f_i \delta u_i dV + \int_V (\sigma_{ij,j}\,\delta u_i + \sigma_{ij}\,\delta u_{i,j}) dV$$
$$= \int_V ((f_i + \sigma_{ij,j})\,\delta u_i + \sigma_{ij}\delta u_{i,j}) dV \qquad \textbf{(1.3)}$$

After substituting the equilibrium equation[1] , the above equation is simplified and becomes:

$$\int_V \delta U_0 dV = \int_V (\sigma_{ij}\,\delta u_i) n_j dS = \int_V \frac{1}{2}(\sigma_{ij}\delta u_{i,j} + \sigma_{ji}\delta u_{j,i}) dV$$
$$= \int_V \sigma_{ij}\,\frac{1}{2}\left(\delta u_{i,j} + \delta u_{j,i}\right) dV = \int_V \sigma_{ij}\,\delta\varepsilon_{ij} dV \qquad \textbf{(1.4)}$$

Since Equation 1.4 is valid for every arbitrary volume V, the two integrands must be equal to each other. Hence,

$$\delta U_0 = \sigma_{ij}\delta\varepsilon_{ij} \qquad \textbf{(1.5)}$$

From the definition of elastic material, we have

$$U_0 = U_0(\varepsilon_{ij})$$
$$\therefore \delta U_0 = \frac{\partial U_0}{\partial \varepsilon_{ij}}\delta\varepsilon_{ij} \qquad \textbf{(1.6)}$$

[1] The equilibrium equations state that :

$$\sigma_{ij,j} + f_i = 0$$
$$T_i = \sigma_{ij} n_j$$

From Equations 1.5 and 1.6, for an arbitrary variation of $\delta\varepsilon_{ij}$ we can write

$$\sigma_{ij}\delta\varepsilon_{ij} = \frac{\partial U_0}{\partial \varepsilon_{ij}}\delta\varepsilon$$
$$\therefore \sigma_{ij} = \frac{\partial U_0}{\partial \varepsilon_{ij}} \qquad \textbf{(1.7)}$$

From Equation 1.7 the stress-strain relation can be obtained by assuming some expressions of $U_0$ in terms of strain components (*Green's Approach*).
For example if one assumes that the strain energy density function is a quadratic function of the strain components, it can be expressed in the following way:

$$U_0 = D_0 + D_{kl}\varepsilon_{kl} + D_{klmn}\varepsilon_{kl}\varepsilon_{mn} \qquad \textbf{(1.8)}$$

So stress can be written as shown below:

$$\sigma_{ij} = \frac{\partial U_0}{\partial \varepsilon_{ij}} = D_{kl}\delta_{ik}\delta_{il} + D_{klmn}\left(\delta_{ik}\delta_{jl}\varepsilon_{mn} + \varepsilon_{kl}\delta_{im}\delta_{jn}\right) = D_{ij} + D_{ijmn}\varepsilon_{mn} + D_{klij}\varepsilon_{kl}$$
$$= D_{ij} + (D_{ijkl} + D_{klij})\varepsilon_{kl} \qquad \textbf{(1.9)}$$

Substituting $(D_{ijkl} + D_{klij}) = C_{ilkj}$ and $D_{ij} = 0$ (for zero stress, this is valid if also strain is zero), one gets the linear stress-strain relation in the following form :

$$\sigma_{ij} = C_{ijkl}\varepsilon_{kl} \qquad \textbf{(1.10)}$$

This is a general linear relation between two second-order tensors.
In the same way, for a nonlinear material, the stress-strain relation will be :

$$\sigma_{ij} = C_{ij} + C_{ijkl}\varepsilon_{kl} + C_{ijklmn}\varepsilon_{kl}\varepsilon_{mn} \qquad \textbf{(1.11)}$$

The first term on the right-hand side of Equation 1.11 is the residual stress (that is stress for zero strain), the second term is the linear term and the third term is the quadratic term. If we follows the Green's approach, this nonlinear stress-strain relation can be derived from a cubic expression of the strain energy density function :

$$U_0 = D_{kl}\varepsilon_{kl} + D_{klmn}\varepsilon_{kl}\varepsilon_{mn} + D_{klmnpq}\varepsilon_{kl}\varepsilon_{mn}\varepsilon_{pq} \tag{1.12}$$

### 1.1.2 Elastic Constants: Number of Independent Material Constants

The coefficient $C_{ijkl}$ introduced above, depends on the material type. The coefficient values are called material constants or elastic constants. Because $i,j,k,l$ vary from 1 to 3, there are a total of 81 combinations possible but not all 81 material constants are independent.
Since stress and strain tensors are symmetric, we can write

$$C_{ijkl} = C_{jikl} = C_{jilk} \tag{1.13}$$

The relation 1.13 reduces the material constants from 81 to 36 and the stress-strain relation can be written in this form:

$$\begin{Bmatrix} \sigma_{11} \\ \sigma_{22} \\ \sigma_{33} \\ \sigma_{23} \\ \sigma_{31} \\ \sigma_{12} \end{Bmatrix} = \begin{bmatrix} C_{1111}C_{1122}C_{1133}C_{1123}C_{1131}C_{1112} \\ C_{2211}C_{2222}C_{2233}C_{2223}C_{2231}C_{2212} \\ C_{3311}C_{3322}C_{3333}C_{3323}C_{3331}C_{3312} \\ C_{2311}C_{2322}C_{2333}C_{2323}C_{2331}C_{2312} \\ C_{3111}C_{3122}C_{3133}C_{3123}C_{3131}C_{3112} \\ C_{1211}C_{1222}C_{1233}C_{1223}C_{1231}C_{1212} \end{bmatrix} \begin{Bmatrix} \varepsilon_{11} \\ \varepsilon_{22} \\ \varepsilon_{33} \\ 2\varepsilon_{23} \\ 2\varepsilon_{31} \\ 2\varepsilon_{12} \end{Bmatrix} \tag{1.14}$$

In the above expression only six components of stress and strain are shown because the other three components of stress and strain are not independent because of the symmetry of the tensors. The 6x6 C-matrix is known as the

*constitutive matrix*. For elastic materials the strain energy density function can be expressed as a function of only strain. It's double derivative has the form:

$$\frac{\partial^2 U_0}{\partial\varepsilon_{ij}\partial\varepsilon_{kl}} = \frac{\partial}{\partial\varepsilon_{ij}}\left(\frac{\partial U_0}{\partial\varepsilon_{kl}}\right) = \frac{\partial}{\partial\varepsilon_{ij}}\left(\sigma_{kl}\right) = \frac{\partial}{\partial\varepsilon_{ij}}\left(C_{klmn}\varepsilon_{mn}\right) = \left(C_{klmn}\delta_{im}\delta_{jn}\right) = C_{klij} \tag{1.15}$$

Similarly,

$$\frac{\partial^2 U_0}{\partial\varepsilon_{kl}\partial\varepsilon_{ij}} = \frac{\partial}{\partial\varepsilon_{kl}}\left(\frac{\partial U_0}{\partial\varepsilon_{ij}}\right) = \frac{\partial}{\partial\varepsilon_{kl}}\left(\sigma_{ij}\right) = \frac{\partial}{\partial\varepsilon_{kl}}\left(C_{ijmn}\varepsilon_{mn}\right) = \left(C_{ijmn}\delta_{km}\delta_{ln}\right) = C_{ijkl} \tag{1.16}$$

Because the order of derivative should not change the final result (Schwarz's Theorem) one can conclude that $C_{ijkl} = C_{klij}$. This means that the C-matrix must be symmetric. Thus, the number of independent elastic constants is reduced from 36 to 21.

Equation 1.14 takes this form:

$$\begin{Bmatrix}\sigma_1\\ \sigma_2\\ \sigma_3\\ \sigma_4\\ \sigma_5\\ \sigma_6\end{Bmatrix} = \begin{bmatrix} C_{11} & C_{12} & C_{13} & C_{14} & C_{15} & C_{16}\\ & C_{22} & C_{23} & C_{24} & C_{25} & C_{26}\\ & & C_{33} & C_{34} & C_{35} & C_{36}\\ & & & C_{44} & C_{45} & C_{46}\\ & & & & C_{55} & C_{56}\\ & & & & & C_{66}\end{bmatrix} \begin{Bmatrix}\varepsilon_1\\ \varepsilon_2\\ \varepsilon_3\\ 2\varepsilon_4\\ 2\varepsilon_5\\ 2\varepsilon_6\end{Bmatrix} \tag{1.17}$$

For simplicity the six stress and strain components have been indicated with only one subscript, $i$=1,..,6. For the same reason, the material constants are written with two subscripts instead of four.

Equation 1.17 has 21 independent elastic constants in absence of any plane of symmetry. This kind of material is called anisotropic material. However, if the material response is symmetric about a plane or an axis, the number of independent material constants is again reduced.

| N° OF PLANES OF SYMMETRY | N° OF AXIS OF SYMMETRY | N° OF INDEPENDENT ELASTIC CONSTANTS | TYPE OF MATERIAL |
|---|---|---|---|
| 1 | / | 13 | Monoclinic |
| 2/3 | / | 9 | Orthotropic |
| 3 | 1 | 6 | Hexagonal |
| 3 | 2/3 | 2 | Isotropic |

**Table 1.1** Material classification based on the number of planes and axes of symmetry.

### 1.1.3 Stress-Strain Relation for Isotropic Materials

Consider an isotropic medium subjected to two states of strain as shown in figure 1.2.

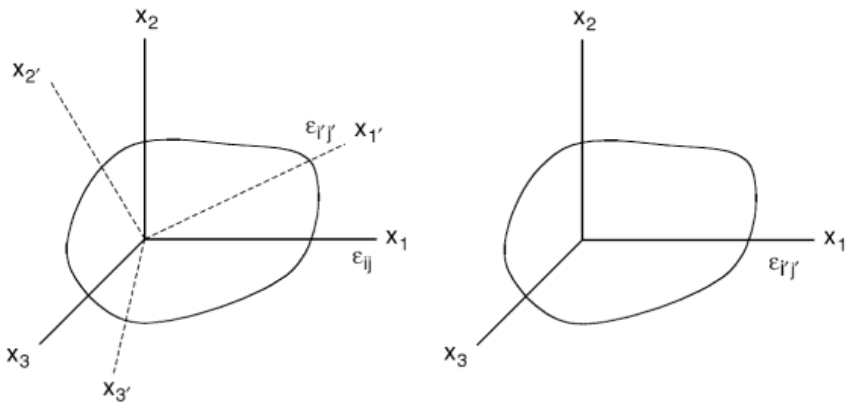


**Fig.1.2** Isotropic material subjected to two states of strain.

The state of strain for the first case is $\varepsilon_{ij}$ while in the second case is $\varepsilon_{i'j'}$. The two strain values are numerically different and $\varepsilon_{i'j'}$ can be obtained by transforming the strain components $\varepsilon_{ij}$, from the $x_1x_2x_3$ coordinate system, to the $x_{1'}x_{2'}x_{3'}$ coordinate system, as shown in the left side of figure 1.2. The strain energy density for the two cases is given by $U_0(\varepsilon_{ij})$ and by $U_0(\varepsilon_{i'j'})$, respectively.

If the material is isotropic, these two values must be equal, since identical numerical values of strain components are applied in two different directions. For isotropic materials equal strain values applied in different direction should not make any difference in computing the strain energy density. The two values $U_0(\varepsilon_{ij})$ and $U_0(\varepsilon_{i'j'})$ are identical if $U_0$ is a function of strain invariants, because strain invariants are the only parameters that do not change when the numerical values of the strain components are changed from $\varepsilon_{ij}$ to $\varepsilon_{i'j'}$.

Three strain invariants can be defined as

$$
\begin{aligned}
I_1 &= \varepsilon_{ii} \\
I_2 &= \frac{1}{2}\varepsilon_{ij}\varepsilon_{ji} \\
I_3 &= \frac{1}{3}\varepsilon_{ij}\varepsilon_{jk}\varepsilon_{ki}
\end{aligned}
\qquad \textbf{(1.18)}
$$

Note that $I_1$, $I_2$ and $I_3$ are linear, quadratic and cubic functions of strain components, respectively. To obtain linear stress-strain relation, the strain energy density must be a quadratic function of strain, as shown below:

$$
\begin{aligned}
&U_0 = C_1 I_1^2 + C_2 I_2 \\
&\therefore \sigma_{ij} = \frac{\partial U_0}{\partial \varepsilon_{ij}} = 2C_1 I_1 \frac{\partial I_1}{\partial \varepsilon_{ij}} + C_2 \frac{\partial I_2}{\partial \varepsilon_{ij}} = 2C_1 I_1 \delta_{ik}\delta_{km} + C_2 \frac{1}{2}\left(\delta_{im}\delta_{jn}\varepsilon_{mn} + \varepsilon_{mn}\delta_{in}\delta_{jm}\right) \\
&\therefore \sigma_{ij} = 2C_1 \varepsilon_{kk}\delta_{ij} + C_2 \varepsilon_{ij}
\end{aligned}
\qquad \textbf{(1.19)}
$$

If we substitute in Equation 1.19 $2C_1=\lambda$ and $C_2=2\mu$, then the stress-relation takes this form:

$$\sigma_{ij} = \lambda \delta_{ij} \varepsilon_{kk} + 2\mu \varepsilon_{ij} \tag{1.20}$$

In relation 1.20 λ and μ are known as Lame's first and second constant, respectively. This equation can be expressed also in matrix form to obtain :

$$\begin{Bmatrix} \sigma_1 = \sigma_{11} \\ \sigma_2 = \sigma_{22} \\ \sigma_3 = \sigma_{33} \\ \sigma_4 = \sigma_{44} \\ \sigma_5 = \sigma_{55} \\ \sigma_6 = \sigma_{66} \end{Bmatrix} = \begin{bmatrix} \lambda+2\mu & \lambda & \lambda & 0 & 0 & 0 \\ 0 & \lambda+2\mu & \lambda & 0 & 0 & 0 \\ 0 & 0 & \lambda+2\mu & 0 & 0 & 0 \\ 0 & 0 & 0 & \mu & 0 & 0 \\ 0 & 0 & 0 & 0 & \mu & 0 \\ 0 & 0 & 0 & 0 & 0 & \mu \end{bmatrix} \begin{Bmatrix} \varepsilon_1 = \varepsilon_{11} \\ \varepsilon_2 = \varepsilon_{22} \\ \varepsilon_3 = \varepsilon_{33} \\ \varepsilon_4 = 2\varepsilon_{23} = \gamma_{23} \\ \varepsilon_5 = 2\varepsilon_{31} = \gamma_{31} \\ \varepsilon_6 = 2\varepsilon_{12} = \gamma_{12} \end{Bmatrix} \tag{1.21}$$

Note that this relation is valid also between shear stresses and engineering shear strains :

$$\sigma_{ij} = \mu \gamma_{ij}$$

Therefore μ is G, the shear modulus.
Equation 1.20 and 1.21 are known as *generalized Hooke's law* in three dimensions. Equation 1.20 can be inverted to obtain strain components in terms of the stress components, as given below:

$$\varepsilon_{ij} = \frac{\sigma_{ij}}{2\mu} + \delta_{ij} \frac{\lambda \sigma_{kk}}{2\mu(3\lambda + 2\mu)} \tag{1.22}$$

### 1.1.4 Hooke's Law in Terms of Young's Modulus and Poisson's Ratio

Strains are usually expressed in terms of stress components with Young's modulus (E), Poisson's ratio (ν) and shear modulus (μ) :

$$
\begin{aligned}
\varepsilon_{11} &= \frac{\sigma_{11}}{E} - \frac{\nu\sigma_{22}}{E} - \frac{\nu\sigma_{33}}{E} \\
\varepsilon_{22} &= \frac{\sigma_{22}}{E} - \frac{\nu\sigma_{11}}{E} - \frac{\nu\sigma_{33}}{E} \\
\varepsilon_{33} &= \frac{\sigma_{33}}{E} - \frac{\nu\sigma_{22}}{E} - \frac{\nu\sigma_{11}}{E} \\
2\varepsilon_{12} &= \gamma_{12} = \frac{\sigma_{12}}{\mu} = \frac{2(1+\nu)}{E}\sigma_{12} \\
2\varepsilon_{23} &= \gamma_{23} = \frac{\sigma_{23}}{\mu} = \frac{2(1+\nu)}{E}\sigma_{23} \\
2\varepsilon_{31} &= \gamma_{31} = \frac{\sigma_{31}}{\mu} = \frac{2(1+\nu)}{E}\sigma_{31}
\end{aligned}
\qquad \textbf{(1.23)}
$$

Since the material is isotropic and has only two independent elastic constants, any of the five common used elastic constants (λ, μ, ν, E and K, with K that is the bulk modulus) can be expressed in terms of any other two elastic constants. In the above equation the relation between E, ν and μ has been incorporated :

$$\mu = \frac{E}{2(1+\nu)}$$

### 1.1.5 Navier's Equation of Equilibrium

Substituting the stress-strain relation expressed in Equation 1.20 into the equilibrium equation [(1)] , one gets

$$
\begin{aligned}
&\sigma_{ij,j} + f_i = 0 \\
&(\lambda\delta_{ij}\varepsilon_{kk} + 2\mu\varepsilon_{ij})_{,j} + f_i = 0 \Rightarrow (\lambda\delta_{ij}u_{k,k} + 2\mu\frac{1}{2}\left[u_{i,jj} + u_{j,ij}\right])_{,j} + f_i = 0 \\
&\lambda\delta_{ij}u_{k,kj} + \mu\left[u_{i,jj} + u_{j,ji}\right] + f_i = 0 \Rightarrow \lambda u_{k,ki} + \mu\left[u_{i,jj} + u_{j,ji}\right] + f_i = 0 \\
&(\lambda+\mu)u_{j,ji} + \mu u_{i,jj} + f_i = 0
\end{aligned}
\qquad \textbf{(1.24)}
$$

In the vector form the above equation can be written as

$$(\lambda+\mu)\underline{\nabla}(\underline{\nabla}\cdot u)+\mu\nabla^2 u+f=0 \qquad \textbf{(1.25)}$$

Because of the vector identity shown below,

$$\nabla^2 u=\underline{\nabla}(\underline{\nabla}\cdot u)-\nabla\times\nabla\times u$$

Equation 1.25 can be written also in this following way:

$$(\lambda+\mu)\underline{\nabla}(\underline{\nabla}\cdot u)-\mu\underline{\nabla}\times\underline{\nabla}\times u+f=0^{(2)} \qquad \textbf{(1.26)}$$

In index notation the above two equations can be rewritten in this way:

$$(\lambda+\mu)u_{j,ji}+\mu u_{i,jj}+f_i=0 \qquad \textbf{(1.27)}$$

The equilibrium equations expressed in terms of the displacement components are known as Navier's equation.

(2) In Equation 1.26 the symbol (.) is used to indicate the scalar product while the symbol (x) is used for the vector product.

## 1.2 Dynamic Problems

In this section we introduce the time dependence and we'll consider an example of a dynamic problem, to obtain the equation of elastic waves.

In all the equations written above it is assumed that the body is in static equilibrium; this means that the resultant force acting on the body is equal to zero. Here we consider a body which is subjected to a nonzero resultant force; it will have an acceleration and the equilibrium equation will be replaced by the following governing equation of motion:

$$\sigma_{ij,j} + f_i = \rho \ddot{u}_i \qquad \textbf{(1.28)}$$

The Navier's equation for the dynamic case takes the following form:

$$(\lambda + 2\mu)\underline{\nabla}(\underline{\nabla} \cdot u) - \mu \underline{\nabla} \times \underline{\nabla} \times u + f = \rho \ddot{u} \qquad \textbf{(1.29)}$$

### 1.2.1 Elastic Waves

Consider a time-dependent normal load *p(t)* on the surface of an elastic half-space as that shown in figure 1.3. The body force is zero, *f=0*.
The loading is applied normal to the $x_1$ direction so the problem geometry is independent of $x_2$ and $x_3$ coordinates.

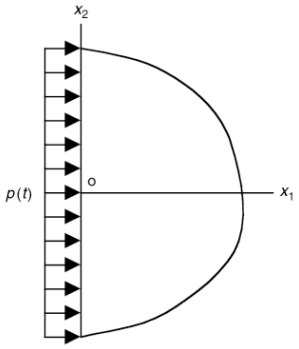


**Fig.1.3** A time-dependent load *p(t)* applied on the surface $x_1 = 0$ of an elastic half space ($x_1>0$).

The solution must be a function of $x_1$ only and must be symmetric about the $x_1$ axis.

This means that,

$$u_2 = u_3 = 0$$
$$u_1 = u_1(x_1)$$

If we substitute these conditions in Equation 1.47 we obtain:

$$(\lambda + 2\mu)u_{1,11} = \rho\ddot{u}_1 \Rightarrow u_{1,11} = \frac{\rho}{\lambda + 2\mu}\ddot{u}_1 = \frac{1}{c_p^2}\ddot{u}_1 \qquad \textbf{(1.30)}$$

where $c_p = \sqrt{\dfrac{\lambda + 2\mu}{\rho}}$ .

Equation 1.30 is a one-dimensional wave equation that has a solution of the form:

$$u_1 = F\left(t - \frac{x_1}{c_p}\right) + G\left(t + \frac{x_1}{c_p}\right) \qquad \textbf{(1.31)}$$

Substituting Equation 1.31 in Equation 1.30 we obtain:

$$u_{1,11} = \frac{1}{c_p^2}\ddot{u}_1 = \frac{1}{c_p^2}\left\{F''\left(t - \frac{x_1}{c_p}\right) + G''\left(t + \frac{x_1}{c_p}\right)\right\} \tag{1.32}$$

where *F''* and *G''* are double derivatives of the functions respect to their arguments.

From the initial condition of the problem we can say that, for $t=0$ and $x_1>0$,

$$\begin{aligned} u_1\big|_{t=0} &= F\left(-\frac{x_1}{c_p}\right) + G\left(\frac{x_1}{c_p}\right) = 0 \\ \dot{u}_1\big|_{t=0} &= F'\left(-\frac{x_1}{c_p}\right) + G'\left(\frac{x_1}{c_p}\right) = 0 \end{aligned} \tag{1.33}$$

Taking the derivative of Equation 1.33 with respect to $x_1$ gives

$$-F'\left(-\frac{x_1}{c_p}\right) + G'\left(\frac{x_1}{c_p}\right) = 0 \tag{1.34}$$

From Equation 1.33 and 1.34 one gets

$$F'\left(-\frac{x_1}{c_p}\right) = G'\left(\frac{x_1}{c_p}\right) = 0 \Rightarrow F'\left(-\frac{x_1}{c_p}\right) = A, G'\left(\frac{x_1}{c_p}\right) = B \tag{1.34a}$$

where A and B are two constants.

We can note that if $t<x_1/c_p$ , the argument of F is negative and the argument of G is positive. If $t>x_1/c_p$ both arguments are positive. Because we have said that F and G equal to the values A and –A (this derives from initial condition in Equation 1.33), the function G should be a constant while the function F is not

necessarily a constant. It is possible to define a new function *f* to express the displacement field, having consider G as a constant:

$$f(t,x_1)=F\left(t-\frac{x_1}{c_p}\right)+G\left(t+\frac{x_1}{c_p}\right)=F\left(t-\frac{x_1}{c_p}\right)-A=f\left(t-\frac{x_1}{c_p}\right) \qquad \textbf{(1.34b)}$$

The displacement field is now expressed in the following way:

$$u_1=0$$
$$u_1=f\left(t-\frac{x_1}{c_p}\right) \qquad \textbf{(1.35)}$$

where the first equation is valid for $t \le x_1/c_p$ while the second one is valid for $t \ge x_1/c_p$.
To obtain the function *f* we use the boundary condition at $x_1=0$, $\sigma_{11}=-p(t)$. Thus,

$$\sigma_{11}=(\lambda+2\mu)\varepsilon_{11}+\lambda(\varepsilon_{22}+\varepsilon_{33})=(\lambda+2\mu)u_{1,11}=$$
$$-\frac{(\lambda+2\mu)}{c_p}f'(t)=-p(t)$$
$$\Rightarrow f'(t)=\frac{c_p}{(\lambda+2\mu)}p(t)=\frac{1}{\rho c_p}p(t)$$
$$\Rightarrow f(t)=\frac{1}{\rho c_p}\int_0^t p(s)ds \qquad \textbf{(1.36)}$$

Combining Equation 1.35 and 1.36 we obtain

$$u_1=f\left(t-\frac{x_1}{c_p}\right)=\frac{1}{\rho c_p}\int_0^{t-\frac{x_1}{c_p}} p(s)ds$$
$$u_1=0 \qquad \textbf{(1.37)}$$

The stress field can be computed in the following manner:

$$\sigma_{11} = (\lambda + 2\mu) u_{1,11} = -\frac{(\lambda + 2\mu)}{c_p} f'\left(t - \frac{x_1}{c_p}\right) =$$

$$-\rho c_p f'\left(t - \frac{x_1}{c_p}\right) = -p\left(t - \frac{x_1}{c_p}\right)$$

$$\sigma_{11} = 0 \qquad \textbf{(1.38)}$$

Equation 1.37 and 1.38 show that the applied stress field *–p(t)* at $x_1=0$ takes a time $t = x_1/c_p$ to propagate at a distance of $x_1$. The propagation velocity is $c_p$. This wave only generates normal or longitudinal stresses in the material, which is why this wave is known as longitudinal or compressional wave. This kind of wave is also known as primary wave or P-wave.

It is possible to demonstrate that if the applied stress is parallel to the free surface, then the disturbance will propagate with a velocity $c_s$ ,

$$c_s = \sqrt{\frac{\mu}{\rho}}$$

In this case, only shear stress will be generated in the material and the wave associated is called shear wave or secondary wave or S-wave.

If the applied load as that shown in figure 1.3 does not extend to infinity in positive and negative $x_2$ directions, then the problem is no longer one-dimensional. The displacement field will have two components, $u_1$ and $u_2$, and both are function of $x_1$ and $x_2$. The problem becomes a two-dimensional one.

It is very difficult to solve two- and three- dimensional problems form Navier's equation. Here we introduce the Stokes-Helmholtz decomposition of the displacement field that transforms the Navier's governing equation of motion into simple wave equations.

### 1.2.2 Stokes-Helmholtz Decomposition

If ϕ is a scalar function and **A** is a vector function, any displacement field **u** can be expressed in the following manner:

$$\mathrm{u} = \underline{\nabla}\phi + \underline{\nabla}\times\mathrm{A} \tag{1.39}$$

This decomposition is known as Stokes-Helmholtz decomposition. Since the above equation has three parameters on the left side ($u_1$, $u_2$, $u_3$) and four on the right side ($\phi$, $A_1$, $A_2$, $A_3$), it is necessary to define an additional relation (gauge condition) such as

$$\underline{\nabla}\cdot\mathrm{A} = 0 \tag{1.40}$$

This condition must be imposed to obtain unique relations between $u_1$, $u_2$, $u_3$ and $\phi$, $A_1$, $A_2$, $A_3$ .
Substituting Equation 1.39 in the Navier's equation, with $\boldsymbol{f}=0$, one gets

$$\begin{aligned}
&(\lambda+2\mu)\underline{\nabla}(\underline{\nabla}\cdot\mathrm{u}) - \mu\underline{\nabla}\times\underline{\nabla}\times\mathrm{u} = \rho\ddot{\mathrm{u}}\\
&\Rightarrow (\lambda+2\mu)\underline{\nabla}\left(\underline{\nabla}\cdot\left\{\underline{\nabla}\phi+\underline{\nabla}\times\mathrm{A}\right\}\right) - \mu\underline{\nabla}\times\underline{\nabla}\times\left\{\underline{\nabla}\phi+\underline{\nabla}\times\mathrm{A}\right\} = \rho\left\{\underline{\nabla}\ddot{\phi}+\underline{\nabla}\times\ddot{\mathrm{A}}\right\}\\
&\Rightarrow (\lambda+2\mu)\underline{\nabla}\left(\underline{\nabla}^2\phi+\underline{\nabla}\cdot\left\{\underline{\nabla}\times\mathrm{A}\right\}\right) - \mu\underline{\nabla}\times\underline{\nabla}\times\left\{\underline{\nabla}\phi+\underline{\nabla}\times\mathrm{A}\right\} = \rho\left\{\underline{\nabla}\ddot{\phi}+\underline{\nabla}\times\ddot{\mathrm{A}}\right\}
\end{aligned} \tag{1.41}$$

Thanks to these vector identities one can write

$$\begin{aligned}
&\underline{\nabla}(\underline{\nabla}\cdot\mathrm{A}) = 0\\
&\underline{\nabla}\times(\underline{\nabla}\phi) = 0\\
&\nabla\times\underline{\nabla}\times\mathrm{A} = \underline{\nabla}(\underline{\nabla}\cdot\mathrm{A}) - \underline{\nabla}^2\mathrm{A}
\end{aligned} \tag{1.42}$$

Substituting Equation 1.42 and 1.40 into Equation 1.41 one obtains

$$(\lambda+2\mu)\underline{\nabla}\left(\nabla^2\phi\right)-\mu\underline{\nabla}\times\left(-\nabla^2\mathrm{A}\right)=\rho\left\{\underline{\nabla}\ddot{\phi}+\underline{\nabla}\times\ddot{\mathrm{A}}\right\}$$
$$\Rightarrow\underline{\nabla}\left[(\lambda+2\mu)\nabla^2\phi-\rho\ddot{\phi}\right]+\underline{\nabla}\times\left[\mu\nabla^2\mathrm{A}-\rho\ddot{\mathrm{A}}\right] \qquad \textbf{(1.43)}$$

Sufficient conditions for the above equation to be satisfied are,

$$\begin{cases}(\lambda+2\mu)\nabla^2\phi-\rho\ddot{\phi}=0\\ \mu\nabla^2\mathrm{A}-\rho\ddot{\mathrm{A}}=0\end{cases}$$

Those equations can be expressed also in the following way:

$$\begin{cases}\nabla^2\phi-\dfrac{\rho}{(\lambda+2\mu)}\ddot{\phi}=\nabla^2\phi-\dfrac{1}{c_p^2}\ddot{\phi}=0\\ \nabla^2\mathrm{A}-\dfrac{\rho}{\mu}\ddot{\mathrm{A}}=\nabla^2\mathrm{A}-\dfrac{1}{c_s^2}\ddot{\mathrm{A}}=0\end{cases} \qquad \textbf{(1.44)}$$

The equations in 1.44 are wave equations that have solutions of the following form:

$$\phi(\mathbf{x},t)=\phi(\mathbf{n}\cdot\mathbf{x}-c_pt)$$
$$\mathbf{A}(\mathbf{x},t)=\mathbf{A}(\mathbf{n}\cdot\mathbf{x}-c_st) \qquad \textbf{(1.45)}$$

These are two waves propagating in the **n** direction with the velocity of $c_p$ and $c_s$ respectively.
When **A**=0 and $\phi\neq0$, from the above solutions one gets

$$\mathbf{u}=\nabla\phi=\mathbf{n}\phi'(\mathbf{n}\cdot\mathbf{x}-c_pt) \qquad \textbf{(1.46)}$$

In this case the direction of the displacement vector **u** and the wave propagation direction **n** are the same.
When **A**$\neq$0 and $\phi$=0, from the above solutions one gets

$$\mathbf{u} = \underline{\nabla} \times \mathbf{A} = \underline{\nabla} \times \mathbf{A}(\mathbf{n} \cdot \mathbf{x} - c_s t) \tag{1.47}$$

Displacement fields given in Equation 1.46 and 1.47 correspond to P- and S-waves, respectively.

So we have assessed that elastic waves in an infinite elastic solid can propagate in two different modes: P-wave mode and S-wave mode. When an elastic wave propagates as a P-wave, only normal stresses are generated in the solid. When an elastic wave propagates as a S-wave, only shear stresses are generated in the solid. The propagation velocities of these two kinds of waves are respectively,

$$c_p = \sqrt{\frac{\lambda + 2\mu}{\rho}}$$

$$c_s = \sqrt{\frac{\mu}{\rho}}$$

In any plane normal to the wave propagation direction **n,** the displacement and the stress components are identical. Every point on a plane normal to **n** has the same state of motion; these planes are called wavefronts and P- and S- waves with plane wavefronts are called plane waves.

If the time dependence of the wave motion is $\sin\omega t$, $\cos\omega t$ or $e^{\pm i\omega t}$ the wave is called harmonic wave. Any function of time can be expressed as a superposition of harmonic functions by the Fourier series expansion.

If we consider an in-plane problem where the waves are propagation in the $x_1x_2$ plane, the wave potentials for P- and S- waves can be expressed in the following manner :

$$\phi(\mathbf{x}, t) = \phi(n_1 x_1 + n_2 x_2 - c_p t) = \phi(x_1 \cos\vartheta + x_2 sen\vartheta - c_p t)$$
$$\psi(\mathbf{x}, t) = \psi(n_1 x_1 + n_2 x_2 - c_s t) = \phi(x_1 \cos\vartheta + x_2 sen\vartheta - c_s t) \tag{1.48}$$

For the harmonic time dependence ($e^{-i\omega t}$) the wave potentials must have this form:

$$\phi(x_1, x_{2,} t) = A\exp(ik_p x_1 \cos\vartheta + ik_p x_2 sen\vartheta - i\omega t) = \phi(x_1, x_2)e^{-i\omega t}$$
$$\psi(x_1, x_{2,} t) = B\exp(ik_s x_1 \cos\vartheta + ik_s x_2 sen\vartheta - i\omega t) = \psi(x_1, x_2)e^{-i\omega t}$$

**(1.49)**

Comparing Equation 1.49 and 1.48 we can see that

$$k_p = \frac{\omega}{c_p}$$
$$k_s = \frac{\omega}{c_s}$$

**(1.50)**

where $k_p$ and $k_s$ are P- and S- wave numbers and ω is the circular frequency (rad/s). The relation between ω and the wave frequency $f$ (Hz) is

$$\omega = 2\pi f$$

**(1.51)**

For time harmonic waves the governing equations are:

$$\begin{cases} \nabla^2\phi + \frac{\omega^2}{c_p^2}\phi = \nabla^2\phi + k_p^2\phi = 0 \\ \nabla^2\psi + \frac{\omega^2}{c_s^2}\psi = \nabla^2\psi + k_s^2\psi = 0 \end{cases}$$

**(1.52)**

## 1.3 Interactions of Light with Matter

In this chapter we are going to describe what happens when light encounters the boundary between two different materials. In general, when light travels along a material medium some portion of the light may be scattered from its original direction. This scattering is caused by the interaction of light with small particles of the medium, atoms or molecules. The scattered light goes off in many different directions and may be scattered again and again until it is finally absorbed somewhere. For monochromatic light the possibility of scattering depends on the size of the particle and on the wavelength of light. So, some wavelength are more susceptible to scattering than others.

### 1.3.1 Reflection and Refraction

When light comes to the boundary between different materials, several things can happen: in general it can be reflected, transmitted and absorbed. Reflection happens when part of the light is reflected back into the material where it came from, while a part of light can continue to travel through the second material. Light which goes through is said to be transmitted. Transmitted light may or may not be absorbed significantly along the way because light penetrates in some material better than in others. This depends on the optical proprieties of the material considered. In general, if light penetrates without much scattering the material is said to be transparent. Materials which let no light through are said to be opaque. The rate at which light that travels along a medium is absorbed can depend especially on the spectral composition of the light and on the mixture of different frequency components. When light comes from a transparent medium to the boundary of an opaque material, there may be some reflection but no significant transmission; all the absorption takes place in a thin layer of material near the surface.
An important effect on transmitted light is that its direction of travel can change as it crosses the boundary between materials. This effect is called refraction and the light is said to be refracted.

When light, propagating in an dielectric medium, with refractive index $n_1$, in the simplest case homogeneous and isotropic, meets the boundary of a second medium with different refractive index $n_2$, the above introduced phenomena of reflection and refraction happen.

The incident beam separates into two beams: a beam that continue to travel in the second medium (refracted beam) and one that is reflected back in the first medium (reflected beam). Incident beam (*i*), reflected beam (*r*) and refracted beam (*t*) are linked by the laws of reflection and refraction.

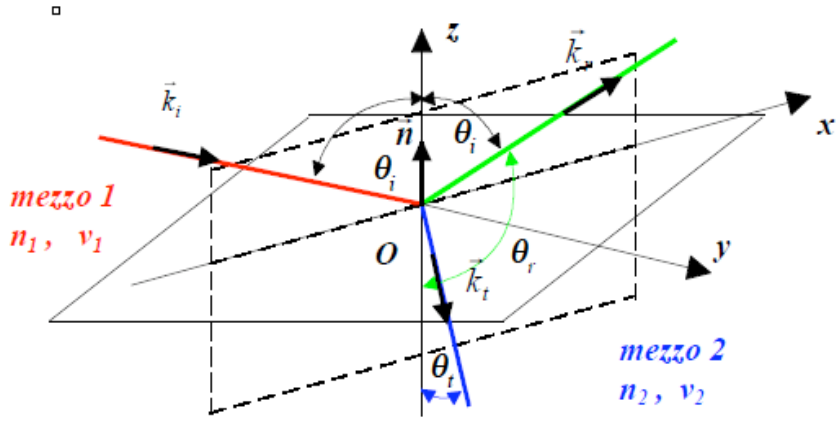


**Fig. 1.4** Incident, reflected and refracted beam through a surface.

In figure 1.4 $\boldsymbol{k}_i$, $\boldsymbol{k}_r$, and $\boldsymbol{k}_t$ are the wavevectors of the incident, reflected and refracted waves, respectively. The incidence plane is the plane formed by the normal **n** (that is coincident with the z axis ) to the surface and the incident light wavevector $\boldsymbol{k}_i$. It can be demonstrated that also $\boldsymbol{k}_r$, and $\boldsymbol{k}_t$ lie in this plane. The angles formed by the three beams with the direction normal to the surface **n** $\theta_i$, $\theta_r$, $\theta_t$. The relations between these are called laws of reflection and refraction :

$$\theta_r = \pi - \theta_i$$

$$\frac{\sin\theta_i}{\sin\theta_t} = \frac{n_1}{n_2} = n_{1,2} \qquad \textbf{(1.53)}$$

These relations are derived with the condition that the propagation direction of the reflected and refracted waves are in the incidence plane. The relation valid for refraction is known as *Snell's law*.

If $n_2 > n_1$, so that the second medium is optically "denser" that the first one, $\sin\theta_t < \sin\theta_i$ and for every incidence angle $\theta_i$ there is a real angle of refraction $\theta_t$. If $n_2 < n_1$ , there will be a real angle of refraction $\theta_t$ only for incidence angles smaller than $\theta^*_i$. For incidence angles larger than $\theta^*_i$, there is total reflection and no radiation is transmitted in the second medium. This will be explained later in more detail.

It must be observed that, even if the radiation does not propagate in the medium, the electromagnetic field cannot disappear, because this would go in contrast with the continuity condition imposed at the separation surface. Therefore there is a wave that propagates along the separation surface with an amplitude that decays exponentially and that is called surface wave or "evanescent" wave.

In the case of a beam that propagates mostly in one direction, there can be diffuse reflection. The reflecting surface can scatter the light so that it travels in many different directions. Figure 1.5 shows what happens to a parallel beam of light when it is reflected diffusely.

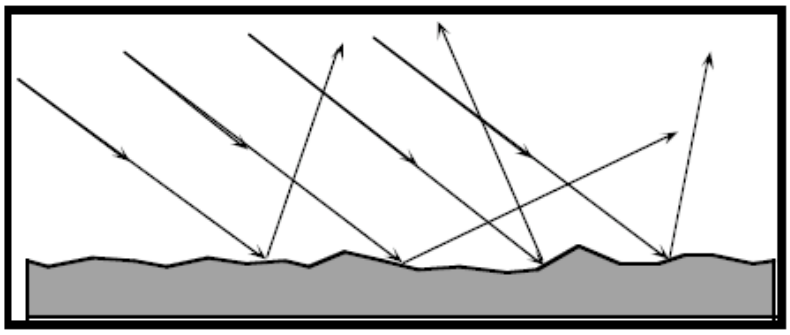

**Fig.1.5** Sketch of diffuse reflection.

Although most examples of reflection in nature are diffuse reflection, the kind of reflection exhibited by mirrors and very smooth surfaces, like those of thin

films, plays a very important role in optics. This kind of reflection is called specular reflection. It can be described as a reflection without scattering. In figure 1.6 there's a sketch of mirror-like reflection where both the incident and reflected light can be represented by bundles of parallel rays. As the incident light that travels in a precise direction, also the reflected light travels in a well-defined direction, and, since there is no scattering, for each incident ray there is only one reflected ray.

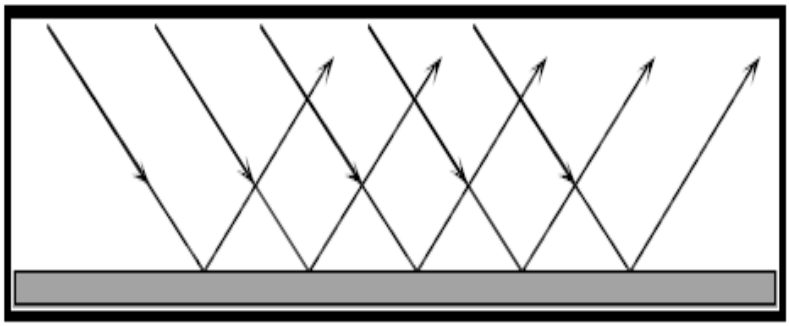

**Fig.1.6** Sketch of specular or mirror-like reflection.

Figure 1.7 describes the behaviour of the rays in specular reflection. If we consider the point where the incident beam meets the surface, also the reflected ray departs from the same point. In this point is constructed a line perpendicular to the mirror surface that is the normal to the surface. The angle between the incident rays and the normal is called angle of incidence while the angle between the reflected ray and the normal is called angle of reflection. Specular reflection is characterized by two laws: the angle of incidence and of reflection are equals and the incident ray, the normal and the reflected ray all lie in the same plane.

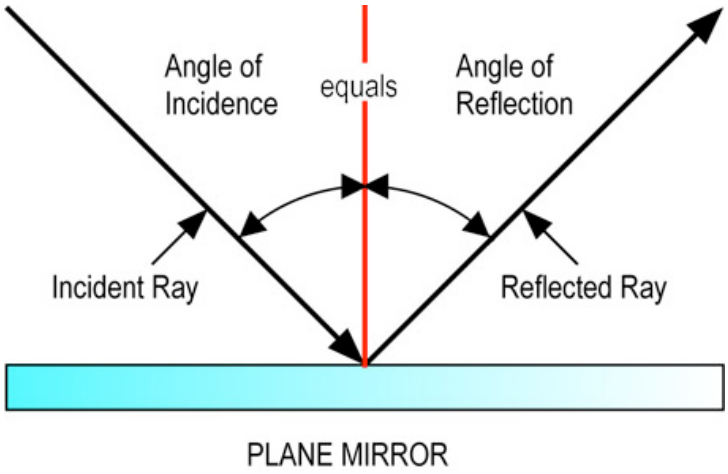


**Fig.1.7** Laws of specular or mirror-like reflection.

It must be noted that the amount of reflected light cannot be predicted by these laws because it depends on the reflectivity of the surface, which is defined as the ratio between the total intensity of reflected light and the total intensity of incident light.

In the case of refraction, part of the light goes into the second material. The direction of the refracted light depends on the characteristics of the two materials. In fact, if the boundary is smooth enough to be a specular reflector, then the direction of the transmitted light is uniquely determined by the nature of the two material, the frequency of the light and the angle of incidence. Furthermore, the light does not go straight ahead; the rays bend at the boundary so that the light goes on in a new direction. Figure 1.8 shows a sketch of refraction.

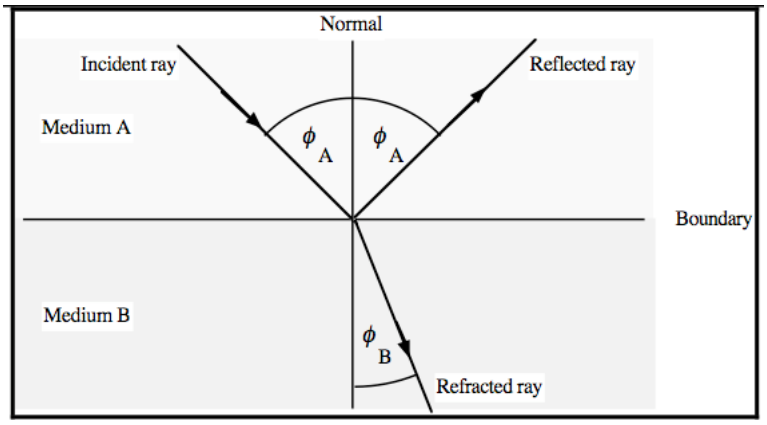


**Fig 1.8** Sketch of refraction.

The new direction is described by two laws: the incident ray, the normal and the refracted ray all lie in the same plane and the direction of the refracted ray is determined by the direction of the incident ray and by the ratio of the speeds of light in the two materials. This last law is known as Snell's law and its original form has been already expressed in Equation 1.53.

This law can be rewritten with the ratio between the speed of light in the materials considered, named A and B. In fact there's a link between the velocity of light and the refractive index. The refractive index $n$ can be defined as the ratio between the speed of light in vacuum $c$ and the speed of light in the material $v$,

$$n = \frac{c}{v} \tag{1.54}$$

The definition of $n$ links the two forms of the refraction law.

So, the original form of the law of refraction becomes:

$$\frac{\sin\phi_A}{\sin\phi_B} = \frac{v_A}{v_B} \tag{1.55}$$

It is easy to see that the law of refraction has a symmetrical form in which swapping the labels A and B makes no difference. This indicates that the incident and refracted light paths are reversible, so that light can travel either way along the path defined by the incident and the refracted rays. This can be seen in figure 1.9 :

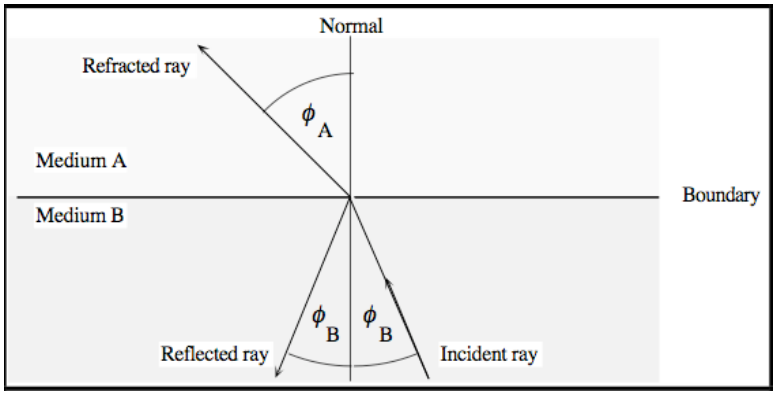


**Fig 1.9** Refraction form a medium with high refractive index.

Note that if the light slow down when it goes into the second medium, the rays will bend towards the normal while, if the light goes faster, the rays will bend away form the normal. In general, light travels faster in vacuum than in any medium so that all refractive indexes are grater than one. The speed of light in a material depends on the chemical composition of the material, the physical state and the on the frequency of light.

A consequence of Snell's law is a phenomenon called total internal reflection.

Total internal reflection is an optical phenomenon that happens when a ray of light strikes a medium boundary at an angle larger than a particular critical angle with respect to the normal to the surface. If the refractive index is lower on the other side of the boundary and the incident angle is greater than the critical angle, no light can pass through and all of the light is reflected. The critical angle $\theta_c$ is the angle of incidence above which the total internal reflection occurs. As it has been introduced above, when light crosses a boundary between

materials with different values of refractive indices, the light beam will be partially refracted at the boundary surface, and partially reflected. However, if the angle of incidence is greater than the critical angle, the light will stop crossing the boundary altogether and instead will be totally reflected back internally. This can only occur where light travels from a medium with a higher refractive index $n_1$ to one with a lower refractive index refractive index $n_2$. For example, it will occur when passing from glass to air, but not when passing from air to glass. The critical angle is given by Snell's law, rearranged to find the critical value for $\theta_i$ when $\theta_t$ is equal to 90°:

$$n_1 \sin\theta_i = n_2 \sin\theta_t \Rightarrow \sin\theta_i = \frac{n_2}{n_1}\sin\theta_t \qquad \textbf{(1.56)}$$

When $\theta_t$ is equal to 90° , sin $\theta_t$ is equal to one and the expression for the critical angle $\theta_c$ is obtained:

$$\theta_c = \arcsin\left(\frac{n_2}{n_1}\right) \qquad \textbf{(1.57)}$$

Figure 1.10 shows the phenomenon of total internal reflection.

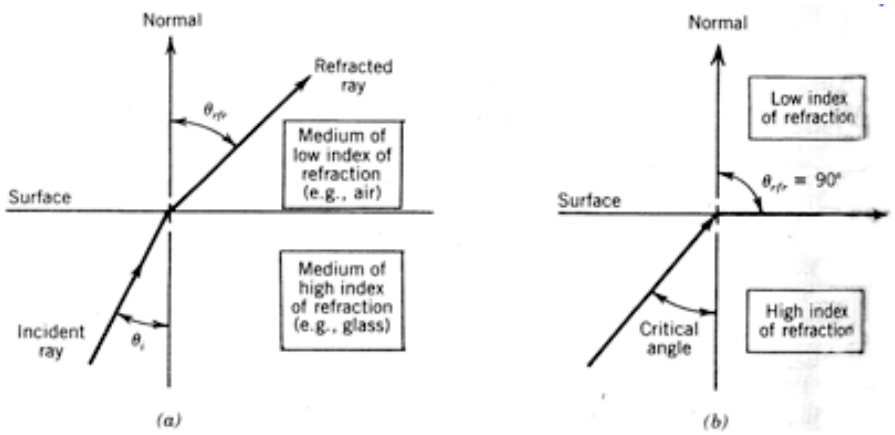


**Fig 1. 10** (a) Sketch of reflection ; (b) sketch of total internal reflection.

# Chapter 2

This chapter offers a brief introduction on the world of acoustic waves, taking in consideration the equation of acoustic waves and its solutions, but also the various kinds of acoustic waves which can propagate in a medium, depending on its properties and on the wavelength to thickness ratio.
In the first part, we present the equation of acoustic waves, first of all in the case of elastic isotropic solids and then in the more general case of anisotropic solids. In the second part, we focus on this equation, analysing its solutions in the case of plane waves and introducing the Christoffel equations, whose secular equation represents the bulk wave dispersion relation for the anisotropic medium, which determines the dependence of the phase velocity on the wavevector. It is important to frame the basics of acoustic waves because inelastic light scattering spectroscopies, or Brillouin and Raman spectroscopies, rely on thermal excited vibrations, that can be view as the incoherent superposition of all the vibrational modes.

## 2.1 Acoustic Waves

Here we are going to derive and describe vibrational elastic excitations which are typically called acoustic, even in the ultrasonic frequency range. We present the equation of acoustic modes in elastic media and, in particular, in the isotropic case, because in the analysis of the results obtained from the Brillouin measurements we will consider our films as if they were isotropic. This allows a strong simplification in many calculations concerning elastic properties because the number of independent elastic constants is reduced to two. However, elastic wave propagation is briefly introduced here also in the case of anisotropic media.
Subsequently, we list the various kinds of acoustic waves, such as bulk waves, surface waves and pseudo-surface waves .

### 2.1.1 Acoustic Modes in Elastic Solids

In the continuum description of a solid, the instantaneous configuration of the solid that goes under deformation can be represented by the displacement vector field $\mathbf{u}(\mathbf{r},t)$, where $\mathbf{u} = (u_1,u_2,u_3)$ and $\mathbf{r} = (x_1,x_2,x_3)$ and $t$ is time. The local state of the solid, as we assessed above, is represented by the strain and stress tensors. In particular, the linear elastic behaviour is characterized by the tensor of the elastic constants $C_{ijkl}$, which can be easily represented as the matrix of the elastic constants $C_{ij}$. The tensor of the elastic constants fully characterizes the stiffness of a solid, when other phenomena of higher orders can be neglected. In a homogeneous linear elastic solid, in the absence of body forces, the equations of motion for the displacement vector field are homogeneous and are the following:

$$\rho \frac{\partial^2 u_i}{\partial t^2} = \sum_{j,k,l} C_{ijkl} \frac{\partial^2 u_k}{\partial x_j \partial x_l} \qquad \textbf{(2.1)}$$

These equations describe vibrational elastic excitations, which are typically called acoustic. The basic solutions of Equations 2.1 and, the most important ones when the boundary effects are irrelevant, are plane waves or modes, of the form:

$$u = e\Re\left\{\tilde{A}\exp\left[i\left(k\cdot r - \omega t\right)\right]\right\} \qquad \textbf{(2.2)}$$

where $\boldsymbol{k}$ is the wavevector, ω is the circular frequency, $f$ the frequency, Ã a complex amplitude and **e** is the polarization vector, which is normalized. The continuum description is appropriate until the wavelength $\lambda = 2\pi/|\boldsymbol{k}|$ is much larger than the interatomic distances. The three translational degrees of freedom of each infinitesimal volume element correspond, for each $\boldsymbol{k}$, to three independent modes having different polarization vectors and frequencies. The acoustic waves are characterized by a phase velocity that depends both on **e** and

on the direction of $\boldsymbol{k}$. The phase velocity, which is a function of frequency, is given by:

$$v = \frac{\omega}{|k|} = \lambda f \tag{2.3}$$

In the simplest case, of isotropic solid, the matrix of the elastic constants is fully determined by two independent quantities; the only non null elements of the matrix are:

$$C_{11} = C_{22} = C_{33}$$
$$C_{44} = C_{55} = C_{66}$$
$$C_{12} = C_{13} = C_{11} - 2C_{44}$$

In this case the shear modulus G coincides with $C_{44}$ while Young modulus E, Poisson's ratio ν and bulk modulus B are respectively given by:

$$\begin{aligned} E &= \frac{C_{44}\left(3C_{12} + 2C_{44}\right)}{C_{12} + C_{44}} = \frac{C_{44}\left(3C_{11} - 4C_{44}\right)}{C_{11} - C_{44}} \\ \nu &= \frac{C_{12}}{C_{12} + C_{11}} = \frac{C_{11} - 2C_{44}}{2\left(C_{11} - C_{44}\right)} = \frac{E}{2G} - 1 \\ B &= \frac{C_{11} + 2C_{12}}{3} = C_{11} - \frac{4}{3}C_{44} \end{aligned} \tag{2.4}$$

In the isotropic case the phase velocities are independent from the direction of $\boldsymbol{k}$, only depending on the relative orientation of **e** respect $\boldsymbol{k}$. One of the three modes is longitudinal with **e** parallel to $\boldsymbol{k}$ and has velocity $v_l$. The other two are transversal with **e** normal to $\boldsymbol{k}$, independent (the two polarization vectors are orthogonal) and degenerate: they have the same velocity $v_t$.
The two velocities introduced above are:

$$v_l = \sqrt{\frac{C_{11}}{\rho}}$$
$$v_t = \sqrt{\frac{C_{44}}{\rho}} \qquad \textbf{(2.5)}$$

In a non isotropic case more than two independent constants are needed to determine the matrix of the elastic constants, and the phase velocities, beside depending on the direction of $\boldsymbol{k}$, have a more complex dependence on the $C_{ij}$ values.

In a finite geometry the search of standing waves having the harmonic time dependence, transforms Equation 2.1 in an eigenfunction/eigenvalue equation of the Helmholtz type[2] . The eigenvalues are proportional to $\omega^2$, the square of the frequencies of the acoustic modes of the structure, also defined as natural frequencies of the structure. These frequencies depend on the $C_{ij}/\varrho$ values and on geometry. In the simplest case of a one dimensional structure of length L, the standing waves are identified by the constructive self interference condition,

$$L = \frac{n\lambda}{2} = \frac{n}{2}\frac{v}{f} \qquad \textbf{(2.6)}$$

where *n* is an integer number.

Substituting above the relation between C and v we obtain:

$$f = \frac{\left(\frac{n}{2}\right)\sqrt{\frac{C}{\rho}}}{L} \qquad \textbf{(2.7)}$$

Here C represents the general combination of elastic constants valid in the isotropic case but also in the anisotropic case.

Therefore, a measurement of the frequencies of the acoustic modes allows to derive

$$C = \frac{\rho(fL)^2}{\left(\frac{n}{2}\right)^2} \tag{2.8}$$

Also in more complex geometries the dependence is always of the same form:

$$C = \rho(fL)^2 N \tag{2.9}$$

where here L is the characteristic length of the structured considered and N is a dimensionless numerical factor which, beside the mode order n, can depend on dimensionless quantities like geometrical aspect ratios or Poisson's ratio. This factor depends also on the character of the mode whose frequency *f* is being measured and therefore on the specific modulus C which is involved.

### 2.1.2 Acoustic Waves in Anisotropic Media

The theoretical approach here is referred to the general case of anisotropic media but it includes as a special case isotropic solids.
It was shown that in an homogeneous isotropic solids two types of bulk acoustic modes exist: primary (P) waves, longitudinally polarized, and secondary (S) waves, transversely polarized. Two independent (orthogonal) transverse polarization directions exist. Their velocities, respectively $v_l$ and $v_t$, given by Equations 2.5, are independent from wavelength, since such a medium does not identify any length scale. In isotropic solids, the secondary waves are perfectly equivalent while in anisotropic media they are not. These modes are called fast transverse (FT) and slow transverse (ST) and have different phase velocities and polarization vectors, which depend on the propagation direction. It must be remembered that in anisotropic solids the polarization vectors are generally neither exactly parallel nor exactly perpendicular to the wavevector so the modes are called quasi longitudinal and quasi transverse.

At surfaces other acoustic modes can be encounter. At a stress free surface of a semi-infinite isotropic elastic solid surface, waves such as the Rayleigh waves (RW) exist. These are non-dispersive acoustic waves[3] that have peculiar characteristics: they have its energy and displacement fields confined near the surface, with the amplitude which declines with depth, with the decay length being close to the wavelength, a wavevector parallel to the surface and a velocity lower than that of any bulk wave. The surface wave cannot couple to bulk waves and does not lose its energy irradiating towards the bulk. Pseudo surface waves can also exist, which violate this last condition. The velocity of a Rayleigh wave cannot be given in a closed form but, in the isotropic case, exist a good approximation:

$$v_R \cong v_t \frac{2{,}87C_{11} - 4C_{44}}{3C_{11} - 4C_{44}} \cong v_t \frac{0{,}862 + 1{,}14\nu}{1+\nu} \qquad \textbf{(2.10)}$$

Similar waves existing on anisotropic surfaces are called generalized Rayleigh waves (GRW). The solution of this kind of wave differs from the true Rayleigh wave on isotropic media only in the form of the variation of the displacement with depth.

There can be other kind of waves such as Lamb waves and Love waves. Lamb waves are in-plane and anti-plane modes in freestanding plates while Love waves are transverse modes in a layered half space[1]. In certain cases exist also unattenuated waves travelling along interfaces between two solids (Stoneley waves). Along a free-stress boundary, surface skimming longitudinal and transverse waves can exist. These are generally called longitudinal guided waves (LGW). Furthermore, waves that are surface-like waves can exist. They slowly radiate energy away from the surface and their displacement field does not vanish at infinite depth. They are not surface waves in the strict sense but their energy is confined near the surface so they are generally called pseudo-surface waves (PSAWs).

[3] A non-dispersive wave is a wave whose phase velocity is not dependent on the wavenumber.

These waves have a phase velocity higher than that of the lowest of the bulk waves in the substrate.
The presence of a layer over a substrate leads to the appearance of various kind of waves confined within the layer. In fact, more complex modes occur in inhomogeneous media.
For a single layer on a solid substrate, these waves are called generalized Lamb or Seazawa waves. The behaviour of generalized Lamb waves depends on the thickness of the layer in relation to the wavelength and the relative densities of the layer and the substrate. For wavelengths much smaller than the thickness wave propagation occurs within each layer as if it is infinite, with reflection and refractions at the surfaces. Instead, for wavelengths comparable to the thickness or even larger, the acoustic modes extend over several layers and are modes of the whole structure. Such modes are in general dispersive, with velocities depending on the wavelength.

## 2.2 Elastodynamics of Anisotropic Media

This section is devoted to the analysis of the wave equation of acoustic waves, derived in the first part of this chapter, with a special attention to the equations of elastodynamics and to the determination of some elastic constants by Brillouin velocity data.
As we have introduced in the previous paragraph, the wave equation for an infinite anisotropic elastic solid is

$$\rho \frac{\partial^2 u_i}{\partial t^2} = C_{ijkl} \frac{\partial^2 u_k}{\partial^2 x_j \partial x_l} \tag{2.11}$$

where $C_{ijkl}$ is the fourth rank elastic modulus tensor and $\varrho$ is the density. This equation admits plane wave solution with the form,

$$u_i = U_i \exp\left[ i\left(k \cdot x - \omega t\right)\right] \tag{2.12}$$

where $\boldsymbol{k}$ is the wavevector, ω the angular frequency and **U** is the polarization vector.

Polarization vectors are related by the set of three linear equations, known as Christoffel equations,

$$\left(C_{ijkl}k_j k_l - \rho\omega^2\delta_{ik}\right)U_k = 0 \tag{2.13}$$

where $\delta_{ik}$ is the Kronecker delta symbol. The corresponding secular equation is :

$$D(k,\omega) = \left|C_{ijkl}k_j k_l - \rho\omega^2\delta_{ik}\right| = 0 \tag{2.14}$$

The last equation represents the bulk wave dispersion relation for the anisotropic medium. By dividing Equation 2.14 by $k^6$, it becomes :

$$D(n,c) = \left|C_{ijkl}n_j n_l - \rho c^2\delta_{ik}\right| = 0 \tag{2.15}$$

which determines the dependence of the phase velocity $c(\boldsymbol{n}) = \omega/\boldsymbol{k}$ on the wave normal $\boldsymbol{n} = \boldsymbol{k}/k$. This is a cubic equation in $c^2$ whose solutions become simpler for special directions of the wave normal or wavevector, such as along rotational symmetry axis or in a mirror symmetry plane. The solutions of this equations are polynomials involving ω, $k_x$, $k_y$ and $k_z$ in three dimensions. For a vector wave equation, there will be a different dispersion relation for every distinct mode of propagation.

When the wave normal lies in a crystallographic mirror plane, one of the three modes is pure transverse, polarized normal to the plane, while the other two are mixed modes, with polarization vectors parallel to the plane. In this case, the Christoffel secular determinant diagonalises, yielding a linear equation for the pure T mode and a quadratic function for the quasi-longitudinal, qL, and quasi-transverse, qT, modes. When $\boldsymbol{n}$ is normal to a mirror plane, the one mode is pure longitudinal, with polarization along $\boldsymbol{n}$, and the other two are pure transverse.

Velocity and its inverse, named slowness (s = $\boldsymbol{k}/\omega$), in high symmetry direction are expressed using the contracted notation of Voight for the elastic constants, $C_{\alpha\beta}$.

For example, in the (001) symmetry plane of a cubic crystal there are three independent constants $C_{11}$, $C_{12}$ and $C_{44}$, the phase velocity and the slowness of the pure T mode are independent of direction and are given by

$$\rho c^2 = \rho / s^2 = C_{44} \qquad \textbf{(2.16)}$$

For the coupled qT and qL modes the equation takes a quadratic form with phase velocities that depend on the angle θ between the wave normal and the <100> direction. There can be simplification for special directions where these modes also become pure modes; for example for θ=0, π/2 these relations are valid :

$$\rho c_L^2 = \rho / s_L^2 = C_{11}$$
$$\rho c_T^2 = \rho / s_T^2 = C_{44} \qquad \textbf{(2.17)}$$

The formulas of the equations above are widely used in the recovery of elastic constants form Brillouin velocity data in high symmetry directions.

In the simplest case of isotropic solids the velocities are independent of direction and are expressed below :

$$\rho c_L^2 = C_{11} = \lambda + 2\mu$$
$$\rho c_T^2 = C_{44} = \mu \qquad \textbf{(2.18)}$$

where λ and μ are the Lame's elastic constants.

# Chapter 3

This is the chapter dedicated to the introduction of the Brilluoin scattering mechanism. It is very important to know the principles and the features of the inelastic scattering phenomenon to understand the Brilluoin spectroscopy which is the technique we used in this work to achieve some information about the vibrational behavior of thin films, which will be related to the morphological structure.

In a crystal, the inelastic scattering of acoustic phonons, the so-called acoustic branches of the dispersion relation, are the vibration of the degrees of freedom of the center of mass of the unit cells. With visible light and with typical properties of solids these branches produce inelastic scattering with frequency shifts which range from few GHz to tens of GHz. In the first part of this chapter we focus on the basics of Brilluoin spectroscopy, introducing the principle of Brillouin scattering and the scattering geometries that select a specific wavevector $\boldsymbol{k}$ or $\boldsymbol{k}_{\parallel}$ which is probed by the inelastic light scattering events. We will present all the scattering geometries but we will concentrate on the backscattering one which is the most exploited geometry in this work. In this section we describe also the scattering mechanism, distinguish between the scattering in the bulk by acoustic waves and the scattering by surface waves. In the former case we talk about the elasto-optic effect, due to the periodic modulation of the refractive index by the periodic strain of the acoustic wave, while in the latter case we refer to the ripple mechanism, related to the periodic corrugation of the surface due to the surface wave.

In the second part of the chapter, we are going to work on the the experimental method, describing the experimental set up of Brillouin measurements. Then we focus on the spectral analysis performed by the Fabry-Perot interferometer, describing its operation and main characteristic and defining important parameters such as the contrast, the finesse and the free spectral range FSR. The third and last part of the chapter is dedicated to the calibration of the obtained Brillouin spectra, describing the principal peaks that can be viewed, and to the

analysis of the uncertainties associated to the measured frequencies or velocities.

## 3.1 The Brillouin Spectroscopy Technique on Solids

In this section is described the overall Brillouin scattering, starting form the theoretical principle and then illustrating the various scattering geometries, which are all presented here even if the most exploited one in this work is the backscattering geometry. There are also few considerations on the scattering phenomenon, introducing the ripple scattering and the elasto-optic scattering.

### 3.1.1 The Principle of Brillouin Scattering

Brillouin light scattering (BLS) is defined as inelastic scattering of light in a physical medium by thermally excited acoustical phonons. Brillouin scattering (BS) depends to statistical phenomena, when scattering of light occurs in a physical medium due to interaction of the light with dynamic inhomogeneity in the medium. These inhomogeneities are caused by thermal fluctuations of the density in the medium. Thermal fluctuations can be seen as a superposition of acoustic waves (thermal phonons) propagating in all directions [(3)].
In Brillouin Scattering, a laser beam of angular frequency $\Omega_i$ and wavevector $\mathbf{q}_i$ is incident on a surface of a sample at angle $\theta$ to the normal. Most of this light is specularly reflected, refracted at angle $\theta$' or absorbed.

[(3)] These are the results of the studies conducted by Einstein, Debye and Smoluchovskii (Landau at al. 1984).

However, because of thermally excited dynamic fluctuations in the strain field within the solid and dynamic rippling of the surface, a small amount of light is also diffusely scattered. In this scattering process the light undergoes a fractional change in frequency of the order of $c_{acoust}/c_{light} \sim 10^{-5}$ , where $c_{acoust}$ is the acoustic wave speed and $c_{light}$ is the speed of light. The radiation scattered in a particular direction is collected and analyzed.

The radiation spectrum contains an intense sharp central peak, unshifted in frequency, due to the elastic scattering. A weaker and broader peak can also be present at the unshifted frequency $\Omega_i$: it is due to scattering by dynamic but non-traveling excitations and is called quasi-elastic scattering. There are two mirror image sidebands due to the inelastic scattering of the incident light by thermal phonons. The frequency downshifted one is called Stokes band and the the frequency upshifted one the anti-Stokes band. This part of the spectrum depends on the optical and elastic properties of the sample, the scattering geometry and the vibration modes of the solid that the light is able to couple to.

The inelastic scattering process can be understood considering thermal noise as a superposition of vibrational modes of any wavevector. This principle is based on the fact that in the bulk, a harmonic wave of wavevector **k** corresponds to a dynamic and periodic fluctuation of the strain field that, by the elasto-optic effect[1], causes a periodic modulation of the dieletric constant and of the refractive index *n*.

Brillouin components may be regarded as a Doppler shift of the incident light caused by moving sound waves in the process of Bragg's reflection. The strain field of a harmonic wave induces a periodic modulation of the refractive index by the elasto-optic effect. This periodic modulation of *n* is like that made by an optical grating that diffracts the light. In this way, BS can be viewed as Bragg's reflection of the incident light by moving diffraction grating created by the thermal phonon.

The wave field scattered by an acoustic wave is the superposition of many contributions which, according to Bragg's law, interfere constructively with each other only at the angle given by

$$2\lambda_{acoust}\sin\left(\frac{\theta}{2}\right)=\frac{\lambda_0}{n} \tag{3.1}$$

where θ is the scattering angle, $\lambda_{acoust}$ is the period of the diffraction grating, $\lambda_0$ is the laser wavelength in vacuum and $n$ is the refractive index of the medium. Because the grating is in motion with velocity $c_{acoust}$, scattering is accompanied by a Doppler effect, which results in the scattered photons being shifted in frequency by $\Delta f$. This Doppler frequency for a source in motion with velocity much smaller than $c_{light}$ is given by

$$\Delta f=\frac{nV}{\lambda_0} \tag{3.2}$$

where $V$ is the component of the velocity of the source parallel to the propagation direction of light. In the case of our interest of scattering by an acoustic wave

$$V=c_{acoust}\sin\left(\frac{\theta}{2}\right) \tag{3.3}$$

Scattered light undergoes this shift twice, upon absorption and subsequent reemission, so the Doppler shift by an acoustic phonon is

$$\Delta f=\frac{2nc_{acoust}\sin\left(\frac{\theta}{2}\right)}{\lambda_0} \tag{3.4}$$

Combining Equation 3.1 and 3.4 one gets

$$\Delta f=\frac{c_{acoust}}{\lambda_{acoust}}=f_{acoust} \tag{3.5}$$

where $f_{acoust}$ is the frequency of the sound wave that causes the scattering. In BLS experiments Equation 3.4 is used to calculate the phonon velocity, $c_{acoust}$, with this expression:

$$c_{acoust} = \frac{\lambda_0 \Delta f}{2n \sin\left(\frac{\theta}{2}\right)} \qquad \textbf{(3.6)}$$

From a quantum mechanics point of view the scattering process can be interpreted as a phonon creation (Stokes) or annihilation (anti-Stokes), where the photon loses or gains the energy of the phonon, respectively.

The inelastic scattering of a photon and a bulk phonon obeys two laws, the conservation of the vector momentum and of energy. If we define $\boldsymbol{q}_i$, $\boldsymbol{q}_s$, $\boldsymbol{q}'_i$, $\boldsymbol{q}'_s$ as the wavevector of the incident (i) and scattered (s) light in a vacuum and in the medium, so that $\boldsymbol{q}'_s = n\,\boldsymbol{q}_s$ and $\boldsymbol{q}'_i = n\,\boldsymbol{q}_i$, where $n$ is the refractive index of the medium where the scattering occurs. Then the conservation laws take the form:

$$\begin{aligned} \boldsymbol{q}'_s - \boldsymbol{q}'_i &= \pm \boldsymbol{k} \\ \Omega_s - \Omega_i &= \pm \omega(\boldsymbol{k}) \end{aligned} \qquad \textbf{(3.7)}$$

where ω is the circular frequency of the phonon, $\boldsymbol{k}$ stands for the phonon's wavevector and $\Omega_i$ and $\Omega_s$ are incident and scattered circular frequencies. The sign (+) in Equations 3.7 refers to an anti-Stokes event, when a phonon disappears in the process and the photon gains energy, and the sign (–) refers to a Stokes event, where a phonon is created and the photon loses energy.

Assuming that $n$ is equal for incident and scattered photons, the photon wavevectors are related to their frequencies by

$$\begin{aligned} \boldsymbol{q}'_i\, c &= n\Omega_i \\ \boldsymbol{q}'_s\, c &= n\Omega_s \end{aligned} \qquad \textbf{(3.8)}$$

The wavevectors for the Stokes scatter are related by the cosine theorem,

$$k^2 = q'^2_i + q'^2_s - 2q'_i q'_s \cos\theta \tag{3.9}$$

Substituting Equation 3.8 in Equation 3.9 we obtain

$$\frac{k^2 c^2}{n^2} = \Omega_i^2 + (\Omega_i - \omega)^2 - 2\Omega_i(\Omega_i - \omega)\cos\theta =$$
$$\omega^2 + 4\Omega_i^2\left(1 - \frac{\omega}{\Omega_i}\right)\sin\left(\frac{\theta}{2}\right) \tag{3.10}$$

In Equation 3.10, the sign (–) is used for Stokes scattering in the Equation 3.7. The BLS shift in frequency $\Delta f = \omega/2\pi$ is very small (~$10^{10}$ GHz) compared to the frequency of the photon (~$10^{14}$ GHz). This means that $\Omega_i \approx \Omega_s$ and $|q_s| \approx |q_s| = 2\pi/\lambda_0$.

From Equation 3.10 we can obtain Bragg's Equation:

$$|k| = \frac{2\pi}{\lambda_{acoust}} = \frac{4\pi n}{\lambda_0}\sin\left(\frac{\theta}{2}\right) \tag{3.11}$$

### 3.1.2 The Scattering Mechanism

In transparent solids inelastic scattering mostly occurs in the bulk. The scattering in this case is mediated by the elasto-optic scattering mechanism. In this phenomenon the dynamic fluctuations of the strain field $\varepsilon_{ij}$ give origin to fluctuation of the dieletric constant and these translate into fluctuations of the refractive index. The strain field of an harmonic wave of wavevector ***k*** induces a periodic and traveling modulation of the refractive index.

In the case of anisotropic media the dieletric constant is a tensor $\chi_{ij}$ of rank two and its fluctuation are given by

$$\delta\chi_{ij} = p_{ijkl}\varepsilon_{kl} \tag{3.12}$$

where $p_{ijkl}$ is the tensor of the elasto-optic constants and $\varepsilon_{kl}$ is the strain tensor.
The strain field in the bulk, away form the surface, is the superposition of the displacement fields of all the bulk P, FT and ST acoustic waves of the solid, introduced in chapter 2. The spectrum of the scattered radiation contains three principal peaks at frequency shifts $\omega = c_{acoust}k$ , where $c_{acoust}$ is the phase velocity of these waves in the direction of $\boldsymbol{k}$**.** The intensities of these peaks vary considerably; they depends on the scattering integral over the scattering volume and on the direction, the polarization and the amplitude of the acoustic wave and the elasto-optic constants of the solid. It is quite common that one or more peaks are too faint ore even are zero.
There is also another kind of scattering mechanism that occurs at a surface. In this case the scattering is mediated by the surface rippling scattering mechanism, based on the dynamic corrugations in the surface profile due to the wave displacements. For this kind of mechanism the kinematic condition expressed in Equation 3.7 pertains only to the components parallel to the surface. This mechanism is a minor one in transparent solids but is the only active one in opaque solids.
The wavevector constraint given by Equation 3.7 allows to coupling to a continuous spectrum of bulk modes, incident on the surface and with $\boldsymbol{k}$ given by $\boldsymbol{k}_{\parallel}$ and any value of the component normal to the surface. This part of the spectrum is called Lamb shoulder.
The scattering cross section for the ripple mechanism with frequency change ω and surface scattering wavevector $\boldsymbol{k}_{\parallel}$ is proportional to the power spectrum $<|u_3(\boldsymbol{k}_{\parallel,\omega})|^2>$ of the normal fluctuations on the surface profile[3] .

### 3.1.3 The Scattering Geometries

The scattering geometry is defined by the direction of the incident light beam, and the direction along which the light is collected. The sample orientation identifies the probed wavevector $\boldsymbol{k}$.
The incident light is a monochromatic laser light with wavelength (in vacuum) $\lambda_0$, wavevector $\boldsymbol{q}_i$ and circular frequency $\Omega_i$. These quantities are related by these relations:

$$|q_i| = q_i = \frac{2\pi}{\lambda_0}$$
$$\Omega_i = c_{light} q_i \qquad \textbf{(3.13)}$$

where $c_{\text{ight}}$ is the velocity of light. The incident beam hits the surface at an angle θ to the normal; this light is specularly reflected, absorbed, refracted at angle θ' with wavevector $\boldsymbol{q'}_{\text{i}}$, elastically scattered or inelastically scattered undergoing a frequency shift. Light emerging in the direction of wavevctor $\boldsymbol{q}_{\text{s}}$ is collected and analysed.

The scattering process is analysed considering first a multilayered system with all layer's plane parallel. The refractive indexes of these layers are respectively $n'$, $n''$, $n'''$,…; the wavevectors of the scattered and incident photons in the vacuum and in the various layers are $\boldsymbol{q}_{\text{i}}$, $\boldsymbol{q}_{\text{s}}$, $\boldsymbol{q'}_{\text{i}}$, $\boldsymbol{q'}_{\text{s}}$, $\boldsymbol{q''}_{\text{i}}$, $\boldsymbol{q''}_{\text{s}}$,… . The incident and scattered circular frequencies $\Omega_i$ and $\Omega_s$ remain unchanged upon refraction. Indicating $l_{\text{ight}}$ with $c$, we have:

$$\Omega_i = cq_i = \left(\frac{c}{n'}\right) q'_i = \left(\frac{c}{n''}\right) q''_i = \ldots$$
$$\Omega_s = cq_s = \left(\frac{c}{n'}\right) q'_s = \left(\frac{c}{n''}\right) q''_s = \ldots \qquad \textbf{(3.14)}$$

These equalities imply that

$$q_i = \frac{q'_i}{n'} = \frac{q''_i}{n''} = \ldots$$
$$q_s = \frac{q'_s}{n'} = \frac{q''_s}{n''} = \ldots \qquad \textbf{(3.15)}$$

while Snell's law implies that

$$q_i \sin\theta_i = q'_i \sin\theta'_i = q''_i \sin\theta''_i = \ldots \qquad \textbf{(3.16)}$$

The Snell's law expressed in Equation 3.16 is also valid for the scattered photon, substituting *i* with *s*.

Equation 3.15 and 3.16 show that in the m-th layer the modulus of the wavevector $\boldsymbol{q}^{(m)}_{\mathrm{i}}$ and its component parallel to the surface (Equation 3.16) remain the same in all the layers and are independent of the number of interposed layers. Therefore, only the refractive index of the layer in which the scattering occurs will be considered and indicated with *n*. As we have introduced above, the conservation equation between the wavevectors $\boldsymbol{q'}_{\mathrm{i}}$ and $\boldsymbol{q'}_{\mathrm{s}}$ identified the probed wavevector $\boldsymbol{k}$ . The directions of $\boldsymbol{q}_{\mathrm{i}}$ and $\boldsymbol{q}_{\mathrm{s}}$ are selected by the experimental set up and the direction of $\boldsymbol{q'}_{\mathrm{i}}$ and $\boldsymbol{q'}_{\mathrm{s}}$ result from refraction. However, when the wavevector $\boldsymbol{k}$ is parallel to the surface ($\boldsymbol{k} = \boldsymbol{k}_{\parallel}$) , Equation 3.7 holds for the component parallel to the surface. Because they remain unchanged upon refraction, refraction becomes irrelevant and conservation can be expressed as:

$$\left(q_{\boldsymbol{s}} - q_i\right)_{\parallel} = \pm k_{\parallel} \qquad \textbf{(3.15)}$$

This happens namely for scattering by surface waves and for scattering by bulk waves in the platelet configuration, that will be illustrated below.

In the analysis of Equation 3.7, 3.8 and 3.13 the big difference between the velocity of light and any acoustic wave allows some simplifications. Equation 3.7 implies that

$$|k| < |q_i''| + |q_s''|$$

that, by Equation 3.8 and 3.13 means that

$$\omega = |\Omega_{\mathrm{i}} - \Omega_{\mathrm{s}}| \leq \frac{c_{\mathrm{acoust}}}{c_{\mathrm{light}}/n}\left(\Omega_{\mathrm{i}} + \Omega_{\mathrm{s}}\right) \qquad \textbf{(3.16)}$$

Showing that the relative difference $|\Omega_s\text{-}\Omega_i|/\Omega_i$ is at most of the order of $c_{\mathrm{acoust}}/(c_{\mathrm{ight}}/n)$, at most $10^{-4}$-$10^{-5}$. This means that the scattering event can be

analysed with this approximation: $q_s \approx q_i$, $q'_s \approx q'_i$. The directions of $q'_s$ and $q'_i$ uniquely identify with $q_i$ the scattering configuration and the acoustic wavevector $\boldsymbol{k}$. The direction of the incident beam with the normal to the incident plane identifies the incidence plane. The out-of-plane directions are not considered but some in plane possibilities are available.

Figure 3.1 shows the geometries we have considered: direct backscattering by bulk waves in a transparent solid; backscattering by surface waves; indirect backscattering by bulk waves in a transparent supported layer; scattering in transmission by bulk waves (platelet configuration) and forward scattering in transparent or semi-transparent solids.

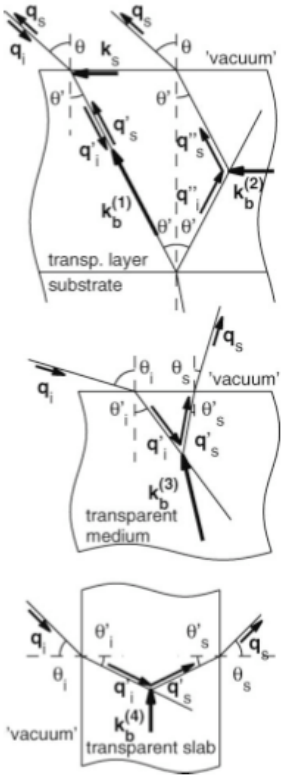


**Fig.3.1** Scattering geometries for Brillouin spectroscopy (Thin arrows: optical wavevectors, thick arrows: acoustical wavevectors). a) Backscattering, direct ($\mathbf{k}_b{}^{(1)}$) and indirect ($\mathbf{k}_b{}^{(2)}$); b) forward scattering ($\mathbf{k}_b{}^{(3)}$) and c) transmission scattering ($\mathbf{k}_b{}^{(4)}$).

Figure 3.1 shows all the possible scattering geometries even if some of them, such as the scattering in transmission, can be exploited only if we have a transparent substrate. In our case, we used almost for all the measurements the backscattering configuration so we are going to analyse in a more precise way only this geometry.

Exact backscattering, with $\boldsymbol{q}_s = -\boldsymbol{q}_i$, is the most frequently used geometry. In non-opaque media it can be the outcome of different scattering geometries. In the case of direct backscattering it is the outcome of scattering bulk waves with $\boldsymbol{q'}_s = -\boldsymbol{q'}_i$, such that the probed wavevector is $\boldsymbol{k}_b^{(d)} = \pm 2\boldsymbol{q'}_i$, whose modulus is the maximum achievable with an incident radiation with $\lambda_0$, and is expressed in this way:

$$k = \left|\boldsymbol{k}_{\mathrm{b}}^{(\mathrm{d})}\right| = 2\left|\boldsymbol{q}'_i\right| = 2\frac{2\pi}{\lambda_0}n \qquad \textbf{(3.17)}$$

In an optically isotropic solid, spectral doublet, whose frequencies are independent of the incident angle, are expected. Each of them identifies a velocity through the value of $n$,

$$c_{acoust} = \frac{\lambda_0 \Delta f}{2n} \qquad \textbf{(3.18)}$$

where $c_{\mathrm{acoust}}$ stands for the phase velocity of the P, FT or ST wave in the direction of $\boldsymbol{k}$. However, in fully isotropic solids the scattering cross section for transverse waves is zero in this geometry and so the only velocity accessible is that of the P-wave. In an anisotropic solid, $c_{\mathrm{acoust}}$ can depend on the direction of $\boldsymbol{k}$, implying a dependence of the doublet frequency on the incidence angle. In both opaque and transparent media interaction can also occur with a surface wave. In this case momentum conservation holds only for the component parallel to the surface, $\boldsymbol{q'}_{s//} = -\boldsymbol{q'}_{i//}$, and the probed wavevector is $\boldsymbol{k}_{//} = \pm 2\boldsymbol{q}_{i//}$, whose modulus is

$$k = \left|\boldsymbol{k}_{\|}\right| = 2\left|\boldsymbol{q}_{i\|}\right| = 2\frac{2\pi}{\lambda_0}\sin\theta \tag{3.19}$$

that depends on the incident angle but not on the refractive index. In the spectrum a continuum, named Lamb shoulder, is expected, due to the coupling with bulk modes, and discrete doublets due to the surface modes, whose frequencies scale as sinθ. Each doublet has a velocity that is given by

$$c_{acoust} = \frac{\lambda_0 \Delta f}{2\sin\theta} \tag{3.20}$$

In the case of transparent layer on a reflecting substrate, there have been several observations from the scattering of the reflected beam of wavevector $\boldsymbol{q'}^{(i)}_{i}$ . This geometry is called indirect backscattering, with probed wavevector $\boldsymbol{k}_b^{(i)}$ or simulated platelet, because the beam reflected at the interface serves as incident light for scattering in a platelet geometry. In the symmetric configuration this wavevector is parallel to the surface:

$$\boldsymbol{k}_b^{(i)} = \boldsymbol{q}_i' - \boldsymbol{q}_s' = \boldsymbol{q}_{i\|}' - \boldsymbol{q}_{s\|}' \tag{3.21}$$

This wavevector is identical to the one by which surface waves are probed and has the same modulus

$$k = \left|\boldsymbol{k}_b^{(i)}\right| = 2\left|\boldsymbol{q}_{i\|}\right| = 2\frac{2\pi}{\lambda_0}\sin\theta \tag{3.22}$$

If the layer is sufficiently thick, the modes it supports at this wavevector are bulk modes. Therefore, this geometry permits to measure bulk waves at a wavevector that is independent of *n*. This is due to the fact that the components of the involved wavevector are only those parallel to the surface that remain unchanged upon refraction. In contrast to direct backscattering, in this case the

scattering cross sections for the transverse waves are not zero and all the bulk (P, FT, ST waves) velocities are accessible.

## 3.2 The Experimental Method

In this part of the third chapter we describe the experimental apparatus which we used to obtain the Brilluoin spectra. We are going to present the complex system of optical devices which is needed to focus the laser beam onto the sample. In the second part, we are going to introduce the basics of the analysis of the obtained spectra, concentrating on the description of the function and of the main characteristics of the Fabry-Perot interferometer. It is through this device that we are able to do the spectral analysis of the scattered light. In particular, we will describe the tandem multipassing Fabry-Perot interferometer, which is made of two FP interferometers operating in series with multiple passages to improve both the contrast and the finesse, two characteristic parameters of the interferometer.

### 3.2.1 Experimental Set-up

Brillouin light scattering experiments require illuminating the sample with a laser beam, collecting the light scattered in a given direction and analysing its spectrum. The spectral analysis of the results of this technique are performed with the tandem Fabry-Perot interferometer in the Sandercock configuration.
In the simplest case experiments are conducted in air at ambient temperature and pressure. The sample is in the open on a sample holder on the optical table where is set the whole apparatus.

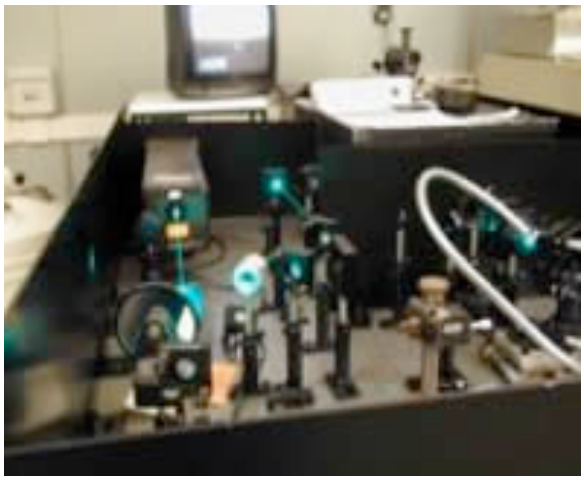

**Fig.3.2** Excitation laser and system of optics for Brillouin spectroscopy, at NEMAS Lab. , Politecnico di Milano.

One of the most peculiar characteristics of BS is that it is a contact-less measure; this makes the technique suited to experiments in which the specimen is kept in controlled conditions. The only required condition is the optical access to the sample, guaranteed by optical windows. At pressures not far from ambient pressure the sample environment can be controlled by a chamber with optical windows of the type used in spectroscopy. The transparency of diamond also allows optical access to samples subjected to extreme pressure and temperature conditions in a diamond anvid cell (DAC).

The laser beam is directed onto the specimen by a small mirror, called the incidence mirror, and focused onto the specimen surface by a lens, called the front lens. Spatial filtering is needed and is performed by a pinhole. The scattered beam is focused onto a pinhole by a lens and can then be reconverted to a parallel beam. On the optical path to the spectrometer two steering mirrors can be inserted to give additional degrees of freedom, which is useful for alignment purposes. Figure 3.3 shows a sketch of the whole apparatus.

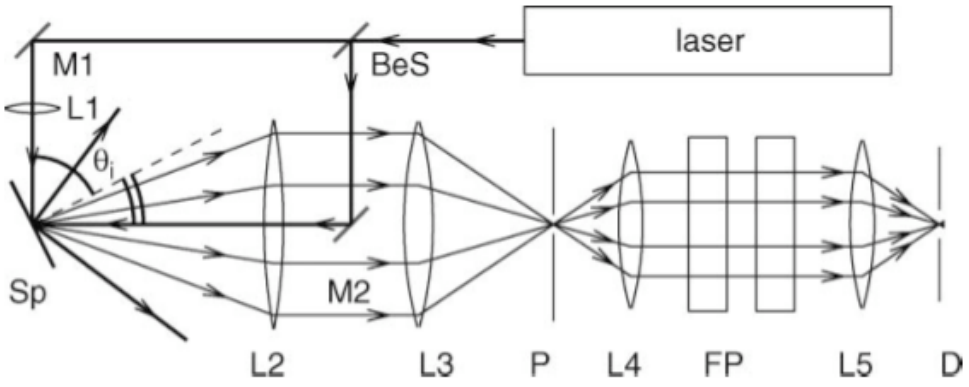


**Fig.3.3** Experimental set-up for Brillouin spectroscopy. BeS: beam splitter; M1, M2: mirrors; Sp: sample; L1-L5: lenses; P: entrance pinhole of the spectrometer; FP: Fabry-Perot interferometer; D: light detector. [4]

Even if the experimental set-up of figure 3.3 is able to realize all the geometries, backscattering geometry is the most widely adopted especially for scattering by surface waves (SBS, surface Brillouin scattering). This geometry has some advantages such as the fact that the front lens focuses the incident beam and also collects the scattered light. In any other geometry two separate lenses are involved and their focal points must coincide to high precision. For this reason other geometries have been adopted in volume scattering but rarely in surface scattering. In volume scattering, due to the finite extension of the waist of the focused incident beam, the requirement of coincident foci is less stringent than in SBS, where the additional requirement of precise coincidence at the surface must be guaranteed. Another advantage of backscattering is that, at least for incidence not too close to the normal, the collection direction is far from the specular reflection one and in the collected beam there is less light elastically scattered.

The incident laser beam is polarized either parallel or orthogonal to the plane of incidence. Light is collected without polarization analysis except in the case of tests for peaks attributions, as we have reported for example in chapter 6. In

fact, the incident polarization is preserved in scattering by BL (bulk longitudinal) and Rayleigh waves and rotated in scattering by BT (bulk transverse) waves.

### 3.2.2 Spectral Analysis: Fabry-Perot Interferometer

The analysis of Brillouin spectra can be a difficult task. The collected light contains an intense elastic peak at the incident frequency $\Omega_i$ and one or more weak doublet at frequencies $\Omega_i \pm \omega$. In figure 3.4 is shown an example of Brillouin spectra.

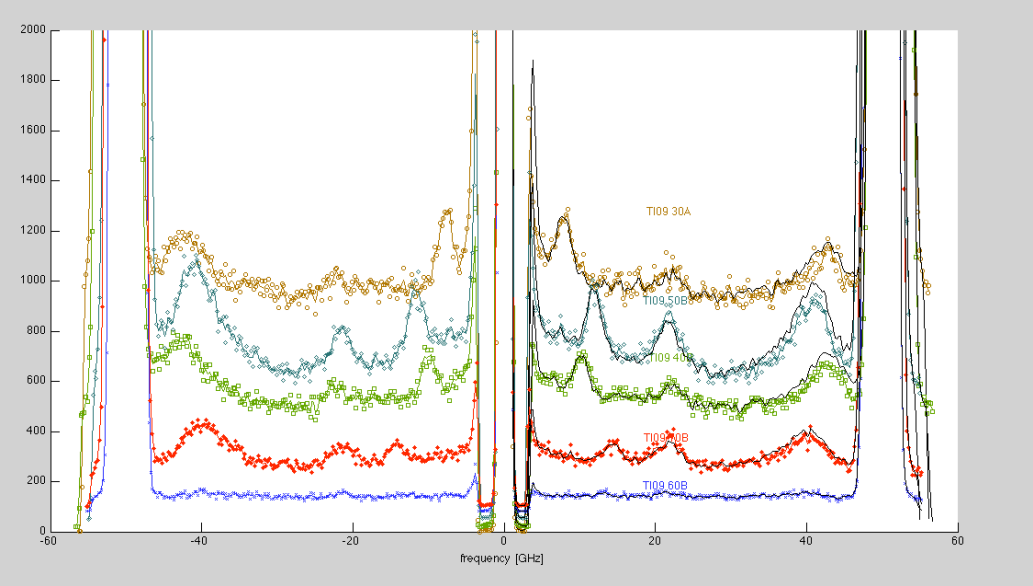


**Fig.3.4** Example of a Brillouin spectra taken on a $TiO_2$ sample with a Si substrate.

In figure 3.4 we can clearly see three couples of Stokes/Anti-Stokes peaks and the spectral ghosts, at the extremes of the free spectral range, whose origin will

be explained in the following paragraph.

In general, the difficulty derives form the low intensity of the doublet and its small relative shift in frequency. The intensity of the doublets is of several orders of magnitude lower than that of the elastic peak and the relative shift for SBS and also for volume scattering is of the order of $10^{-4}$. With green light the incident frequency is $\sim 10^{14}$ Hz and the spectral shift is of the order of 30 GHz or lower. The smallness of this frequency shift is a characteristic that prevents analysis by dispersive methods such as diffraction gratings.

Two methods have been exploited to overcome this difficulty, narrow bandwidth tunable band-pass filters and beating methods. The standard choice is the scanning multipass Fabry-Perot interferometer that is able to achieve the required filtering performances. The Fabry-Perot Interferometer is an optical resonator that transmits only the light of its resonant wavelength and acts like a band-pass filter. Because its resonant frequency can be adjusted, it can be used to scan all the spectrum to be measured. The most common type of this interferometer is the Sandercock one, which is able to resolve the weak Brillouin doublets. Sandercock first showed that the contrast can be significantly improved by multipassing the interferometer, with three or five passes up to seven passes. Usually there are two synchronized coupled Fabry-Perot because this solution avoids the overlapping of different orders of interference. Couples of multipass interferometer have been developed and the latter configuration evolved into the 3+3 passes tandem interferometer that is the type of spectrometer most commonly adopted in Brillouin spectrometry.

Here we describe the plane Fabry-Perot interferometer which is an optical resonator formed by two plane-parallel partially reflecting mirrors, at a distance $d$ from each other. A photography of the interferometer can be viewed in figure 3.5.

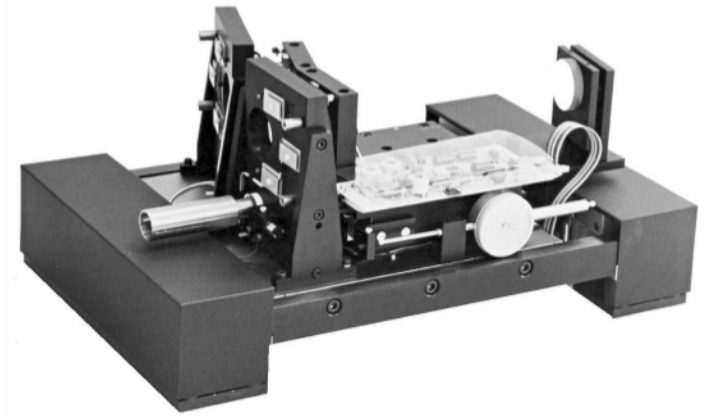

**Fig.3.5** Fabry-Perot interferometer apparatus.

The light that enters into the cavity through on of the incompletely reflecting mirror, is reflected back and forth, part of it being leaked at each reflection. The light path can be seen in figure 3.6.

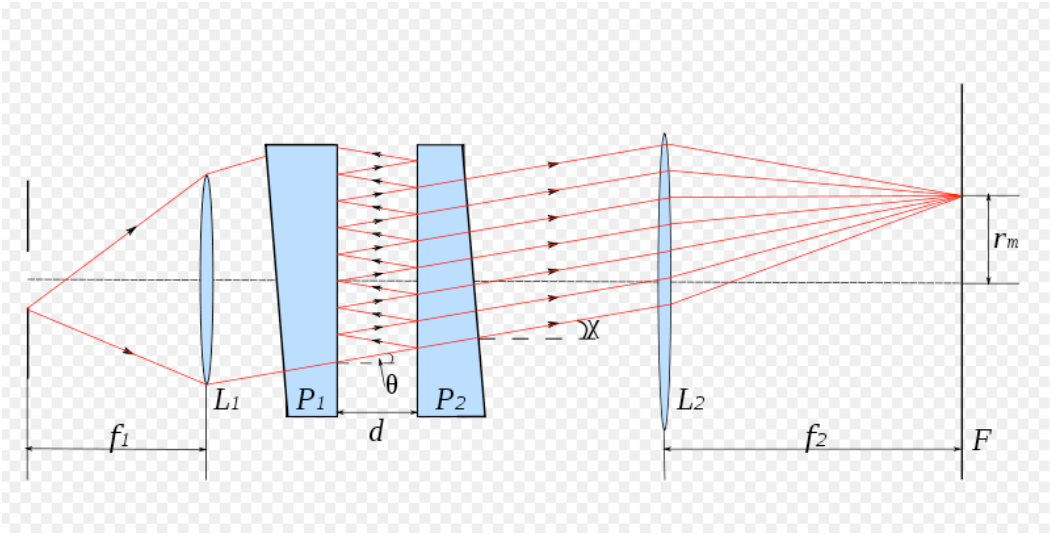


**Fig.3.6** Full scheme of Fabry-Perot etalon and path of light in it.

The light that leaks from the second mirror is the transmitted light. In the multiple reflection process the intensity of the wavelengths that satisfies the constructive interference condition is enhanced while all the other wavelengths

decay. The transmitted light contains only wavelengths whose intensity in the cavity is high. So, for a given spacing *d* between the mirrors, the interferometer will transmit only certain wavelengths λ as determined by:

$$T = \frac{\tau_0}{1 + \left(\frac{4F^2}{\pi^2}\right)\sin^2\left(\frac{2\pi d}{\lambda}\right)} \qquad \textbf{(3.25)}$$

where $\tau_0$ (<1) is the maximum possible transmission determined by losses in the system and F is the finesse, a quality factor depending on the mirror reflectivity and flatness. Equation 3.25 shows that only wavelengths satisfying this relation, for integral values of *p*, will be transmitted. This is illustrated below in figure 3.7.

$$d = \frac{1}{2} p\lambda \qquad \textbf{(3.26)}$$

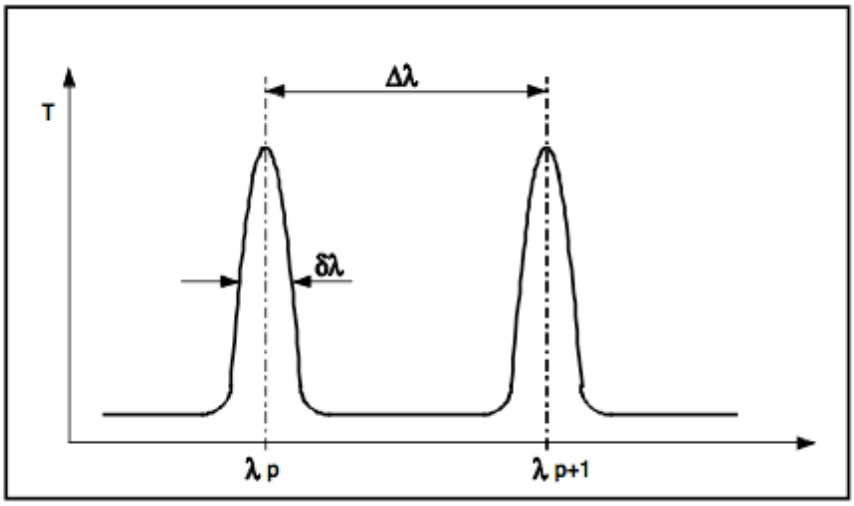


**Fig.3.7** Two successive transmitted peaks of width δλ separated by Δλ.

So, the equally spaced frequencies are $\nu_m = m(c_{light}/2d)$. The frequency spacing is called free spectral range and it is given by, FSR= $c_{light}/2d$.

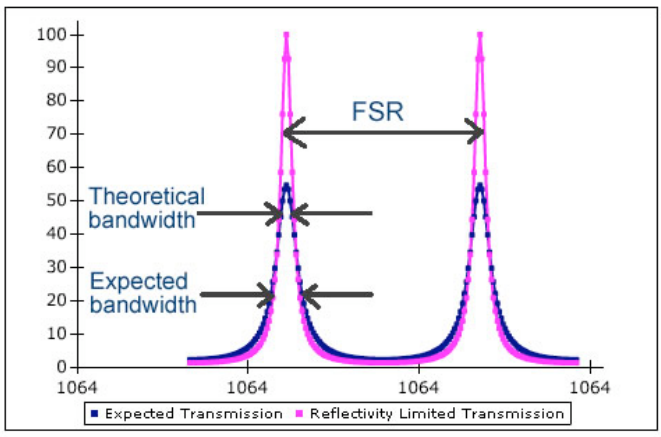


**Fig.3.8** Free spectral range between transmitted peaks in the interferometry.

The common characterization of sharpness, that is an increasing function of the reflectivity R, is usually expressed in term of finesse F defined above. Finesse is also defined as the ratio of the distance $\Delta\varphi = 2\pi$ between two consecutive maxima to the FWHM (full width at half maximum). We can call FWHM as $\delta\varphi$. In this way we can express finesse as the ratio between the distance of two transmitted wavelengths and the width of a give transmission peak:

$$F = \frac{\Delta\varphi}{\delta\lambda}$$

Both parameters, FSR and F, are increasing function of R and have limited values because R too close to unity makes the maximum transmission decline. In general, high performance filtering requires having high values of F and a strong attenuation of those $\lambda$ that are not transmitted. However, in practice F cannot be much grater than about 100 due to limitations on the quality of mirror substrates and coatings. The relation between resolution and FSR is limited by the achievable values of F. By modulating the distance between the mirrors it is possible to modulate FSR and so the transmitted frequencies $f_m$.

The Fabry-Perot interferometer acts as bandpass filter, transmitting all the frequencies $f_m$ which are at equal spacing FSR form each other, with bandwidth of FSR/F around each of them. The interferometer can be operated also as a spectrometer using on of the transmitted frequencies as a narrow bandwidth bandpass filter, whose frequency is scanned across the spectral interval to be measured. Operation of the interferometer as a Brillouin spectrometer is accomplished first by adjusting $d$ to a central value $\boldsymbol{d}$ such that the incident laser frequency is transmitted $\Omega_i/2\pi$, and then varying $d$ around $\boldsymbol{d}$: $d=\boldsymbol{d}+\delta d$. This means that the **m**-th transmission peak coincides with laser frequency $\boldsymbol{f_m}=\mathbf{m}(c_{light}/2\boldsymbol{d})= \Omega_i/2\pi$. The selected FSR is $(c_{light}/2\boldsymbol{d})$. Then $d$ is varied with $|\delta d|\leq \boldsymbol{d}/\mathbf{m}$. The extrema of this interval are identified by the transmission peaks $f_{m-1}$ and $f_{m+1}$. The $\boldsymbol{f_m}$ transmission frequency scans the frequency range $\delta\Omega/2\pi=\pm(\Omega_i/2\pi)/\mathbf{m}=\pm(c_{light}/2\boldsymbol{d})=\pm$FSR around $\Omega_i/2\pi$. The frequency shifts measured range from a few GHz to some tens of GHz. In general a typical choice are FSR of tens of GHz that means distances $\boldsymbol{d}$ of a few millimetres (0-10 mm).

Once light enters the FP interferometer, then it is detected by a photomultiplier that is typically operated in the single counting mode. The distance or frequency scan is usually performed by discrete steps. The distance is kept fixed for a given time, the photons are counted and attributed to that channel, then the distance is changed to a new value and photons are counted and the attributed to the new channel and so on. The overall scanning amplitude is twice the FSR and the number of channel into which the scan is subdivided is correlated to the finesse. Because the filtered bandwidth is FSR/F and the filter transfer function is an Airy function, that is similar to a Gaussian, if the number of channels is smaller than 2F the adjacent channel do not overlap and some of the spectral information is lost. But if the number of channels is too higher than 2F, the adjacent channels strongly overlap and redundant data is collected. So, the optimal number of channels is larger, but not too much, than 2F. We usually consider a 512 channels spectrum.

Because the finesse is a parameter of the specific interferometer and is independent of mirror distance, once the number of channels is fixed the only parameter that the operator must choose is the FSR, that translates in the choice of the mirror distance $d$. Because the spectrum is measured in the ± FSR

interval, the optimal choice for FSR requires an estimate of the frequency of the peaks to be measured. In fact, if the FSR is too wide there is poor resolution but it must obviously be larger than the frequency to be measured. Increasing mirror distance, FSR decreases and peaks at low frequency can be explored in a better way. Instead, if we want to explore higher frequencies, mirror spacing is reduced to increase FSR. In general, FSR should not exceed twice the expected value of frequency that must be measured.

The filtering efficiency is measured by the finesse and the contrast. One of the problem in the analysis of Brillouin spectra us the presence of the intense elastic peak; measurement of the doublets has to contend with the proximity of this very intense peak. The contrast cannot be infinite and the one achievable by a single FP interferometer is not sufficient to filter this peak off. Therefore multipassing interferometer is adopted. Passing the scattered light more times by the same interferometer increases both the contrast and the finesse. Similarly, tandem interferometers are adopted. The most useful arrangement is a system with two interferometers in which the space of the second one $L_2$ is close to $L_1$, where $L_2$ and $L_1$ are the optical distances between the mirrors (the spacing $d$ multiplied by the refractive index $n$ of the gas between mirrors). In general a good practical value for $L_2/L_1$ is 0,95.

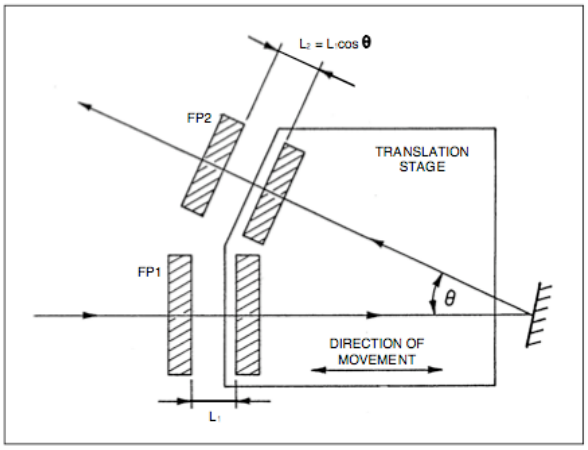


**Fig.3.9** Translation stage of the two FPs, FP1 and FP2 that are able to scan synchronously.

In this way two interferometers with slightly different FSRs can be synchronously scanned, keeping their $f_m$ transmission peaks coincident with a high overall transmissivity; however, due to the different FSRs, if the transmission peaks $f_m$ coincide, then the extrema of the frequency interval $f_{m-1}$ and $f_{m+1}$ of the two interferometers do not coincide, and each of the interferometers cancels the transmission peaks of the other, avoiding replication of spectra.

In general the finesse achievable by a FP tandem interferometer is about 100. The non perfect suppression is showed by the partial transmission of the intense laser light. This occurs at the extreme of the frequency interval FSR when one, not both, interferometer does not transmit the laser frequency and gives rise to the instrumental peaks called "ghosts" at ± FSR. These ghosts, that we present in the spectrum in figure 3.4 can be used for calibration purposes, once the distance among the mirrors is known.

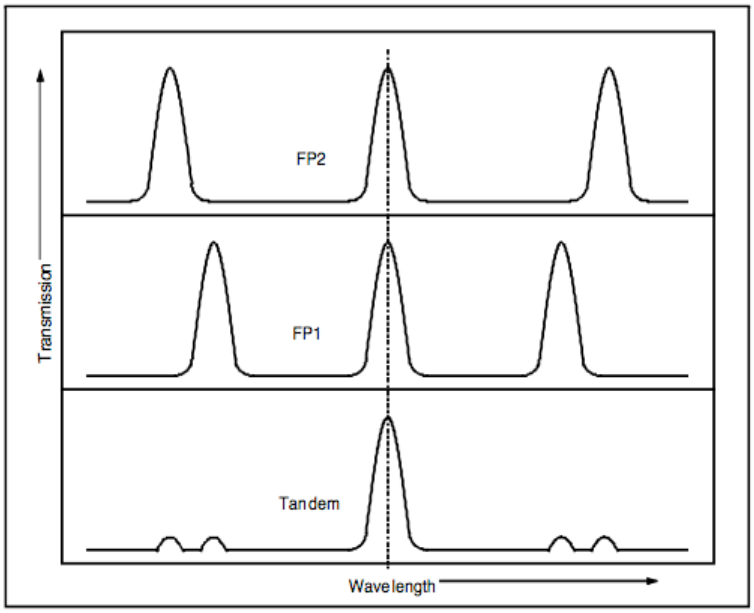


**Fig.3.10** Tandem interferometry with two FPs in series.

## 3.3 Brilluoin Spectra: calibration and uncertainty analysis

In this third part of the chapter we describe the calibration in frequency of the Brilluoin spectra, taking in consideration the different geometries. Then we will focus on the assessment of uncertainties relative to the measured frequencies or velocities, committed in the set of the scattering configuration and in the fitting process. We concentrate on the backscattering case but every geometric configuration has its own set of uncertainties which must be analysed case by case.

### 3.3.1 Frequency Calibration of Brillouin Spectra

The Fabry-Perot interferometer, operated as a tunable bandpass filter, supplies the raw spectrum as photon count number vs. channel number. Frequency calibration is performed identifying with a best fit procedure the positions of the peak of the two ghosts, at channel numbers $n^+_g$ and $n^-_g$, and attributing to them the frequency shifts of ± FSR. The frequency shift of a doublet is expressed in this way:

$$f = FSR\frac{\left(n_p^+ - n_p^-\right)}{\left(n_g^+ - n_g^-\right)} \qquad \textbf{(3.29)}$$

The frequency shift $f = |f_t - f_0|$ of a Stokes/anti-Stokes doublet is obtained, via the identification of the channel numbers of the peaks, $n^+_p$ and $n^-_p$.
The channel number corresponding to the null frequency shift is best identified as $n_0 = ( n^+_g + n^-_g)/2$.
The frequencies of the peaks we have measured are fitted with the MATLAB program. All the peaks have been fitted with gaussians in two different ways: the first is called “single doublet” and makes use of gaussians to fit the peaks; the second one is called “sum of doublets” and makes use of gaussians to fit the peaks, but with lorenztians curves to fit the background.

Scattered light of the nominal wavevector $\mathbf{q}_s$ has sharply defined frequencies, and would give peaks having the instrumental width FSR/F. Due to the finite aperture, light is collected having all the wavevectors within a whole cone whose axis is $\mathbf{q}_s$, resulting form scattering by acoustic wavevectors which span a whole region around the nominal $\mathbf{k} = \pm(\mathbf{q'}_s - \mathbf{q'}_i)$. Interaction with a whole interval of acoustic wavevectors causes a peak broadening. A simple geometric analysis shows that this broadening is asymmetric. These effects are minimized in direct backscattering and their relevance increases monotonically for scattering angles going from $\pi$ to zero. Finally, these effects are more relevant for acoustic wavevectors parallel to the surface ($\mathbf{k}_s$ and $\mathbf{k}^{(2)}_b$, see figure 3.2), because the projection of the wavevectors onto the surface is a non linear operation. For the exchanged wavevectors $\mathbf{k}^{(1)}_b$ and $\mathbf{k}^{(3)}_b$ (scattering angle of $\pi$ or close to it) the collection angle has a minor effect and doublets can still be fitted by simple Gaussians.

For the exchanged wavevector $\mathbf{k}^{(4)}_b$, which is parallel to the surface, the collection angle has a non negligible effect, whose computation is more complex because of the possible non perfect confocality of the incidence lens and the collection lens. A theoretical prediction of the peculiar shape of the double peaked ghosts is even more difficult, because it depends on not controllable factors; in general the sum of two Gaussians is adopted because of its simplicity.

### 3.3.2 Estimate of the Uncertainties

The outcome of BS measurement is given by the acoustic velocities $c_{acoust}$ obtained from each measured frequency shift $f$ via this equation:

$$c_{acoust} = \frac{\lambda_0 f}{2n}$$

$$c_{acoust} = \frac{\lambda_0 f}{2\sin\theta} \qquad \textbf{(3.30)}$$

It must be remembered that the presence or not of the inverse proportionality on *n* depends on the exchanged wavevector.

The laser wavelength has a fixed value $\lambda_0$ whose uncertainty is negligible. The frequency shift *f* is usually identified with a best-fit procedure. The uncertainty $\sigma_f$ is attached to the best-fit procedure and mainly depends on the peak intensity. In fact, if the peak is intense, it has a good signal to noise ratio and the central peak value can be identified with small uncertainty. A minor effect is also due to the peculiar shape of the Brillouin peaks. In fact, the shape of these peak is due to the finite aperture of the light collecting lens. As we have explained above, the lens collects the light scattered with all the wavevector directions falling within the solid angle delimited by lens aperture, within a cone around the nominal collection direction $\boldsymbol{q}_s$. In the case of backscattering, this finite collection aperture induces an asymmetry of the peaks which should be taken into account in the identification of the peaks frequency.

The frequency scale of the spectra is also calibrated with finite accuracy. The uncertainty associated with frequency calibration is usually negligible in comparison to the uncertainty derived from the best-fit procedure and can be completely negligible for the most intense and sharp peaks. The refractive index *n* is known to a finite accuracy $\sigma_n$ which depends on the way it is measured. The incidence angle $\theta$ is set to a finite precision $\sigma_\theta$ that depends on the procedure adopted to set up the scattering geometry. The total resulting $\sigma_c$ depends on the uncertainties $\sigma_f$, $\sigma_n$ and $\sigma_\theta$ and it can be expressed through the error propagation formula :

$$\left(\frac{\sigma_c}{c}\right)^2 = \left(\frac{\sigma_f}{f}\right)^2 + \left(\frac{\sigma_n}{n}\right)^2 \qquad \textbf{(3.31)}$$

This Equation becomes, form Equation 3.30,

$$\left(\frac{\sigma_c}{c}\right)^2 = \left(\frac{\sigma_f}{f}\right)^2 + \left(\frac{\sigma_{\sin\theta}}{\sin\theta}\right)^2 \qquad \textbf{(3.32)}$$

where in turn, the last term can be expressed as

$$\frac{\sigma_{\sin\theta}}{\sin\theta} = \frac{1}{\sin\theta}\frac{d\sin\theta}{d\theta}\sigma_\theta = \frac{\sigma_\theta}{\tan\theta} \qquad \textbf{(3.33)}$$

The last equation shows that the same primary uncertainty $\sigma_\theta$ has more severe effects at small incidence angles. These uncertainties have different natures that must be recognized : $\sigma_f$ is the random error in the identification of a peak frequency and $\sigma_\theta$ is the uncertainty due to the random errors in the setting of the scattering geometry. In different measurements they are independent and uncorrelated and tend to be averaged out by repeated measurements. So they contribute to the scatter of results but do not affect the mean value. Therefore they characterize a lack of precision but do not imply a lack of accuracy[4].

On the other hand, the refractive index is a material parameter known to a finite accuracy, but remains the same over repeated measurements. This means that its uncertainty affects the mean value but not the scatter of the results, so it affects accuracy but not precision.

For what concerns $\sigma_f$ , applying the error propagation formula to Equation 3.29, we obtain:

$$\left(\frac{\sigma_f}{f}\right)^2 = \left(\frac{\sigma_{FSR}}{FSR}\right)^2 + \frac{\sigma^2_{n_p^+} + \sigma^2_{n_p^-}}{\left(n_p^+ - n_p^-\right)^2} + \frac{\sigma^2_{n_g^+} + \sigma^2_{n_g^-}}{\left(n_g^+ - n_g^-\right)^2}$$
$$= \left(\frac{\sigma_{FSR}}{FSR}\right)^2 + \left(\frac{\sigma_p}{n_p}\right)^2 + \left(\frac{\sigma_g}{n_g}\right)^2 \qquad \textbf{(3.34)}$$

where the two last terms are the relative uncertainties remaining form the best fit procedures.

[4]The accuracy of a measurement system is the degree of closeness of measurements of a quantity to that quantity's actual (true) value. The precision of a measurement system, also called reproducibility or repeatability, is the degree to which repeated measurements under unchanged conditions show the same results.

The first term on the right side of Equation 3.34 is due to the spacing $d$ that is inversely proportional to FSR. An optical calibration can achieve a relative uncertainty $\sigma_d / d = \sigma_{FSR} / FSR$ below a micrometre over a few millimetres. The term $\sigma_p / n_p$, due to the doublet, depends mainly on the signal to noise ratio. The term $\sigma_g / n_g$, due to the spectral ghosts, is related to the difficulty of adequately describing the particular shape of the ghosts.

The accuracy of a single measurement can be limited but both accuracy and precision can be improved by repeated measurements.

The analysis of the uncertainties must be discussed for the particular geometry because the terms included in Equation 3.34 can change, depending on scattering configuration.

# Chapter 4

In this chapter we are going to give a general description of the principal features of the material which constitutes our sample, titanium dioxide, $TiO_2$. We do this to place the material in the contest of our work, also because it is one of the most used materials in materials science.

The very first part of this chapter is dedicated to the description of the physical and chemical properties of titanium and titanium dioxide, giving a special attention to the crystal structure of the minerals of titanium dioxide, rutile, anatase and brookite. In fact, in this work, we focus on the films characterization so it is very important to know which is the morphology and the crystal structure of the films we probe. For the same reason, we add in this chapter a paragraph concerning bulk and surface defects typical of $TiO_2$, such as oxygen vacancies and step edges.

After having introduced the general properties of the material, in the second part of the chapter, we are going to focus on its electronic structure, whose knowledge is fundamental if we want to understand the most important properties and applications of titanium dioxide. Between these properties there is in particular the photoactivity, which translates in photocatalysis and photoinduced hydrophilicity, two peculiar properties exploited in many technological applications. The third part contains a list of the most widespread applications of $TiO_2$ such as its use as a photocatalyst and in environmental applications, such as in self-cleaning materials and in the treatment of VOCs (volatile organic compounds). The fourth and last part of this chapter contains a description of one of the most important application of $TiO_2$ in photovoltaic cells. First of all we will introduce the general concept of solar cells with their main characteristics such as p-n junction and then we are going to concentrate on the photovoltaic cells developed by M.Gratzel, the so-called DSSC (Dye-Sensitzed Solar Cell), which provide a technically and economically credible alternative to the most diffuse p-n junction devices.

## 4.1 Titanium Dioxide: properties

In this very first part of the fourth chapter we describe the metal whose oxide, titanium dioxide, $TiO_2$, is the constitutive material of the sample analysed in this work. Here we offer a brief description of the physical and chemical properties, of the production process and of the principal application of titanium.
In the second part we begin to occupy of $TiO_2$, describing its main characteristics and its most diffuse minerals that occur in nature, rutile anatase and brookite. Here we describe these three polymorphs of titanium dioxide in terms of crystal structure underlying the main differences between them. Then, we introduce the defects of the $TiO_2$, such as oxygen vacancies and step edges, which are useful to have an idea of the surface and bulk structure of our films.

### 4.1.1 Titanium

Titanium is a chemical element with symbol Ti and atomic number 22. It has been discovered in Great Britain and occurs with a number of mineral deposits, principally rutile and ilmenite which are widely distributed in the Earth's crust and lithosphere. It is found in almost all living things, rocks, water bodies and soils.
Significant titanium-bearing ilmenite deposits exist in western Australia, Canada, China, India, Mozambique, New Zealand, Norway, and Ukraine. Large quantities of rutile are also mined in North America and South Africa.
Titanium is always bonded to other elements in nature. It is the ninth-most abundant element in the Earth's crust (0.63% by mass) and the seventh-most abundant metal. It has different compounds such as titanium dioxide ($TiO_2$), titanium tetrachloride ($TiCl_4$) and titanium trichloride ($TiCl_3$). Titanium dioxide is the most common one and it a popular photocatalyst while the other two compounds are catalyst used to produce smoke screens and polypropylene respectively.
It has an hexagonal compact crystal structure (*hcp*), whose hexagonal alpha form changes into a body-centered cubic (lattice) β form at 882 °C. Similar to zirconium and hafnium, an additional omega phase exists, which is

thermodynamically stable at high pressures, but is metastable at ambient pressures.

The two most useful properties of this metal are corrosion resistance and the highest strength-to-weight ratio of any metal. It is a strong metal with low density that is quite ductile, lustrous, and metallic-white in color. The relatively high melting point (more than 1650 °C) makes it useful as a refractory metal. It is paramagnetic and has fairly low electrical and thermal conductivity. It is fairly hard (although not as hard as some grades of heat-treated steel), non-magnetic and a poor conductor of heat and electricity.

Naturally occurring titanium is composed of five stable isotopes: $^{46}$Ti, $^{47}$Ti, $^{48}$Ti, $^{49}$Ti, and $^{50}$Ti, with $^{48}$Ti being the most abundant (73.8% natural abundance).

The processing of titanium metal occurs in 4 major steps: reduction of titanium ore into "sponge", a porous form; melting of sponge, or sponge plus a master alloy to form an ingot; primary fabrication, where an ingot is converted into general mill products such as billet, bar, plate, sheet, strip, and tube; secondary fabrication of finished shapes from mill products. Because the metal reacts with oxygen at high temperatures it cannot be produced by reduction of its dioxide. For what concerns applications, titanium is used in steel as an alloying element to reduce grain size and as a deoxidizer, and in stainless steel to reduce carbon content. Titanium is often alloyed with aluminium (to refine grain size), vanadium, copper (to harden), iron, manganese, molybdenum, and with other metals. Applications for titanium mill products (sheet, plate, bar, wire, forgings, castings) can be found in industrial, aerospace, recreational, and emerging markets. Powdered titanium is used in pyrotechnics as a source of bright-burning particles. Due to their high tensile strength to density ratio, high corrosion resistance, fatigue resistance, high crack resistance, and ability to withstand moderately high temperatures without creeping, titanium alloys are used in aircraft, armor plating, naval ships, spacecraft, and missiles. Due to its high corrosion resistance to sea water, titanium is used to make propeller shafts and rigging and in the heat exchangers of desalination plants; in heater-chillers for salt water aquariums, fishing line and leader, and for divers' knives. Welded

titanium pipe and process equipment (heat exchangers, tanks, process vessels, valves) are used in the chemical and petrochemical industries primarily for corrosion resistance. Titanium metal is used in automotive applications, particularly in automobile or motorcycle racing, where weight reduction is critical while maintaining high strength and rigidity. Because it is biocompatible (non-toxic and is not rejected by the body), titanium is used in a lot of medical applications including surgical implements and implants. Titanium is non-toxic even in large doses and does not play any natural role inside the human body. An estimated quantity of 0.8 milligrams of titanium is ingested by humans each day, but most passes through without being absorbed.


**Fig. 4.1** Titanium mineral concentrate.

**Fig. 4.2** Titanium dioxide powder.

### 4.1.2 Titanium Dioxide

Titanium dioxide, also known as titanium(IV) oxide or titania, is the naturally occurring oxide of titanium, chemical formula $TiO_2$. Titanium dioxide occurs in nature as well-known minerals rutile, anatase and brookite. The most common form is rutile, which is also the equilibrium form at all temperatures. The metastable anatase and brookite phases both convert to rutile upon heating. Titanium dioxide has eight modifications: in addition to rutile, anatase and brookite, there are three metastable forms produced synthetically (monoclinic, tetragonal and orthorombic), and five high pressure forms ($\alpha$-$PbO_2$-like, baddeleyite-like, cotunnite-like, orthorhombic OI, and cubic phases):

| **Form** | **Crystal system** |
|---|---|
| Rutile | tetragonal |
| Anatase | tetragonal |
| Brookite | orthorhombic |
| $TiO_2$ (B) | monoclinic |
| $TiO_2$ (H) | tetragonal |

| | |
|---|---|
| $TiO_2$ (R) | tetragonal |
| $TiO_2$ (II) ($\alpha$-$PbO_2$ like form) | orthorhombic |
| 7 coordinated Ti (baddeleyite-like form) | monoclinic |
| $TiO_2$-OI | orthorhombic |
| Cubic form | cubic |
| $TiO_2$-OII (cotunnite ($PbCl_2$) like form) | orthorhombic |

**Table 4.1** Titanium dioxide polymorphs and their crystal structure.

Table 4.2 summarizes the general properties of titanium dioxide :

| | |
|---|---|
| Molecular formula | $TiO_2$ |
| Molar mass | 79,866 g/mol |
| Density | 4,23 g/cm$^3$ |
| Melting point | 1843 °C |
| Boiling point | 2972 °C |
| Refractive index | 2,488 (anatase)<br>2,583 (brookite)<br>2,609 (rutile) |

**Table 4.2** Titanium dioxide properties.

### 4.1.3 Rutile, Anatase and Brookite

Rutile is a mineral composed primarily of titanium dioxide, $TiO_2$. Rutile is the most common natural form of $TiO_2$. Brookite and anatase are typical polymorphs[(5)] of rutile formed by retrogression of metamorphic rutile. Rutile has among the highest refractive indices of any known mineral and also exhibits high dispersion. Natural rutile may contain up to 10% iron and significant

amounts of niobium and tantalum. It is the preferred polymorph of $TiO_2$ in many environments because it has the lowest molecular volume of the three polymorphs; it is thus the primary titanium bearing phase in most high pressure metamorphic rocks.

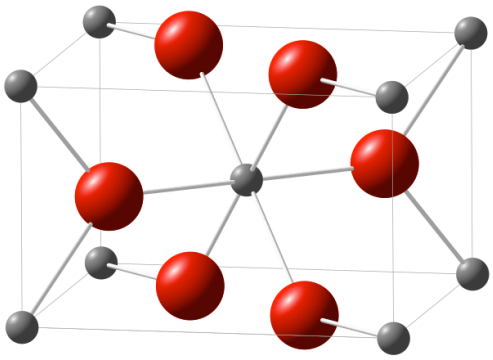

**Fig.4.3** Rutile unit cell. Titanium atoms are grey while oxygen atoms are red.

Rutile has a primitive tetragonal unit cell as it is shown in figure 4.3. The titanium cations have a coordination number of 6 meaning they are surrounded by an octahedron of 6 oxygen atoms. The oxygen anions have a coordination number of 3 resulting in a trigonal planar coordination.
Figure 4.4 shows the tetragonal crystal structure made of slighted distorted octahedral.

(5) Polymorphism in the ability of a solid to exist in nature in more than one form or crystal structure.

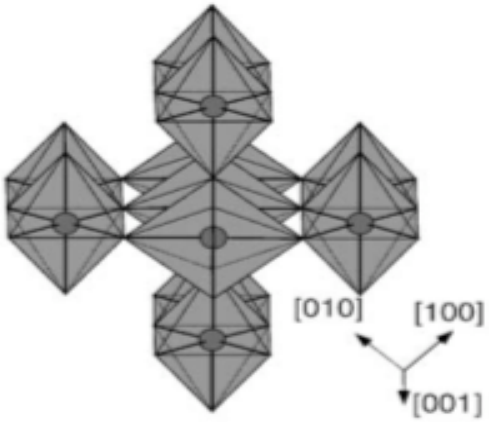


**Fig. 4.4** Rutile octahedra.

Table 4.3 collects the three reticular parameters of the three polymorphous forms of $TiO_2$ :

| Crystal form | Crystal structure | Reticular parameters (Å) | | |
|---|---|---|---|---|
| | | a | b | c |
| rutile | tetragonal | 4,593 | 4,593 | 2,959 |
| anatase | tetragonal | 3,782 | 3,782 | 9,502 |
| brookite | orthorhombic | 9,182 | 5,456 | 5,413 |

**Table 4.3** Principal characteristics of the crystal structure of the three forms of $TiO_2$ .

For what concern the two polymorphous form, anatase and brookite, anatase is always found as small, isolated and sharply developed crystals, and like rutile, the most commonly occurring modification of titanium dioxide, it crystallizes in the tetragonal system. There are also important differences between the physical

characters of anatase and rutile: the former is less hard (5.5-6 vs. 6-6.5 Mohs) and dense (specific gravity[6] about 3.9 vs. 4.2).

Anatase is not an equilibrium phase of $TiO_2$, it is kinetically stabilized. At temperatures between 550° C and about 1000 °C, anatase transforms to the equilibrium rutile phase, increasing its specific gravity to 4.2.

The temperature of this transformation strongly depends on the impurities or dopants present in the material as well as on the morphology of the sample.

Figure 4.5 shows the unit cell of anatase whose parameters have been already collected in table 4.3. The crystal structure is the same of rutile but the octahedra have different degree of distortion. The crystal structure can be observed in figure 4.6.

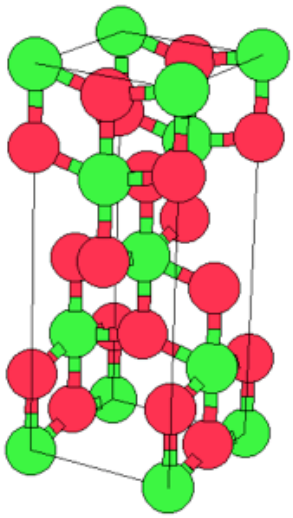

**Fig.4.5** Unit cell of anatse with red atoms of Ti and green atoms of O.

[6] Specific gravity is the ratio of the density of a substance and the density of a reference substance, usually water for liquids and air for gases.

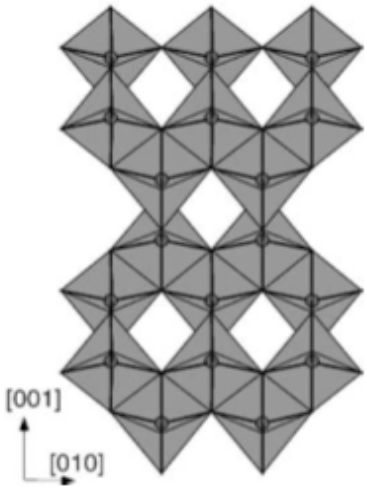


**Fig.4.6** Anatase crystal structure.

In figure 4.7, it is possible to focus on the single octahedron of rutile and anatase with the relative distances in the bond structure.

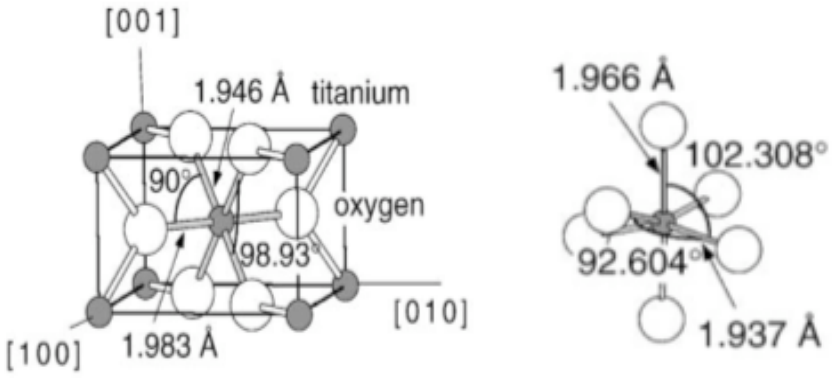


(a) (b)

**Fig.4.7** Rutile and anatase octahedra with Ti atoms in grey, surrounded by the oxygen atoms. (a) Unit cell of rutile with the lengths (Å) of the bonds between atoms; (b) unit cell of anatase where are shown the lengths of the atomic bonds and the angles between atoms.

The structural differences of these two forms of $TiO_2$ reflect on the different densities of the two solids, 4240 kg/m$^3$ for rutile and 3830 kg/m$^3$ for anatase.
Brookite is another one of the three naturally occurring polymorphs of titanium dioxide approved by the International Mineralogical Association (IMA). Brookite is rare compared to anatase and rutile and, like these forms, it exhibits photocatalytic activity. Brookite has a larger cell volume than either anatase or rutile, with 8 $TiO_2$ groups per unit cell, compared with 4 for anatase and 2 for rutile. In fact, brookite has a volume of the unit cell of 257,38 Å$^3$, while rutile volume cell is 62,07 Å$^3$ and anatase one is 136,25 Å$^3$. The structure of anatase is similar to that of rutile. It has tetragonal symmetry and belongs to the same point group, but contains an inversion center perpendicular to the [001] axis that gives it body centered symmetry. As in rutile, the $TiO_6$ octahedra are linked at the corners in an alternating pattern. There is a distortion in the octahedra that causes longer bond lengths along the axial Ti-O bonds than those in the horizontal plane. This distortion is slightly larger for anatase. The brookite structure is more complicated and is the least dense of the three forms. By definition, the brookite structure is of lower symmetry than its $TiO_2$ polymorphs and the dimensions of the unit cell are unequal. Also the Ti-O bond lengths vary more so than in the rutile or anatase phases, as do the O-Ti-O bond angles. Iron Fe, tantalum Ta and niobium Nb are common impurities. At temperatures above about 750 °C, brookite will revert to the rutile structure. Brookite belongs to the orthorhombic dipyramidal crystal class. The formula is $TiO_2$, with 8 formula units per unit cell (Z = 8). The unit cell of brookite can be seen in figure 4.8 :

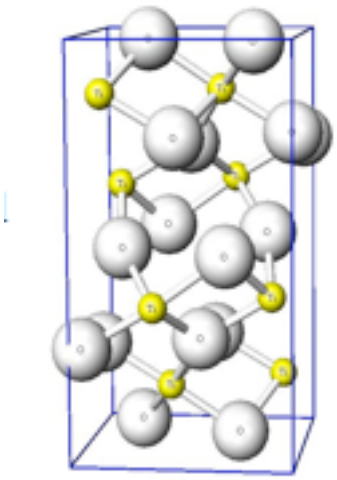

**Fig.4.8** Brookite unit cell with yellow titanium atoms and white oxygen atoms.

The brookite structure is built up of distorted octahedra with a titanium ion at the center and oxygen ions at each of the six vertices. Each octahedron shares three edges with adjoining octahedra, forming an orthorhombic structure. Figure 4.9 shows the crystal structure of brookite :

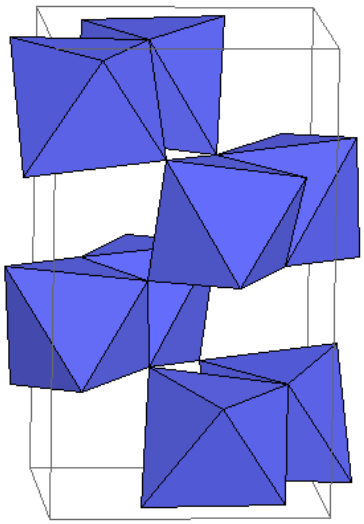

**Fig.4.9** Brookite crystal structure.

Crystals are typically tabular, elongated and striated parallel to their length. They may also be pyramidal, pseudo-hexagonal or prismatic. Brookite is doubly refracting[6], as are all orthorhombic minerals, and it is biaxial. Refractive indices are very high, above 2.5, which is even higher than diamond at 2.42. Brookite is a brittle mineral, with a subconchoidal[7] to irregular fracture and poor cleavage in one direction parallel to the c crystal axis and traces of cleavage in a direction perpendicular to both the a and the b crystal axes.

[6] Birefringence, or double refraction, is the decomposition of a ray of light into two rays when it passes through certain anisotropic materials, such as crystals of calcite or boron nitride.

[7] Subconchoidal fracture is a mineral fracture that falls between conchoidal and even fracture; the first one is a fracture where the indentation is rounded and resembles as a shell and the second one is a fracture that forms a smooth flat surface.

### 4.1.4 Bulk, Surface and Line Defects

The titanium oxygen phase diagram is very rich with many stable phases with a variety of crystal structures. Consequently, $TiO_2$ can be reduced easily. Bulk reduction and the resulting color centers are reflected in a pronounced color change of $TiO_2$ single crystals from initially transparent to light and dark blue (figure 4.10) [7].

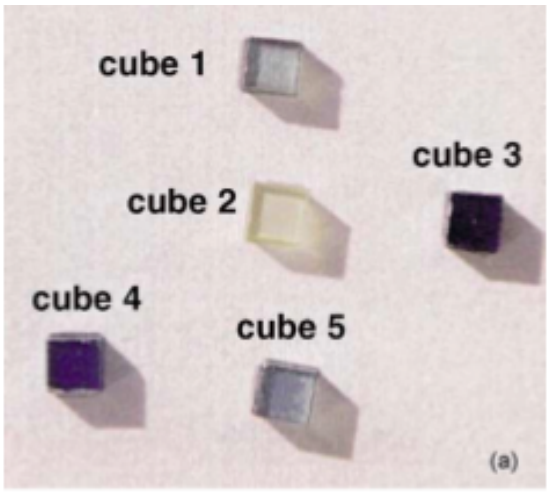


**Fig.4.10** Color centers associated with bulk defects that are formed upon reduction of $TiO_2$ single crystals cause a change in crystal color. Photographs of rutile single crystals heated in a furnace to various temperatures and for various times.

These intrinsic defects result in n-type doping and high conductivity. Bulk defects play a major role in a variety of surface phenomena where annealing to high temperatures is necessary. The relationship between crystal color, conductivity, bulk defects as characterized by EPR (electron paramagnetic resonance) measurements, and surface structure of rutile (110) has been investigated systematically by Li et al.[11]. The bulk structure of reduced $TiO_2$ crystals is quite complex with a various types of defects such as doubly charged

oxygen vacancies, $Ti^{3+}$ and $Ti^{4+}$ interstitials, and planar defects such as CSPs (crystallographic shear planes). The defect structure varies with oxygen deficiency which depends on temperature, gas pressure, impurities. Despite years of research, the question of which type of defect is dominant in which region of oxygen deficiency is still subject to debate. It was shown that the dominant type are Ti interstitials. The diffusion mechanism for the various types of defects is quite different; oxygen migrates via a site exchange (vacancy diffusion) mechanism, while excess Ti diffuses through the crystal as interstitial atoms. The interstitial diffusion happens especially fast through the open channels along the <001> direction (the crystallographic c-axis). A Ti interstitial located in these channels is in an octahedral configuration, similar to the regular Ti sites.

Between surface defects, there are step edges, oxygen vacancies of various origin and line defects. An example of a typical terrace-step structure can be seen in figure 4.11.

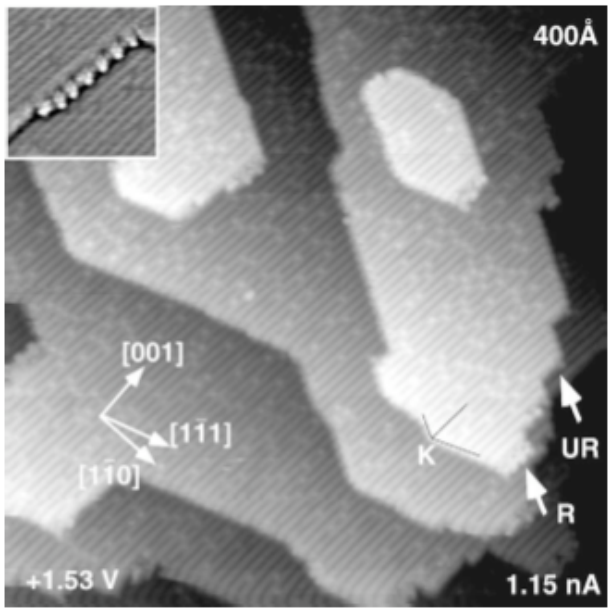


**Fig.4.11** STM image of a clean stoichiometric surface of $TiO_2$ after sputtering and annealing.

Step edges on annealed[8] surfaces run predominately parallel to the <001>- and <111>-type directions. In figure 4.11, a kink site, labeled with K, forms at the point where a different type step edges intersect. Such kink sites are located at the end of dark rows (the bridging oxygens). Figure 4.11 shows two kinds of <001>-type steps: one appears smooth and is labeled with UR while the other one is rugged, labeled with R, that stays for reconstructed, with a higher number of kinks.

The most common point defects are oxygen vacancies, especially on samples sputtered and annealed in UHV (ultra high vacuum). The concentration of vacancies in the bridging oxygen rows is reported as several percent. These defects are of high importance for the surface properties of $TiO_2$. Thermally induced point defects are shown in the AFM (atomic force microscopy) figure 4.12 as black points on the bright oxygen rows.

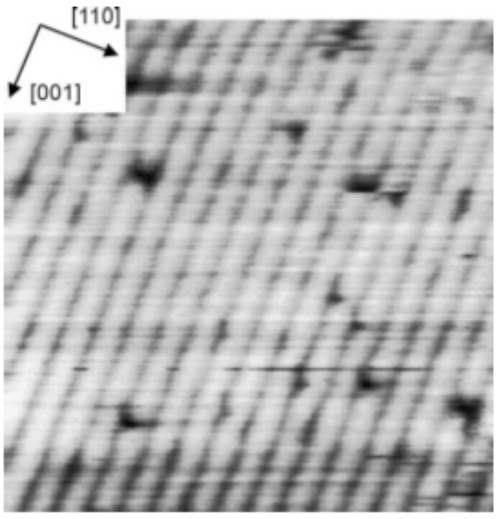


**Fig.4.12** AFM image of a $TiO_2$ surface with the black spots assigned as oxygen vacancies.

[8] Annealing, in metallurgy and materials science, is a heat treatment wherein a material is altered, causing changes in its properties such as strength and hardness. It is a process that produces conditions by heating to above the critical temperature, maintaining a suitable temperature, and then cooling

Oxygen vacancies can also be created by bombardment with electrons, that creates a core hole in the Ti3p level. With a certain possibility, this hole is filled through an inter-atomic Auger process[9] from a neighboring O atom. Such electron-stimulated defects behave somewhat different than thermally excited ones.

Defects can also be created by irradiation with UV light, but nothing is known about their structure.

For what concerns line defects, figure 4.13, STM (scanning tunneling microscope) images of UHV-annealed surfaces, shows dispersed bright strands, typically of several tens of Angstroms long.

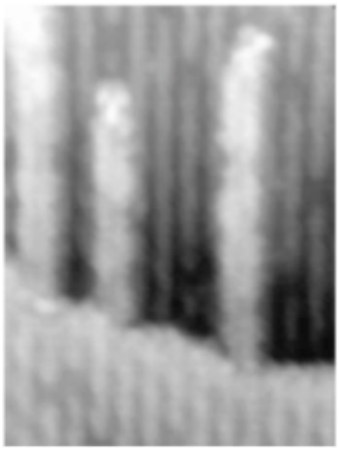

**Fig.4.13** STM image of strings growing out of the upper terrace of a $TiO_2$ rutile surface.

[9]The Auger effect is a physical phenomenon in which the transition of an electron in an atom filling in an inner-shell vacancy causes the emission of another electron. When a core electron is removed, leaving a vacancy, an electron from a higher energy level may fall into the vacancy, resulting in a release of energy. Although sometimes this energy is released in the form of an emitted photon, the energy can also be transferred to another electron, which is ejected from the atom. This second ejected electron is called an Auger electron.

They are distributed across terraces and have a tendency to grow out step edges onto the lower terrace. The presence of such dispersed strands is sample-dependent. Investigations on numerous $TiO_2$ samples have shown that small amount of bulk impurities can also cause strands on the surface.
In general, commercial $TiO_2$ single crystals are quite clean but impurities of different nature can be present. A common impurity that has been investigated is calcium. It tends to segregate to the surface upon high temperature annealing. Typically calcium can be depleted from the near-surface region in a few sputtering[10] /annealing cycles.

[10] Sputtering is a process whereby atoms of a cartain surface are ejected form a solid target because of the bompardament of the target by energetic particles. It is used for thin film deposition, etching and other analythical techniques. The primary particles are supplied in different way, for example by a plasma, an ion source, an accelerator or by a radioactive material.

## 4.2 Titanium Dioxide : electronic structure and photocatalysis

Here we introduce a brief description of electronic properties and structure of titanium dioxide, after having described the main features of semiconductor materials. Generally, titanium dioxide is a semiconducting material which can be chemically activated by light. This section introduces two important properties of titanium dioxide which render this material greatly exploitable for a vaste range of application. They are photocatalysis and photoinduced hydrophilicity. The photoactivity of $TiO_2$ which is known for 60 years has been investigated extensively. Compared with rutile and brookite, anatase shows the highest photoactivity, so in the following, $TiO_2$ always denotes the anatase modification.

### 4.2.1 Electronic Structure and Properties of $TiO_2$

To understand the principle of photocatalysis it must be necessary to know the electronic structure and properties of semiconductors used as photocatalysts.
In general, the behavior of crystal solids is described with the band gap model that can be used to represent the electrons distribution in a solid.
In solid state physics, a band gap, also called energy gap or bandgap, is an energy range in a solid where no electron states can exist. The band gap generally refers to the energy difference (in electronvolts) between the top of the valence band and the bottom of the conduction band in insulators and semiconductors. This is equivalent to the energy required to free an outer shell electron from its orbit about the nucleus to become a mobile charge carrier, able to move freely within the solid material. So the band gap is a major factor determining the electrical conductivity of a solid. Substances with large band gaps are generally insulators, those with smaller band gaps are semiconductors, while conductors either have very small band gaps or none, because the valence and conduction bands overlap.
Electrons are able to jump from one band to another. However, in order for an electron to jump from a valence band to a conduction band, it requires a specific minimum amount of energy for the transition. The required energy differs with

different materials. Electrons can gain enough energy to jump to the conduction band by absorbing either a phonon or a photon. A semiconductor is defined as a material with a small but nonzero band gap which behaves as an insulator at absolute zero but allows thermal excitation of electrons into its conduction band at temperatures which are below its melting point. The conductivity of intrinsic semiconductors is strongly dependent on the band gap. The only available carriers for conduction are the electrons which have enough thermal energy to be excited across the band gap.

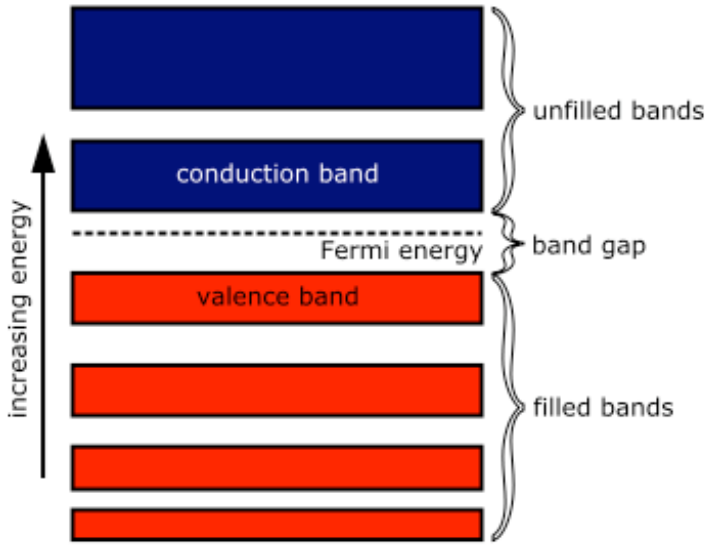


**Fig.4.14** Solids band structure.

Figure 4.14 shows the valence band (VB) and the conduction band (CB), separated by a prohibited region, named band gap, with energy $E_g$ (eV).
The ability of a semiconductor to undergo photoinduced electron transfer to adsorbed particles is governed by the band energy positions of the semiconductor and the redox potentials of the adsorbents. The relevant potential level of the acceptor species is thermodynamically required to be below the

conduction band of the semiconductor. Otherwise, the potential level of the donor is required to be above the valence band position of the semiconductor in order to donate an electron to the empty hole. Figure 4.15 presents the band-edge positions of several semiconductors.

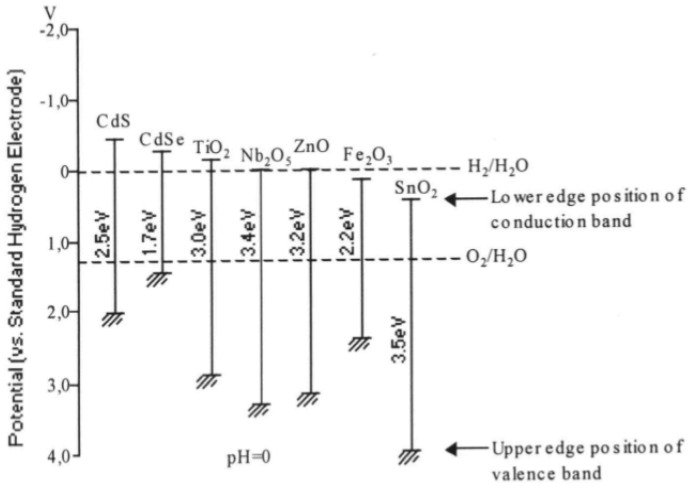


**Fig.4.15** Band edge energies of typical semiconductors.

From the electronic structure point of view, $TiO_2$ is a semiconductor *n*[(11)] with a band gap energy Eg = 3,2 eV for anatase and Eg=3 eV for rutile.

[(11)] Semiconductor *n* refers to n-type doping (see par.4.6.1).

If this material is irradiated with photons of the energy > $E_g$, the band gap is exceeded and an electron is promoted from the valence to the conduction band. Consequently, the primary process is the charge-carrier generation.

In the case of rutile, energy of incident light must be equal or higher than 3 eV while for anatase it must be equal or higher than 3,2 eV.
From equation 4.4 it can be seen that each form of $TiO_2$ can be activated by light with different wavelength :

$$E_g = h\nu = \frac{hc}{\lambda} = \frac{1240}{\lambda} \qquad \textbf{(4.4)}$$

where ν is the frequency of the incident radiation, *c* is the speed of light, λ is the wavelength and the product *hc* is a constant expressed in eVnm.
Anatase is activated by light having λ< 388 nm and rutile by light having λ< 413 nm. This means that, because of high values of $E_g$ of anatase and rutile, can be exploited radiation sources with λ< ≅400 nm. These solids absorb only the UV portion of the electromagnetic spectrum, that corresponds only to the 3-5% of the total solar light spectrum. For this limit, it has been necessary to dope $TiO_2$ with ions of boron, carbon, nitrogen, sulfur and fluorine, to enlarge the region of absorption of the solar spectrum, narrowing the prohibited band. In this way, $TiO_2$ surfaces can be activated also by visible light.

### 4.2.2 $TiO_2$ as a Photocatalyst

In 1972, Fujishima and Honda[10] discovered the photocatalytic splitting of water on $TiO_2$ electrodes. This event marked the beginning of a new era in heterogeneous photocatalysis. Although $TiO_2$ absorbs only approx. 5 % of the solar light reaching the surface of the earth, it is the best investigated semiconductor in the field of chemical conversion and storage of solar energy. In recent years semiconductor photocatalysis using $TiO_2$ has been applied to important problems of environmental interest like detoxification of water and of air.
In chemistry photocatalysis is defined as the acceleration of a photoreaction in the presence of a catalysts. In absence of a catalytic active substance, the oxidation of the most hydrocarbons proceeds rather slowly, which can be

explained by kinetic arguments. A photocatalyst decreases the activation energy of a given reaction.

A heterogeneous photocatalytic system consists of semiconductor particles (photocatalyst) which are in close contact with a liquid or gaseous reaction medium. Exposing the catalyst to light, excited states are generated which are able to initiate subsequent processes like redox reactions and molecular transformations.

Due to their electronic structure, which is characterized by a filled valence band (VB) and an empty conduction band (CB), semiconductors (metal oxides or sulfides as ZnO, CdS, TiO2, Fe2O3, and ZnS) can act as sensitizers for light-induced redox processes.

The heterogeneous photocatalytic oxidation with $TiO_2$ meets the following requirements that could make it competitive with respect to other processes oxidizing contaminants: a low-cost material is used as photocatalyst; the reaction is quite fast at mild operating conditions (room temperature, atmospheric pressure); a wide spectrum of organic contaminants can be converted to water and $CO_2$ and no chemical reactants must be used and no side reactions are produced.

The photocatalysis process can be described in the following way: when a photon with energy of hν exceeds the energy of the band gap an electron (e-) is promoted from the valence band to the conduction band leaving a hole (h+) behind. In electrically conducting materials, for example metals, the produced charge-carriers are immediately recombined. In semiconductors a portion of this photo-excited electron-hole pairs diffuse to the surface of the catalytic particle (electron-hole pairs are trapped at the surface) and take part in the chemical reaction with the adsorbed donor (D) or acceptor (A) molecules. The holes can oxidize donor molecules whereas the conduction band electrons can reduce appropriate electron acceptor molecules.

A characteristic feature of semiconducting metal oxides is the strong oxidation power of their holes h+. They can react in an one-electron oxidation step with water to produce the highly reactive hydroxyl radical (-OH). Equation 4.5 contains the reactions considered. Both the holes and the hydroxyl radicals are very powerful oxidants, which can be used to oxidize most organic

contaminants.

$$H_2O + h^+ \rightarrow {}^{-}OH + H^+$$
$$O_2 + e^- \rightarrow O_2^- \qquad \textbf{(4.5)}$$

Equation 4.5 shows the formation of radical hydroxyl $^{\cdot}OH$ and ion superoxide $O^{\cdot}_2$. Figure 4.16 present an example of the operation of a photochemical excited particle of $TiO_2$ :

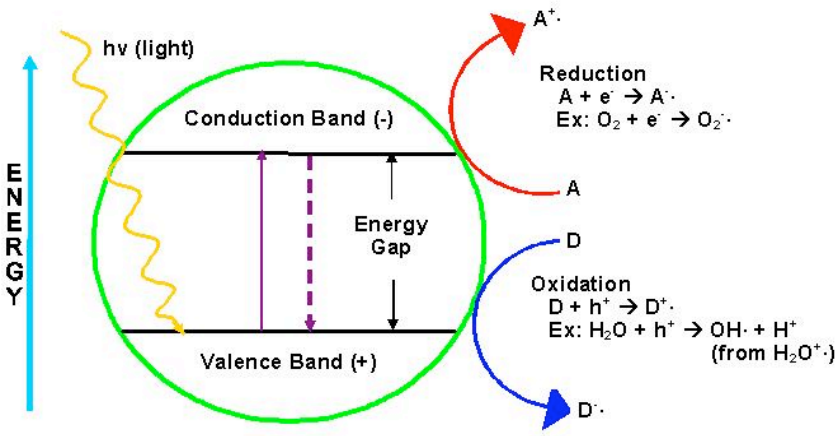


**Fig. 4.16** Mechanism of photocatalisys.

As it has been introduced above, photocatalysis began to be a phenomenon of interest since the late 1960s, when A. Fujishima began to investigate on the photoelectrolysis of water using a single n-type $TiO_2$ (rutile) semiconductor electrode. $TiO_2$ has been chosen because of its sufficiently positive valence band edge to oxidize water to oxygen and because of its stability in presence of aqueous electrolyte solution.

The possibility of solar photoelectrolysis was demonstrated for the first time in 1969 when the system which was exposed to UV light and was connected to a platinum counter electrode through an electrical load.When the surface of the rutile $TiO_2$ electrode was irradiated with light consisting of wavelengths shorter than its band gap (about 400 nm for 3,2 eV), photocurrent flowed from the

platinum counter electrode to the $TiO_2$ electrode through the external circuit. The direction of the current revealed that the oxidation reaction occurs at the $TiO_2$ electrode and the reduction reaction at the Pt electrode. This observation shows that water can be decomposed into oxygen and hydrogen using UV light, without the application of an external voltage.

In 1980s, photocatalytic water splitting has been studied intensively with powdered anatase $TiO_2$ suspensions, with Pt deposited on $TiO_2$ as a cathodic catalyst. Although there were many experiments for simultaneous production of $H_2$ and $O_2$ in the powder systems, either such experiments could not be reproduced or the reaction efficiency was very low. It has been demonstrated that this reaction could not proceed in the powder systems because the produced $H_2$ and $O_2$ might recombine to regenerate other molecules of water, because the production sites of each gas are close to each other. To solve this problem, organic compounds have been added to the aqueous suspension of platinized $TiO_2$. In this case water is reduced, producing $H_2$ at the Pt sites and the organic compounds, such as ethanol, are oxidized instead of water by photogenerated holes at the $TiO_2$ sites. The $H_2$ production was surprisingly efficiently, with anatase that in general gives better results than rutile for hydrogen production in powder photocatalysis. This is probably due to the higher reduction potential of photogenerated electrons in the former than in the latter.

Even if the reaction efficiency is very high, $TiO_2$ can absorb only UV light, which is only about 3% of the solar spectrum. Therefore, from the point of view of the $H_2$ production, $TiO_2$ photocatalysis is not very attractive.

Instead, the research shifted to the utilization of the strong photoproduced oxidation powder of $TiO_2$ for the destruction of pollutants. In the 1980s, detoxications of many harmful compounds in both water and air were demonstrated using powered $TiO_2$ as potential purification methods of waste water and polluted air. In this case the reduction reaction was not necessarily hydrogen production anymore. Now both the reduction and oxidation sites are located on $TiO_2$ surfaces and the reduction of adsorbed oxygen molecules proceeds on $TiO_2$ surfaces. It must be said that, although many research studies were conducted on the purification of waste water and polluted air, $TiO_2$ photocatalysis could not be developed to the stage of a real industrial technology

in the 1980s.
In 1990, have been determined the reasons why $TiO_2$ photocatalysis could not be a practical technology. It is fundamentally inadequate to utilize $TiO_2$ photocatalysis for either energy acquisition or the treatment of huge amounts of water and/or air, because light energy is low and, in addition, $TiO_2$ can utilize only the small amount of UV light contained in solar light. Based on such understanding, K.Hashimoto and others[10] conceived the idea of applying photocatalysis targeting only substances adsorbed originally on surfaces. This means that only substances existing on two-dimensional surfaces can be the object of decomposition, instead of those in three-dimensional spaces such as water and air. In this case, the absolute amounts of the substances decrease and thus the rather weak UV light existing in an ordinary environment could be a sufficient light source for maintaining the $TiO_2$ surface clean. In this way it has been obtained the concept of auto-cleaning materials coated with $TiO_2$ film photocatalysts [13].

### 4.2.3 Photo-induced Hydrophilicity: water wettability of titanium dioxide surface

While investigating the new concept of light-cleaning materials coated with $TiO_2$ film photocatalyst under weak UV light, the same scientists found in 1995 a marked change in water wettability of the $TiO_2$ surface before and after UV irradiation.
The wetting of a solid with water, where air is the surrounding medium, is dependent on the relation between the interfacial tensions (water/air, water/solid and solid/air). The ratio between these tensions determines the contact angle $\theta$ between a water droplet on a given surface. The surface wettability is in general evaluated by the water contact angle (CA). The CA ($\theta$) is defined as the angle between the solid surface and the tangent line of the liquid phase at the interface of the solid-liquid-gas phases. A contact angle of 0° means complete wetting, and a contact angle of 180° corresponds to complete non wetting. The higher this angle the lower is the value of the adhesion work. Decreasing of the contact angle leads to enlarged values of the adhesion work: these are called hydrophilic

surfaces.

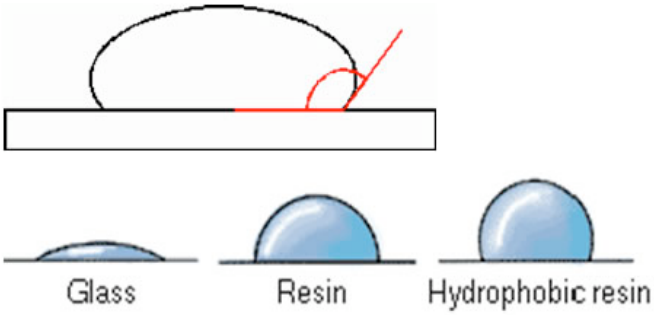


**Fig. 4.17** Contact angle of the surface of materials. Super Hydrophilicity: CA<5°; Hydrophilicity CA<30°; Hydrophobicity : CA>90° ;Super Hydrophobicity :CA>150°.

A $TiO_2$ thin film exhibits an initial CA of several tens of degrees depending on the surface conditions mainly surface roughness. When this surface is exposed to UV light, water starts to exhibit a decreasing CA, that is, it tends to spread out flat instead of beading up. Finally the CA reaches almost 0° as figure 4.15 shows. In this case the surface becomes completely non-water-repellant and it is termed highly hydrophilic.

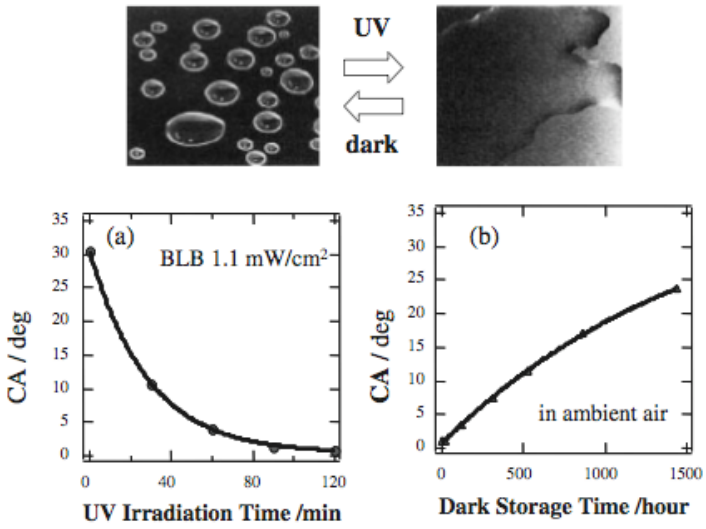


**Fig.4.18** Changes in CA of $TiO_2$ surface (a) under UV irradiation and (b) in the dark.

The surface in question retains a CA of a few degrees for a day or two under the ambient condition without being exposed to UV light. Then the CA slowly increases and the surface turns out to be less hydrophilic again. At this stage, the high hydrophilicity can be recovered simply by exposing the surface again to UV light. Thus, this type of $TiO_2$-coated material is the only known practical highly hydrophilic one that shows stable and semi permanent properties.

This hydrophilic conversion originates from the clean surface produced by the decomposition of staining compounds adsorbed through the conventional photocatalytic oxidation. This is because metal oxides have large surface energies in general, and thus, we considered that a clean $TiO_2$ surface could be essentially hydrophilic. However, it is important to note that a completely clean surface cannot be obtained by the photocatalytic reaction, because the surface is easily contaminated by airborne stains under the ambient condition. K. Hashimoto and others have obtained that this highly hydrophilic state is not a simple clean surface but is a structurally changed metastable one [10].

Figure 4.19 shows an example of the structural changes on $TiO_2$ surfaces irradiated with UV light. This figure shows FEM images of rutile single crystal before and after UV irradiation. Before UV irradiation no difference in contrast was observed, indicating homogeneous wettability. After UV irradiation, the hydrophilic (bright) and the hydrophobic (dark) areas can be clearly observed. It has been concluded that the nanoscale separation between the hydrophilic and hydrophobic phases accounts for the highly hydrophilic characteristics on the $TiO_2$ surface.

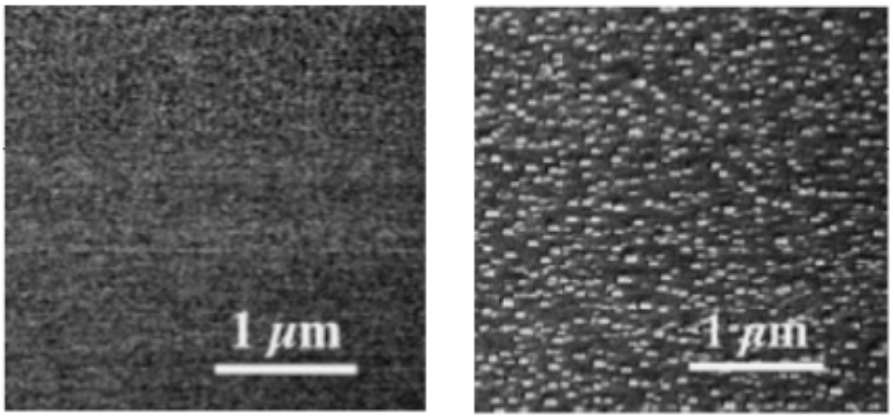


**Fig.4.19** FEM images of rutile single crystal surface before and after UV irradiation.

The finding of photo-induced hydrophilicity has widened the application range of $TiO_2$-coated materials. The stains adsorbed on the $TiO_2$ surface can be easily washed by water because water soaks between stain and the high hydrophilic surface. This has removed the limitation of the cleaning function of the $TiO_2$ photocatalysis, which function is limited by the number of photons. Even though the number of photons is not sufficient to decompose the adsorbed stains, the surface is maintained clean when water is supplied there. The $TiO_2$-coated materials, that are commonly called photocatalytic building materials, are usually used outdoors, as exterior tiles, glass, aluminum walls, have already begun to be commercialized.

Another function blessed with the photo-induced hydrophilicity is the anti-fogging function. The fogging of surfaces of mirror and glass occurs when steam cools down to form many water droplets. On a highly hydrophilic surface no water droplets are formed but a uniform thin film of water is formed on the surface. This uniform film can prevent the fogging.

## 4.3 Titanium Dioxide: some technological applications

There is an extremely wide range of application of titanium dioxide because of its efficient photoactivity and its high stability and low cost.
The two most important photo-induced phenomena, introduced in the last paragraph, photocatalytic activity and superhydrophilicity, can take place simultaneously on the same $TiO_2$ surface. Depending on the composition and the processing, the surface can have more photocatalytic character and less superhydrophilic character or vice versa. The studies conducted on $TiO_2$ surface are able to explain these phenomena and also measurements done to obtain information about surface morphological behavior and vibrational behavior can be used to characterize the surface and its ability to support one phenomenon or both.
Here we present some applications of $TiO_2$ based on these characteristics phenomena, especially the $TiO_2$ application in photovoltaic cells. In this case, $TiO_2$ is used in form of nanocrystals and a large internal surface of the nanocrystalline layers, which is one prerequisite for a good solar cell performance, can only be achieved by adjusting the respective size of the nanoparticles. The coating and heating processes, and the obtained crystal structure of titanium dioxide also play a major part in the preparation of highly efficient devices.

### 4.3.1 Design of nanostructures of $TiO_2$ for highly sensitive hydrophilicity

$TiO_2$ has already been applied to indoor use with the aid of either silver and copper for anti-bacterial purpose. A photocatalytic decomposition reaction can be applied to microorganisms. Escherichia coli cells can completely disappear after about one week under a UV irradiation of 1 $mW/cm^2$. However, the typical indoor UV light intensity are lower, of the order of $nW/cm^2$, so the deactivation of microorganisms takes much longer time under indoor conditions than in outdoor ones. Another way to apply $TiO_2$ for its hydrophilic properties to an

indoor use is the production of highly sensitive $TiO_2$ that undergoes highly hydrophilic conversion. As the reconstruction of surface OH groups is responsible of the hydrophilic conversion, different types of hydrophilic behaviour are expected to be observed among the different crystal faces. In fact, the (100) and (110) faces of a rutile single crystal exhibit a higher hydrophilicity than the (001) face (see figure 4.20) because the former have two-fold oxygens which are higher in positions and more reactive than their surrounding atoms and they are called "bridging site oxygens", whereas the latter has three-fold oxygens which are lower in positions and more inactive.

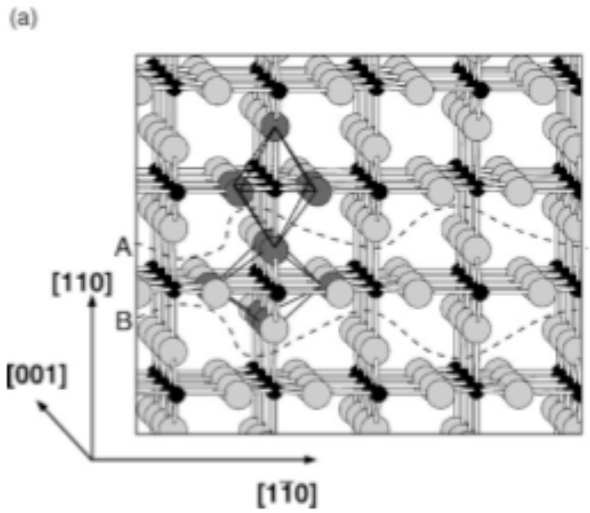


**Fig.4.20** Ball-and-stick model of the rutile crystal structure. It is composed of slightly distorted octahedra, two of which are indicated. Along the [1 1 0] direction these octahedra are stacked with their long axes alternating by 90°. Open channels are visible along the [0 0 1] direction.

Therefore, the (100) and the (110) faces are favorable for increasing the number of OH groups. To obtain the appropriate faces, the photoetching technique was applied to the (001) face of a rutile single crystal. In this way, a large number of rectangular porous holes emerged with a fairly regular arrangement[15] . This rectangular porous surface increased the sensitivity of the photo-induced

hydrophilic reaction and achieved a high hydrophilicity under UV light irradiation of 1 $\mu W/cm^2$, whereas the surface without a photoetching did not. Because the surface roughness enhances the hydrophilicity, the high sensitization for hydrophilic conversion by the photoetching treatment was caused by the exposure of faces with bridging site oxygens and the increase in surface roughness. The high sensitization of $TiO_2$ under weak UV light is expected to increase the application areas to indoor conditions.

### 4.3.2 Environmental Applications

Environment pollution, including water, air and soil, is becoming a serious problem today. There have been many reports about the possibility to apply photocatalysis to pollution clean-up. However, the purification of a three-dimensional space is much more difficult than that of a two-dimensional surface of building materials due to the following two reasons. One is that the phtocatalytic reactions are surface reactions and so the reactants must be captured by the photocatalyst surface. The other is that the total amount of reactant is higher in a three-dimensional space than on a two-dimensional surface, indicating that much more light energy is necessary for the purification of the three-dimensional space.

Some scientists[10] have recently succeeded in the construction of a practical purification system for wastewater form agriculture and soil polluted by volatile organic compounds (VOCs). These systems are based on $TiO_2$ photocatalysis and utilize only solar energy. Because the concentration of environmental pollutants are low in general, the UV light contained in sun light is sufficiently strong to decompose them by $TiO_2$ photocatalysis, if it is possible to collect the light from a broad area. In this application is important to use nanosized $TiO_2$ photocatalyst powders dispersed on substrates with very large areas and spreading them on the ground widely to collect sunlight.

Another application consists in the detoxification of wastewater [13] used for rice hull disinfection. Disinfection solutions for rice hulls (to stop the spread of plant diseases) contain agricultural chemicals. The corresponding wastewater is mostly disposed of by pouring onto the ground, which causes soil pollution.

K. Hashimoto at al. have developed a glass wool mat with a large surface area deposited with very photoactive $TiO_2$ nanoparticles. They were able to show that the wastewater solution is easily purified using the photocatalytic mat under only solar light. The wastewater solution is pored onto mats and the agricultural chemicals are decomposed under sunlight in a few days. In particular, it has been measured that the total initial organic carbon (TOC) values decreased from several hundreds of ppm to nearly zero.

It has become very interesting the application of photocatalytic $TiO_2$ in the treatment of VOC (Volatile chlorinated organic compounds)-polluted soil. In general the most common method of treating the polluted soil is either the simple replacement with clean soil or the heating of the soil to volatilize VOCs, but these methods do not truly purify the environment.

It have been developed photocatalytic sheets to purify the polluted soil on the ground using sunlight. As figure 4.19 shows, the polluted soil is dug up and covered with the sheet, which is made of corrugated paper containing both $TiO_2$ powder adsorbed on activated carbon powders. Then the covered soil is heated volatilizing the pollutant gases captured by adsorption on activated carbon incorporated in the sheet material. The sheet is allowed to stay under sunlight while $TiO_2$ in the sheet decomposes the pollutants completely by photocatalytic reaction.

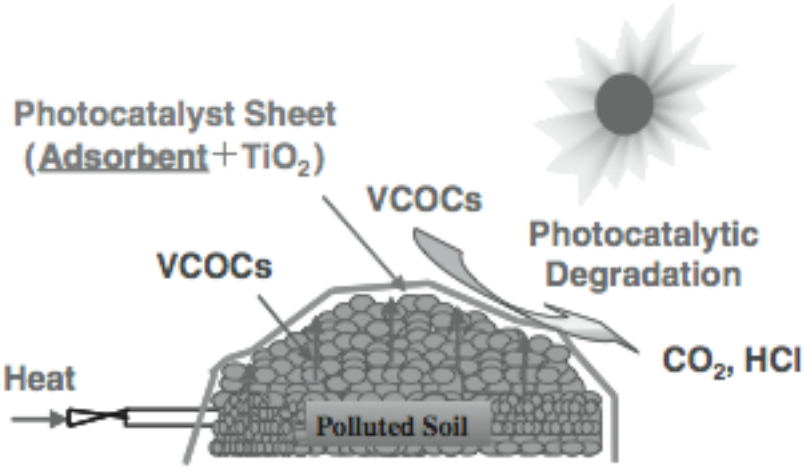


**Fig.4.21** Purification method for polluted soil using solar light and $TiO_2$ sheets.

### 4.3.3 Photocatalytic Sterilization and Photocatalytic Cancer Treatment

As already mentioned, $TiO_2$ photicatalysis can be used to kill bacteria and so can be prepared self-sterilizing surfaces[13]. An example of this application are those carried out with suspensions of Escherichia coli. It has been demonstrated that in these suspensions illuminated with an UV light, no cells survive after only one hour of illumination.

Cancer treatment is one of the most important topics associated with photocatalysis. Some scientists[12] developed a device to allow the cancer to be exposed to light while titanium dioxide powder was being added to the tumor. This device, built by modificating an endoscope, should make it possible to access various parts of the human body. There are still some problem to be solved before such a device can be put into practical use. However, because the photocatalytic reactions only occur under illumination it is possible to selectively destroy cancer cell, if there is a technique available for illumination of the tumor. Obviously, the excitation light should not cause mutations in normal cells.

### 4.3.4 Efficient water evaporation from hydrophilic surfaces

An effective method to prevent the so-called heat island phenomenon is increasing the area of green tract land or the surface area of water. This phenomenon is due to the temperature increase, that is caused by the rapid increase in the absorption of solar energy, due to the coverage of the ground surface by buildings and roads, and by the increase in energy consumption, due to the heat emissions from traffic and air conditioners. A way to solve this problem is the construction of artificial lakes or the cultivation of rooftop plants. However, it is very difficult to secure green tract land and water surfaces so, it has been proposed a method of securing water surfaces by continuously sprinkling water onto the surfaces of buildings that will be covered with a $TiO_2$ photocatalyst. The surface covered with $TiO_2$ photocatalyst becomes highly hydrophilic and plays an important role in minimizing the amount of required sprinkling water to form a water film. It is important to underline that the buildings are not cooled by water itself but by the latent heat flux derived from water evaporation. The cooling of the building surfaces also results in the reduction in the amount of electricity consumed for air conditioning (by ten to several tens of percentage). Therefore, $TiO_2$ coated materials could also contribute to the development of energy-saving technologies.

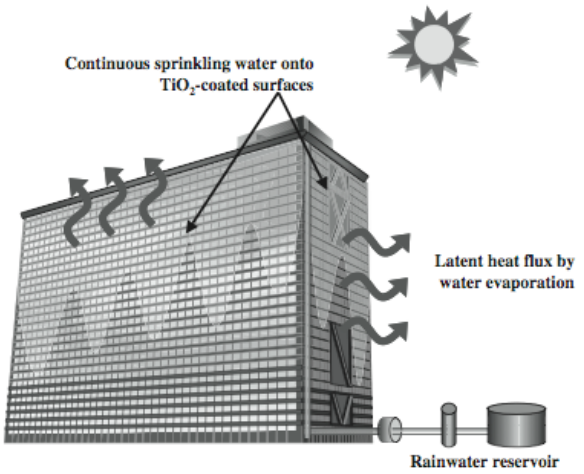


**Fig.4.22** Energy-saving system using solar light and stored rainwater.

## 4.4 A Special Application: photovoltaic cells

Nanomaterials used for gathering solar energy inevitably involve charge transport process. This process is of a great importance for all electronic devices, included solar cells. The transport behaviour is attributed to the carrier (electron) concentration and mobility. The high electron mobility in $TiO_2$ relies on the high crystallinity of the lattice, which is related to the preparation conditions. In fact it can be controlled via varying the reaction temperature ands solvents used in the solvothermal method[18] that is a facile route for direct synthesis of nano-$TiO_2$. Another exploited method is a sol-gel process used to produce titanium dioxide nanoparticles thin layers. In this case titanium dioxide particles have a diameter of about 100 nm, larger than that of nanoparticles produced with other methods. It has been demonstrated that a large internal surface of the nanocrystalline layers is one of the prerequisites of a good solar performance and and can be achieved by adjusting the respective size of nanoparticles.

Some scientists [20] have developed the new concept of packing factor, PF, a criterion for ranking the charge separation abilities of semiconductors. This concept can be used to evaluate inherently existing internal fields that can be used to rank the charge separation abilities among oxide materials. The concept is based on the idea that lower elastic stiffness can promote distortion, which promotes internal fields. Low PF value results in lower elastic stiffness, higher internal field, more efficient light-induced electron-hole separation and transport, and, consequently, a higher photocatalytic activity. The packing factor is computed by dividing the sum of spherical volumes of the ions that form the compound by the unit cell volume. These factors has been calculated for $TiO_2$ polymorphs and they are PF=0,6455 for anatase and PF=0,7045 for rutile. The packing factor model can explain why $TiO_2$ anatase, with its loosely packed structure and more efficient electron-hole separation, is favorable for photocatalytic activity.

Nanocrystalline $TiO_2$, particularly in the anatase phase, has been extensively investigated as a potential material for dye-sensitized solar cells (DSSCs). This high light-to-electricity energy conversion efficiency is attributed to the novel physicochemical properties of mesoporous $TiO_2$, which include high surface area, uniform nanochannels, and a homogeneous nanocrystalline structure. The high surface area adsorbs large quantities of the sensitized dye, resulting in the generation of a higher photocurrent density. A significant influence of the mesopore structure on photovoltaic performance was also observed.

### 4.4.1 General Characteristic of Solar Cells

A solar cell, also called photovoltaic cell is a solid state electrical device that converts the energy of light directly into electricity by the photovoltaic effect. that is defined as the creation of voltage or electric current in a material upon exposure to light. The photovoltaic effect differs in that electrons are transferred between different bands (from the valence to conduction bands) within the material, resulting in the buildup of voltage between two electrodes. Assemblies of solar cells are used to make solar modules which are used to capture energy from sunlight. When multiple modules are assembled together, the resulting integrated group of modules all oriented in one plane is called, in the solar industry, solar panel.

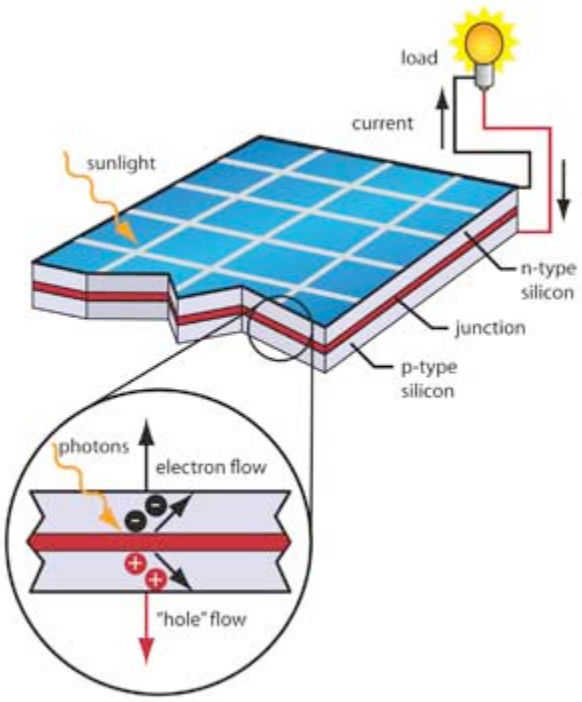


**Fig.4.23** Example of a common solar cell used for electricity production.

Photovoltaic cells are based on the physical processes by which light is converted into electrical current when striking a suitable semiconductor device. When a photon hits the solar panel, it is absorbed by the semiconducting material, such as silicon, and transfers to an electron in the absorbing material. Usually this electron is in the valence band, and is tightly bound in covalent bonds between neighboring atoms, and hence unable to move far. The energy given to it by the photon excites it into the conduction band, where it is free to move around within the semiconductor. The covalent bond that the electron was previously a part of now has one fewer electron, that is known as a hole. The presence of a missing covalent bond allows the bonded electrons of neighboring atoms to move into the hole, leaving another hole behind, and in this way a hole can move through the lattice. Thus, it can be said that photons absorbed in the semiconductor create mobile electron-hole pairs.

The most commonly known solar cell is a large area p-n junction made of silicon. A p-n junction is formed at the boundary between a p-type and a n-type semiconductor created in a single crystal semiconductor by doping. A p-type semiconductor is obtained by adding atoms called acceptors (atoms of elements with a valence number of electron that is lower than that of silicon, such aluminium or boron), in order to increase the number of free charge carriers (in this case positive holes). A n-type semiconductor is obtained by adding atoms called donors (which have a valence number of electrons that is higher than that of the original semiconductor, such as phosphorus) to provide extra conduction electrons. If a piece of p-type silicon is placed in intimate contact with a piece of n-type silicon, then a diffusion of electrons occurs from the region of high electron concentration (the n-type side of the junction) into the region of low electron concentration (the p-type side of the junction). When the electrons diffuse across the p-n junction, they recombine with holes on the p-type side. The diffusion of carriers does not happen indefinitely, however, because charges build up on either side of the junction and create an electric field. The electric field creates a diode that promotes charge flow, known as drift current, that opposes and eventually balances out the diffusion of electrons and holes. This region where electrons and holes have diffused across the junction is called the depletion region because it no longer contains any mobile charge carriers. It is also known as the space charge region.

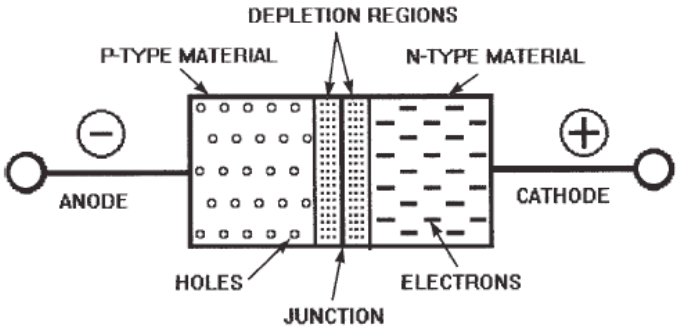


**Fig.4.24** A p-n junction in thermal equilibrium with zero-voltage applied.

Materials presently used for photovoltaic solar cells include monocrystalline silicon, polycrystalline silicon, amorphous silicon, cadmium telluride, and copper indium selenide/sulfide. Many currently available solar cells are made from bulk materials that are cut into wafers between 180 to 240 micrometers thick that are then processed like other semiconductors. Other materials are made as thin-films layers, organic dyes, and organic polymers that are deposited on supporting substrates. A third group are made from nanocrystals and used as quantum dots (electron-confined nanoparticles). Silicon remains the only material that is well-researched in both bulk and thin-film forms.

### 4.4.2 DSSC: Dye-Sensitized Solar Cells

The dye-sensitized solar cells[21] provide a technically and economically credible alternative concept to present day p-n junction photovoltaic devices. In this case, in contrast to conventional systems where the semiconductor assumes both the task of light absorption and charge carrier transport, these two functions are separated. Light is absorbed by a sensitizer, which is anchored to the surface of a wide band semiconductor. Charge separation takes place at the interface via photo-induced electron injection from the dye into the conduction band of the solid. Carriers are transported in the conduction band of the semiconductor to the charge collector. Figure 4.25 shows a schematic presentation of the operating principle of the DSSC .

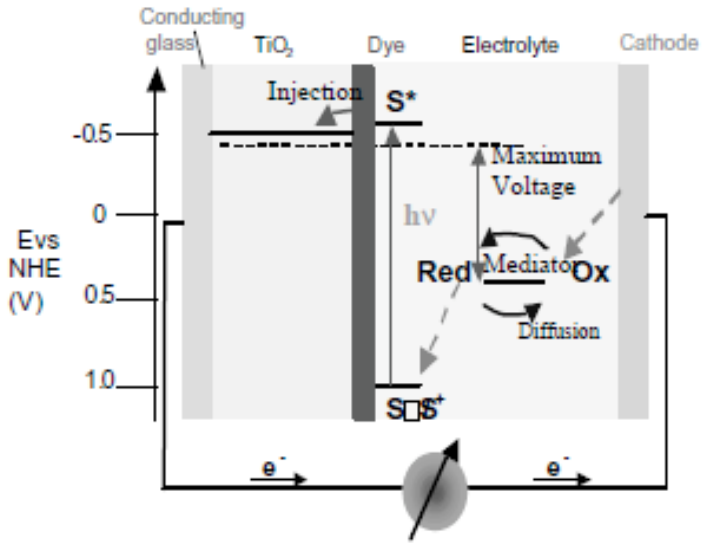


**Fig.4.25** Principle of operation and energy level scheme of a dye-sensitized nanocrystalline solar cell.

At the heart of the system there is a mesoporous oxide layer composed of nanometer-sized particles which have been sintered together to allow for electronic conduction to take place. The material of choice has been $TiO_2$ anatase, but, alternatively, also wide band gap oxides as ZnO have been investigated. $TiO_2$ has many advantages for sensitized photo chemistry and photo electrochemistry: it is a low cost, widely available, non toxic and biocompatible material.

Figure 4.26 shows a SEM image of a nanocrystalline $TiO_2$ (anatase) film used in DSSC cells. In general, these films are 5-20 μm thick and show a porosity of about 50-60% with the average pore size being of few nanometer. Anatase $TiO_2$ is photochemically more active than rutile and has a larger bandgap (3.29 eV vs. 3.05 eV) which prevents a bandgap absorption of blue light by $TiO_2$ particles.

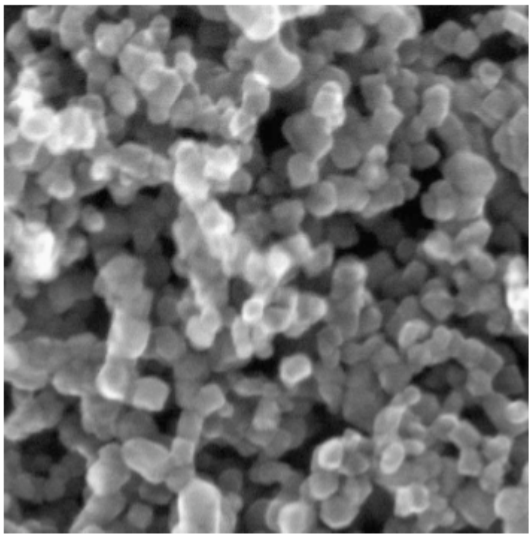

**Fig.4.26** Scanning electron microscope image of a $TiO_2$ film.

The thickness of the $TiO_2$ layers is an important parameter for optimizing the cell efficiencies. Thick layers (>10 μm) show high light absorption, but have also higher recombination losses compared to thin layers (<5 μm) due to larger distances to the current collecting electrodes.

Attached to the surface of the nanocrystalline film is a monolayer of the charge transfer dye. Photo excitation of the latter results in the injection of an electron in the conduction band of the oxide. The original state of the dye is subsequently restored by electron donation from the electrolyte, usually an organic solvent containing redox system, such as iodide. As in a conventional alkaline battery, an anode (titanium dioxide) and a cathode (platiunm) are placed on either side of the liquid electrolyte solution.

In the case of the original Grätzel and O'Regan design, the cell has 3 primary parts. On top is a transparent anode made of fluoride-doped tin dioxide ($SnO_2$:F) deposited on the back of a (typically glass) plate. On the back of this conductive plate is a thin layer of titanium dioxide ($TiO_2$), which forms into a highly porous structure with an extremely high surface area. $TiO_2$ only absorbs a small fraction of the solar photons (those in the UV). The plate is then immersed in a mixture

of a photosensitive ruthenium-polypyridine dye (also called molecular sensitizer) and a solvent. After soaking the film in the dye solution, a thin layer of the dye is left covalently bonded to the surface of the $TiO_2$. A separate plate is then made with a thin layer of the iodide electrolyte spread over a conductive sheet, typically platinum metal. The two plates are then joined and sealed together to prevent the electrolyte from leaking. Although they use a number of advanced materials, these are inexpensive compared to the silicon needed for normal cells because they require no expensive manufacturing steps. Figure 4.27 shows an example of this kind of cheaper solar cells.

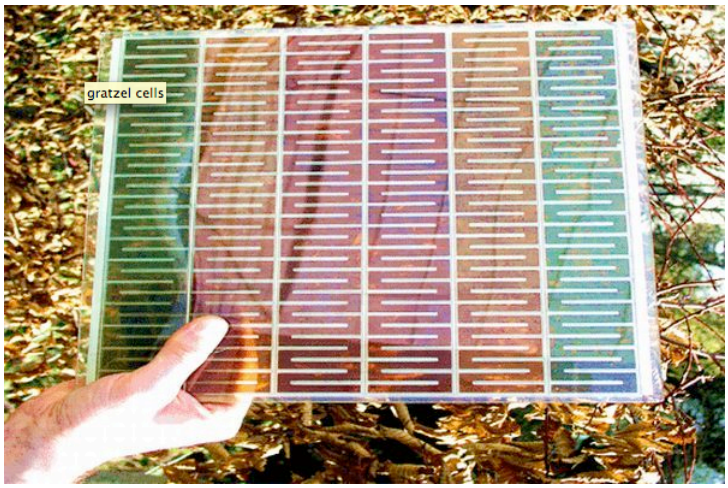


**Fig.4.27** An example of Gratzel cells: these cells are generally coated with dye that enhances the amount of light that is absorbed thus making the solar cells more efficient to use.

From the operational point of view, sunlight enters the cell through the transparent $SnO_2$:F top contact, striking the dye on the surface of the $TiO_2$. Photons striking the dye with enough energy to be absorbed, create an excited state of the dye, from which an electron can be injected directly into the conduction band of the $TiO_2$. From there it moves by diffusion (as a result of an electron concentration gradient) to the clear anode on top. Meanwhile, the dye

molecule has lost an electron and the molecule will decompose if another electron is not provided. The dye strips one from iodide in electrolyte below the $TiO_2$, oxidizing it into triiodide. This reaction occurs quite quickly compared to the time that it takes for the injected electron to recombine with the oxidized dye molecule, preventing this recombination reaction that would effectively short-circuit the solar cell. The triiodide then recovers its missing electron by mechanically diffusing to the bottom of the cell, where the counter electrode re-introduces the electrons after flowing through the external circuit. The voltage generated under illumination corresponds to the difference between the Fermi level of the electron in the solid and the redox potential of the electrolyte, that is indicated in figure 4.25 with a dashed line. Generally the Gratzel's cell has a voltage of 0,4 V and a currents achieved during operational conditions are between 16 and 20 $mA/cm^2$. Overall, the device generates electric power from light without suffering any permanent chemical transformation.

DSSCs are currently the most efficient third-generation solar technology available, with an overall conversion efficiency of about 11%. Other thin-film technologies have efficiencies between 5% and 13%, and traditional low cost commercial silicon panels operate between 12% and 15%. This makes these cells attractive for the so called low density applications, such as rooftop solar collectors, where robustness and light weight of the glass-less collector is a major advantage. A practical advantage that one DSSCs share with most thin-film technologies, is that the cell's mechanical robustness indirectly leads to higher efficiencies in higher temperatures. In any semiconductor, increasing temperature will promote some electrons into the conduction band. However, the DSSC cells may not be as attractive for large scale deployments where higher-cost higher-efficiency cells are more viable.

There is another area where DSSCs are particularly attractive. The process of injecting an electron directly into the $TiO_2$ is qualitatively different to that occurring in a traditional cell, where the electron is promoted within the original crystal. In theory, given low rates of production, the high-energy electron in the silicon could re-combine with its own hole, giving off a photon (or other form of energy) and resulting in no current being generated. Although this particular

case may not be common, it is fairly easy for an electron generated in another molecule to hit a hole left behind in a previous photoexcitation. In contrast, the injection process used in the DSSC cells does not introduce a hole in the $TiO_2$ but only an electron. Although it is energetically possible for the electron to recombine back into the dye, the rate at which this occurs is quite slow compared to the rate that the dye regains an electron from the surrounding electrolyte. Also recombination from the $TiO_2$ species in the electrolyte is possible but for optimized devices is a very slow process. On the contrary, electron transfer from the platiunm coated electrode to species in the electrolyte is very fast. As a result of this favorable kinetics, DSSCs can work also with low light, under cloudy skies and non direct sunlight.

The major disadvantage for DSSC devices is the use of a liquid electrolyte, which has temperature stability problems. At low temperatures, then electrolyte can freeze, ending power production, while at higher temperatures the liquid can expand, making sealing the panels a serious problem. Another disadvantage is that costly ruthenium (dye), platinum (catalyst) and conducting glass or plastic (contact) are needed to produce the Graetzel cell. A third major drawback is that the electrolyte solution contains volatile organic compounds (or VOC's), solvents which must be carefully sealed as they are hazardous to human health and the environment.

# Chapter 5

In this chapter we present the spectra obtained from the Brillouin measurements on $TiO_2$ samples. Here we divide the samples into two groups: in the first one we consider samples produced at the same pressure (10 Pa) and in the second one we consider samples produced at different increasing pressures (5 Pa, 7 Pa, 10 Pa and 15 Pa). The samples of the first group have been investigated through measurements performed with the same incidence angle but at different positions on the sample to evaluate the lateral uniformity.

Then we concentrate on the second group of samples which reveals to be more interesting. Here our aim is to observe the differences in the spectra obtained from samples produced at different pressure.

In this chapter we collect both the figures showing the spectra of the various samples and the tables containing the measured frequencies with relative uncertainty.

## 5.1 Measurements

This first part of the chapter contains a brief description of the technique used to produce our samples, pulse laser deposition (PLD). Then we are going to introduce the samples and their characteristics.

### 5.1.1 Samples Characteristics and Production

Samples of $TiO_2$, deposited on (001) silicon substrates, at different pressure and with different thickness, were analysed. They are listed in table 5.1, labeled by a number (i.e. TI 137 stays for $TiO_2$ 137). The letter "A" refers to the fact that also some annealed samples have been measured. Annealing is generally done with

temperatures from 400° C to 800° C, aiming at improving the structure crystallinity and at making the film more homogeneous. In our case, the samples have been annealed at 500° C for 2 hours. Samples' thicknesses have been measured during the acquisition of SEM (scanning electron microscopy) images, that will be reported in the following chapter.

| Sample name | Pressure [Pa] | Thickness [μm] |
|---|---|---|
| TI 137 | 10 | 2,172 |
| TI 137 A | 10 | ~2 |
| TI 153 | 10 | ~ 2 |
| TI 040 A | 1 | 0,5 |
| TI 041 A | 10 | 1,323 |
| TI 109 | 5 | 2,132 |
| TI 109 A | 5 | 2,113 |
| TI 110 | 7 | 2,262 |
| TI 111 | 10 | 2,312 |
| TI 112 | 15 | 2,253 |

**Table 5.1** List of the samples used in Brillouin measurements.

Our samples have been produced by the PLD systems of nanoLab-NEMAS of Politecnico di Milano and of IIT @ PoliMi (the Italian Institue of Technology) in Milan. Titanium dioxide films have been grown in a high vacuum PLD chamber made of steel and with a cylindrical shape. UV laser pulses (duration 5-7 ns) were focused on $TiO_2$ target with a pluse repetition rate of 10 Hz. The maxium energy released in every impulse is of 180 mJ. The laser beam is focused onto the target by a lens, that is necessary to improve energy fluence.

The target is mounted on a rotation-translation carousel. Combining the vertical movement and the rotation of the target, the incident spot covers uniformly the surface of the target through a spiral path. In this way, two subsequent spots do not fall on the same region avoiding the formation of craters.

Almost all the measurements have been conducted in the backscattering geometry with different incidence angles on the sample. The angles go form 20° to 70°, while the sample is orientated in order to have the incidence plane which intersects the sample surface along the (100) direction of the Si substrate. The incident plane coincides with the so-called sagittal plane.

### 5.1.2 PLD: the principle and the characteristics phenomena

This technique has been used to produce metallic films since the early 1960s with the discovery of laser. In this process a target is placed in a vacuum chamber and it is ablated by highly energetic laser pulses. The PLD scheme is shown in figure 5.1.

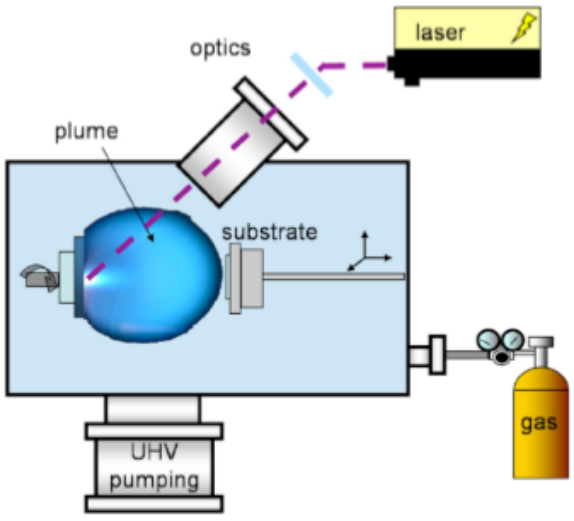


**Fig.5.1** PLD simplified scheme.

Due to the interaction between laser and target, the surface of the target melts and evaporates and, the ablated material expand towards a substrate assuming the classical shape called ablation plume. The process can occur in vacuum or in presence of an inert or reactive background gas. The principal disadvantages of this technique concern the geometry of the substrate; the deposited film is uniform only on a small area and the surface must have a simple geometry. The other disadvantage is the possible presence of particulates, sub-micrometer size droplets, on the film surface that may vary in a non-controllable way the film properties. On the contrary, PLD is widely used because it allows to study many classes of materials changing deposition parameters in large ranges.

The principal phenomena that occur in the PLD process are laser-target interaction, plasma formation and expansion and film deposition. Here we briefly describe these phases of the process.

The laser penetration depth in a material is:

$$l_A = \frac{1}{\alpha} \qquad \textbf{(5.1)}$$

where α is the material absorption coefficient that depends on the radiation wavelength. In our case, the laser used is a solid state laser [13] Nd:YAG with λ= 266 nm (ultraviolet). The interation between laser and target induces thermal and non-thermal phenomena at different time scales; in particular, the non-thermal ones, such as electron excitation, occur in the first stage of the interaction.

[13] A solid state laser is a laser which uses as a gain medium a solid and not a liquid or a gas. Generally this active medium is a glass or crystalline host material to which are added dopants such as neodymium, chromium or erbium. The most common solid state laser is the Nd:YAG (neodymium-doped yttrium aluminium garnet) that is used also in extremely high power and high energy beam systems.

The equilibrium is restored in the material through collisions between electrons and collisions between electrons and phonons. When a ns (nano second) laser is used, these phenomena occur during pulse duration, so it is possible to describe the interaction through a one temperature model.

The heat distribution depth in a material, homogeneous and isotropic, is given by

$$l_\tau = 2\sqrt{D\tau_l} \tag{5.2}$$

where D is the diffusion coefficient and $\tau_l$ is the pulse duration.

If $l_A < l_\tau$ a congruent ablation takes place and the relative concentrations of species within the plasma remains unchanged for successive laser pulses and equal to those of the target. In general, for low fluence values, material constituents are only excited, while for fluence values over the threshold value, that depends on the material, plasma formation occurs. Plume expansion in the vacuum is almost linear vs time and depends only on the velocity of the ablated particles when they escape from the target. The spatial distribution is strongly forward directed and does not change during plume expansion. The presence in the chamber of an inert gas at a given pressure affects the plume expansion and modifies important process features such as spatial distribution, deposition rate and kinetic energy distribution of deposited particles. Chemically reactive gases such as $O_2$, $N_2$, $H_2$ are used to deposite oxides, nitrides and hydrides starting from a metallic or dieletric target. Film growth mechanism can be divided into two classes: atom by atom or cluster assembling, depending on collisional phenomena that take place during plume expansion. Atom by atom growth mechanism is the analogous to those occurring in other deposition techniques, such as chemical vapor deposition (CVD). In this regime, film growth happens with three mechanisms: 3-D island growth, layer by layer growth and mixed growth. The first one produces rough films and occurs when the cohesion between atoms is larger than that between atoms and the substrate. The second

mechanism produces more compact films and the cohesion between atoms and the substrate is dominant. In practice, we have the growth of bidimensional layers that grow one-by-one. In the mixed formation mechanism, the properties of the film obtained are at halfway between those of the two mechanism introduced above. Cluster aggregation in the plume occurs at sufficiently high gas pressure. In this case film formation is determined by the kinetic energy per atom in the cluster and it is possible to deposit films with different morphologies, from compact to highly porous. If the kinetic energy per atom in the cluster is not high enough to fragment the clusters, the film grows by the second mechanism: cluster assembling. Other important parameters are laser pulse characteristics and substrate temperature. Short wavelength pulses deposit larger energy density per volume in the target. High values of fluence induce high ionization degree and energy of the ablated species. Generally depositions are conducted using a fluence slightly greater than the threshold for ablation. Increasing the spot size the plume has better directionality, normal to the target and the expulsion of particulate fragments is reduced. The incident angle is usually 45°, because it is a good compromise between spot size and plasma shielding process. Substrate temperature influences growth mechanism, because a high temperature can favor the diffusion of the species on the substrate and can lead to crystalline films. However, an excessive temperature can cause the re-evaporation of the film and of the more volatile elements: temperature is a good way to select the deposited compounds. Many works indicate that substrate temperature influences also the crystalline grain sizes: in general higher temperatures bring to formation of bigger crystalline grains. The deposition parameters, such as laser fluence or substrate temperature, can influence also the rutile/anatase ratio; in fact, since rutile is typically formed at higher temperature (400°C) than anatase (300°C), raising the substrate temperature favors rutile growth. An increase in the background pressure leads in many cases to preferential growth of anatase, because kinetic energy of the particles impinging on the substrate is reduced. In our case, $TiO_2$ is produced in the rutile phase with increasing percentage of anatase at pressure increase.

### 5.1.3 Characteristics and Parameters of Brillouin Spectroscopy Measurements

This thesis is based on a measurement campaign on two batches samples of $TiO_2$ produced by PLD. The experimental results have been obtained by a Brillouin spectrometer, that works with a laser $Ar^+$ ion laser (Coherent Innova 304) with these characteristics:

- Maximum power 4 W
- Maximum power of 1,4 W at $\lambda = 514$ nm
- Maximum power of 0,8 W at $\lambda = 488$ nm
- Laser beam diameter of 3,9 mm

We used the laser at a $\lambda_0$=514 nm and at a power of 100-150 mW. These measurement have been conducted with the aim of analysing the obtained spectra to gain information about some properties of $TiO_2$ films, such as elastic constants and dispersion relations.

Spectra are collected as counts vs channel number. In agreement with the finesse of the interferometer, of about 100 (see chapter 3), data collection is performed over 512 channels. Spectra are then analysed and converted in terms of count number vs frequency (or velocity) by a MATLAB tool named Brillo, developed at Nanolab, Dept. of Energy.

In general, the data collection time depends on the signal to noise ratio: low values of this ratio, or low peak intensities, need long acquisition times to improve the signal to noise ratio. In our case, the data collection times range from about 20 minutes (that correspond to 2000 counts) to almost 4 hours (about 20000 counts).

**Fig.5.2** Experimental apparatus for Brillouin spectroscopy of NanoLab at Politecnico di Milano.

**Fig.5.3** Sample holder of the Brillouin apparatus.

## 5.2 Brillouin Spectra of $TiO_2$ films : first batch of samples

The first phase of our measurements was concentrated on few samples, listed in the table below:

| Sample name | Pressure [Pa] | Thickness [μm] |
|---|---|---|
| TI 137 | 10 | 2,172 |
| TI 137 A | 10 | ~2 |
| TI 153 | 10 | ~2 |
| TI 040 A | 1 | 0,5 |
| TI 041 A | 10 | 2,323 |

**Table 5.2** First group of analysed samples.

Figure 5.4 present an example of the analysed samples, in particular $TiO_2$ 137, where we can note the presence of interference fringes.

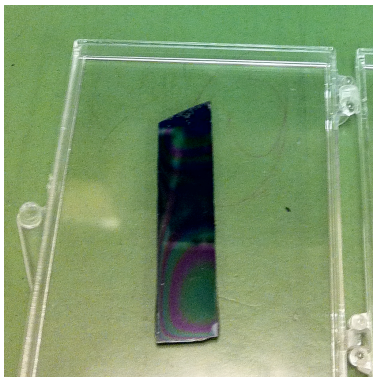

**Fig.5.4** One of the measured samples, $TiO_2$ 137.

This paragraph presents the spectra of $TiO_2$ in terms of count number vs frequency. It is possible to convert these spectra in count number vs velocity for waves with wavevector parallel to the surface, knowing that in this case the frequency and velocity are linked by the following relation :

$$v = f\frac{2\pi}{k_{\parallel}} = f\frac{2\pi}{k_0 \sin\theta} = f\frac{\lambda_0}{\sin\theta}$$

where $f$ is the peak frequency, $k_{\parallel}$ is the wavevector parallel to the surface, $\theta$ is the incidence angle and $\lambda_0$ is the laser wavelength. This conversion is done by the MATLAB tool already mentioned.

### 5.2.1 Spectra of $TiO_2$ 137 before annealing

This paragraph presents some spectra of $TiO_2$ 137 (10 Pa), not annealed, taken at different angles and in different position on the samples. Positions are selected looking for points from which elastic scattering is weaker, and points in regions where film thickness is more uniform, as it can be estimated by interference fringes. We supposed that in these points the sample should have a more uniform structure. An example is sketched in Figure 5.5.

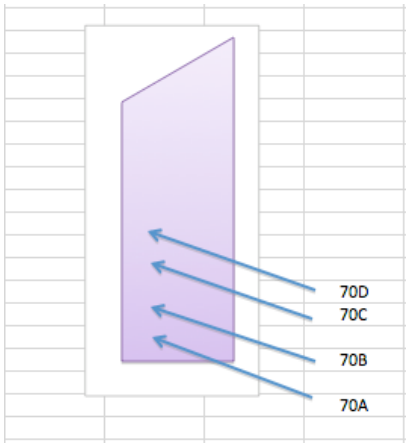


**Fig.5.5** Sketch of a the sample $TiO_2$ 137 with the points of measure marked out with arrows.

The first spectra were obtained with a backscatterimng geometry and with a mirror spacing of 2 mm. This means a relatively wide FSR of about 75 GHz.

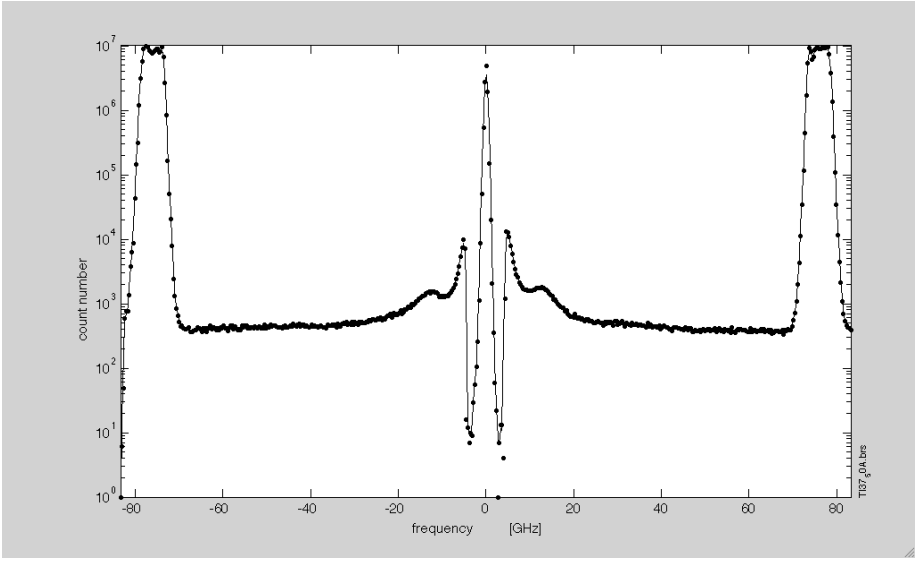


**Fig.5.6** $TiO_2$ 137 with θ=50° and with mirror spacing d= 2 mm.

In this spectrum a broad peak is visible between 10 and 20 GHz, without any spectral feature at higher frequencies. Consequently, and in order to improve the resolution of this lower frequency part of the spectrum, subsequent measurements were performed with a mirror spacing of 4 mm, meaning a FSR of about 37,5 GHz.

With this mirror spacing and the same incidence angle spectra have been measured at different positions on the sample. Figure 5.7 collects these spectra.

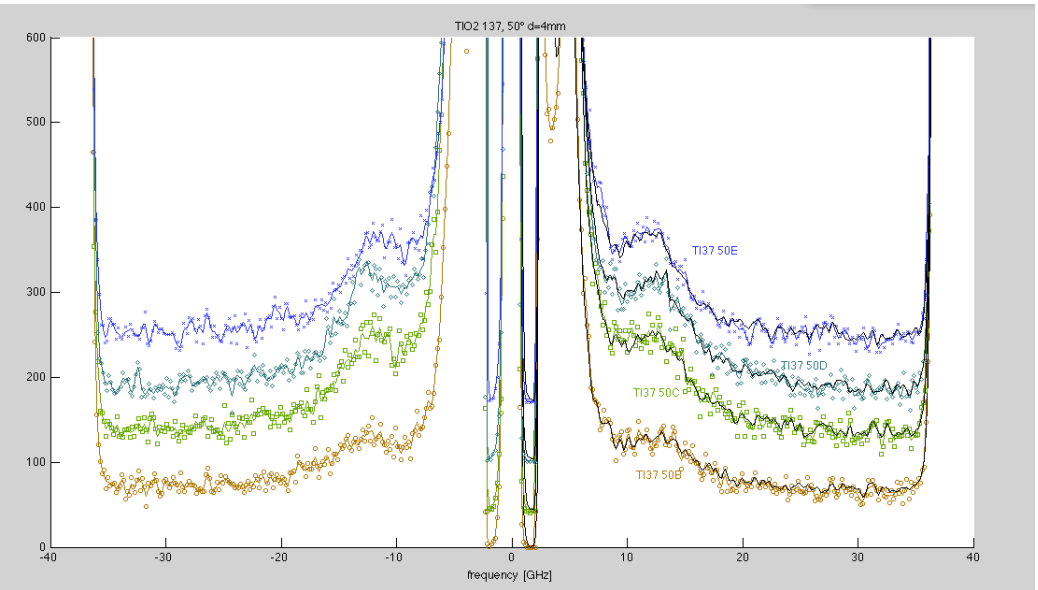


**Fig.5.7** $TiO_2$ 137, θ=50° and d= 4mm. Spectra taken at different positions on the sample.

In this figure, the peak at about 12 GHz has become more visible. It has almost the shape of a shoulder and remains essentially unchanged in the various positions on the sample. There is also another peak at about 5 GHz which is much more intense than that at 12 GHZ, as shown in Fig. 5.8, in logarithmic scale; it also is essentially independent from the measurement position.

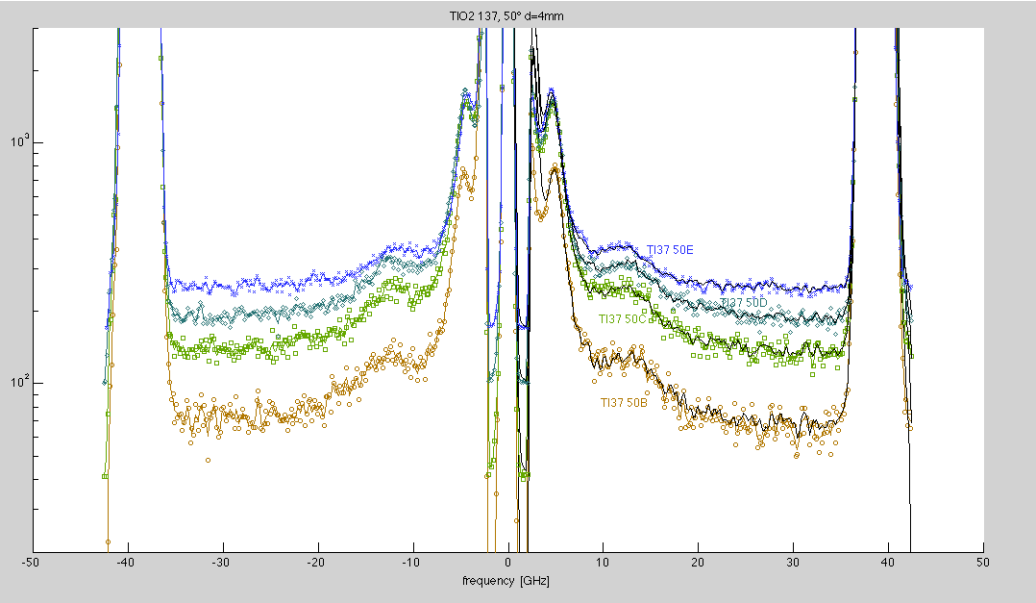


**Fig.5.8** $TiO_2$ 137, θ=50° and d= 4mm. Spectra taken at different positions on the sample.

The frequencies of the peaks have been measured fitting the peaks by the already mentioned MATLAB tool. All the peaks have been fitted with gaussians, with the so called "sum of doublets" option, which also fits the background. The following tables summarize the results.

| File name | Frequency [GHz] | Uncertainty [GHz] | Frequency [GHz] | Uncertainty [GHz] |
|---|---|---|---|---|
| TI37_50B | 4,92 | 1,01 | 12,32 | 0,57 |
| TI37_50C | 4,24 | 0,048 | 11,88 | 0,97 |
| TI37_50D | 4,28 | 0,038 | 12,88 | 0,18 |
| TI37_50E | 4,60 | 0,051 | 11,03 | 0,34 |

**Table 5.3** Frequencies of $TiO_2$ 137 first peak and second peak of the spectra obtained with Brillo, with $\theta$=50°.

In order to assess the possible dependence of these peak frequencies on the incidence angle, the same measurements have been conducted with an incidence angle of 60°. Figure 5.9 shows these spectra, obtained at different points on the sample.

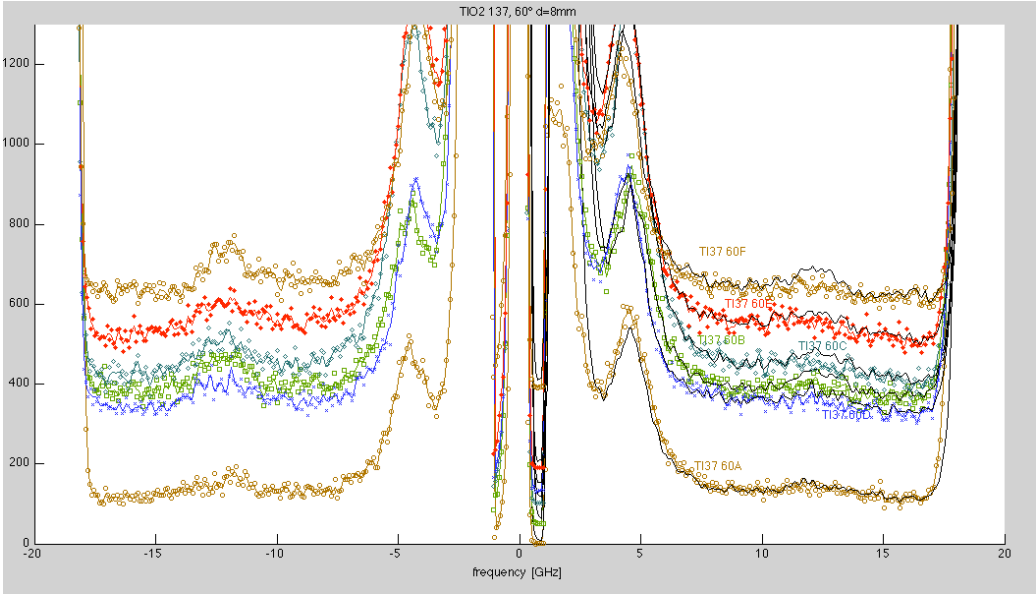


**Fig.5.9** $TiO_2$ 137, θ=60° and d= 8mm. Spectra taken at different positions on the sample.

Table 5.4 shows the frequencies of the spectral doublets, obtained by the same fitting procedure mentioned above:

| File name | Frequency [GHz] | Uncertainty [GHz] | Frequency [GHz] | Uncertainty [GHz] |
|---|---|---|---|---|
| TI37_60A | 4,66 | 0,038 | 11,87 | 0,26 |
| TI37_60B | 3,93 | 0,107 | 11,86 | 0,47 |
| TI37_60C | 4,56 | 0,045 | 12,21 | 0,41 |
| TI37_60D | 4,24 | 0,081 | 11,65 | 0,28 |
| TI37_60E | 3,95 | 0,046 | 11,02 | 0,31 |
| TI37_60F | 4,24 | 0,036 | 11,73 | 0,18 |

**Table 5.4** Frequencies of $TiO_2$ 137 first and second peak of the spectra obtained with Brillo, with θ=60°.

The comparison of Figures 5.7 and 5.9 shows the strong similarity of the spectra obtained at the two incidence angles, with the peak at about 5 GHz which seems to be more intense at θ=60° than at θ=50°. Also the comparison of Tables 5.3 and 5.4 shows that the spectral frequencies do not change with the incidence angle.

Further spectra, shown in Figure 5.10, were measured with θ=70°; the obtained frequencies are presented in Table 5.5.

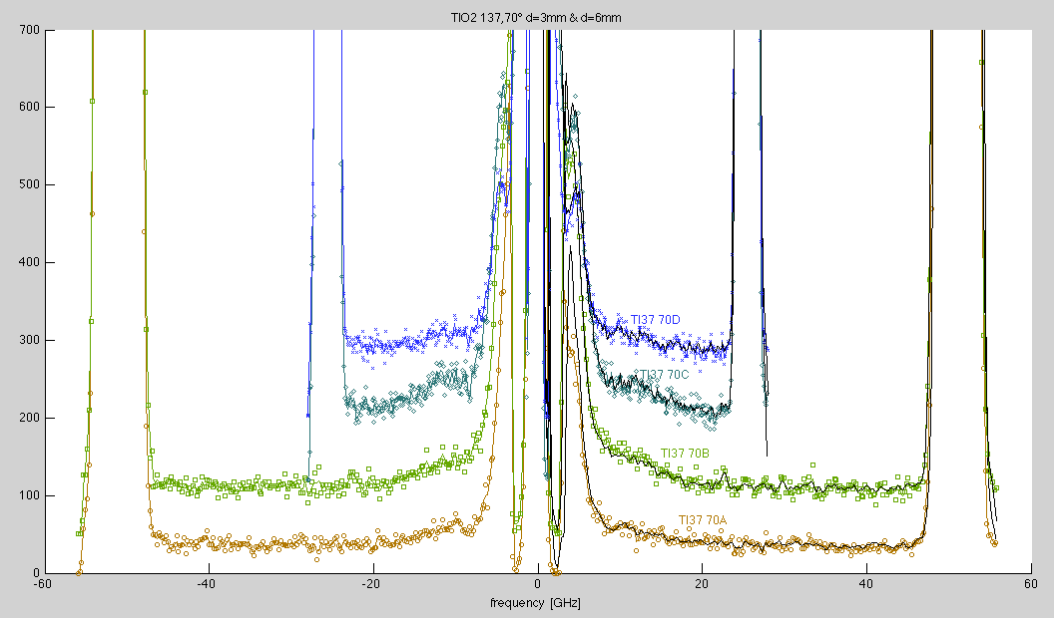


**Fig.5.10** $TiO_2$ 137, θ=70°. The two spectra at the bottom are collected with d=3 mm while the two spectra at the top with d=6 mm.

| File name | Frequency [GHz] | Uncertainty [GHz] | Frequency [GHz] | Uncertainty [GHz] |
|---|---|---|---|---|
| TI37_70A | / | / | 10,01 | 0,31 |
| TI37_70B | / | / | 11,45 | 0,93 |
| TI37_70C | 4,79 | 0,07 | ~11,8 | ~0,50 |
| TI37_70D | 5,02 | 0,12 | ~10 | ~0,75 |

**Table 5.5** Frequencies of $TiO_2$ 137 first and second peak of the spectra obtained with Brillo, with $\theta$=70°. TI37_70A and TI37_70B have been obtained with d=3 mm and the only peak that can be fitted is the one at about 11 GHz.

In conclusion, sample $TiO_2$ 137 (10 Pa) presents two peaks, one at about 4 GHz and the other one at about 11 GHz. To a first approximation, the frequencies of these peaks do not depend on the point of measure on the sample, so that we can consider our sample sufficiently uniform form the point of view of wave propagation. A measurement has been done also with another scattering geometry, the forward scattering (90° scattering) instead of backscattering, but the spectra we have obtained are not really significant.

The following figure contains the spectra obtained on $TiO_2$ 137 at different incidence angles.

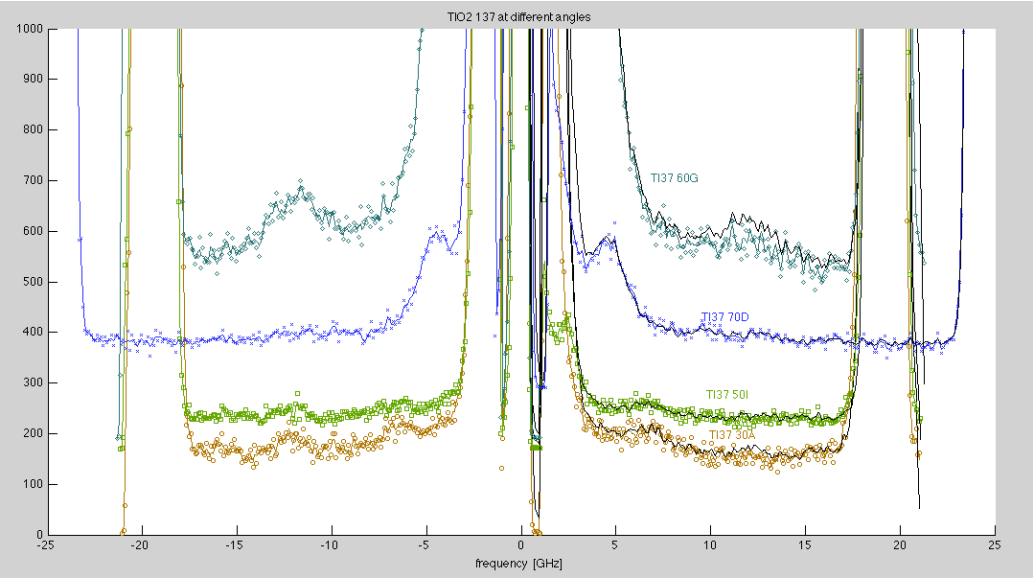


**Fig.5.11** $TiO_2$ 137: spectra at different θ, from 30° to 70° and with d=6,8 mm.

### 5.2.2 Spectra of $TiO_2$ 137 after annealing

This paragraph contains some spectra of the sample $TiO_2$ 137 after its annealing at 500°C for 2 hours. Our aim is to verify if the thermal process, made to improve cristallinity, restores the material with a more compact and uniform structure. Figure 5.12 shows the spectra obtained on the annealed sample with θ=60°.

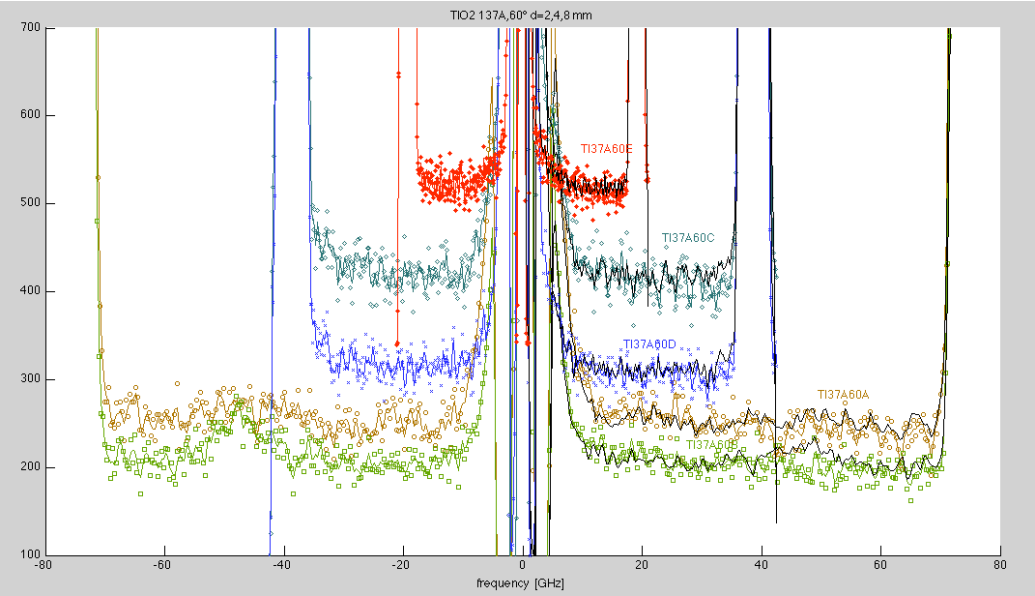


**Fig.5.12** $TiO_2$ 137 A, θ=60°. The spectrum at the top of the figure are collected with d=8 mm, the two in the middle with d=4 mm while the two at the bottom with d=2 mm.

In this case, neither of the spectra contains measurable spectral doublets. There are no feature which emerges from the background noise. The reason for this disappearance of the spectral peaks upon annealing is not clear.

### 5.2.3 Spectra of $TiO_2$ 153 before annealing

$TiO_2$ 153 is a sample whose pressure of deposition is the same of $TiO_2$ 137, 10 Pa. The measurements on this sample have been conducted to compare the spectra with equal parameters of production but produced in different times.

Figure 5.13 and table 5.6 collect the spectra at θ=60° and the measured frequencies, respectively.

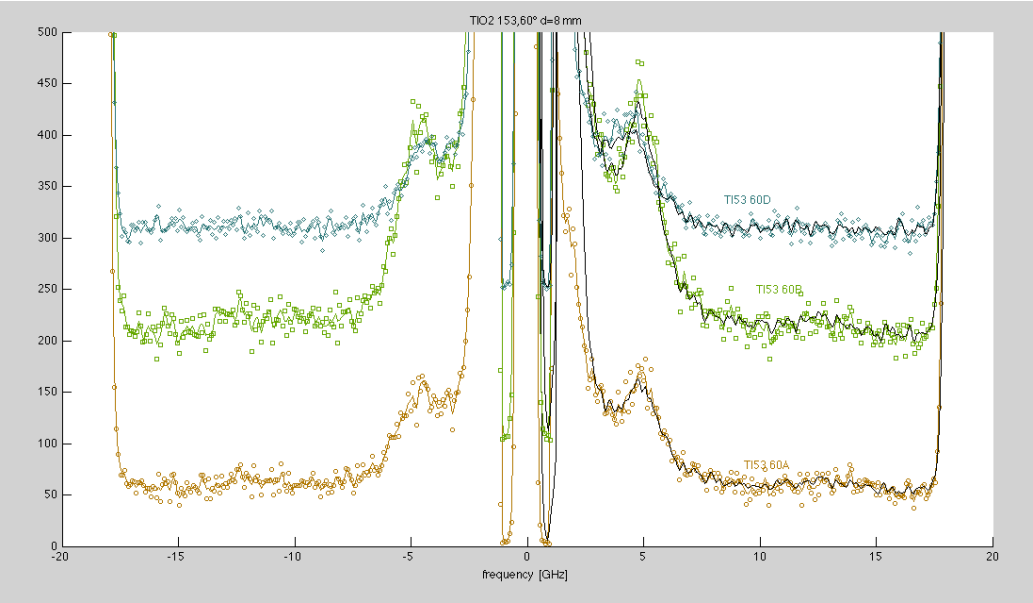


**Fig.5.13** $TiO_2$ 153, θ=60° and d=8 mm.

The spectra are similar to those of Fig. 5.9, although the feature at around 12 GHz is weaker, and did not allow a reliable identification of its frequency by the fitting procedure. The frequencies of the peak at around 5 GHz are not appreciably different from those of Table 5.4. It can be concluded that the two peaks observed for the $TiO_2$ 137 sample are associated to the acoustic waves peculiar of the samples produced at 10 Pa.

| File name | Angle | Frequency [GHz] | Uncertainty [GHz] |
|---|---|---|---|
| TI53_60A | 60° | 4,99 | 0,061 |
| TI53_60B | 60° | 4,71 | 0,11 |
| TI53_60D | 60° | 4,11 | 0,12 |

**Table 5.6** Frequencies of $TiO_2$ 153 first peak of the spectra obtained with Brillo, with $\theta$=60°.

### 5.2.4 Spectra of $TiO_2$ 040 and 041 after annealing

This paragraph takes in consideration some spectra obtained from Brillouin measurements on two samples, $TiO_2$ 040 and $TiO_2$ 041, produced at 1 Pa and 10 Pa, respectively.

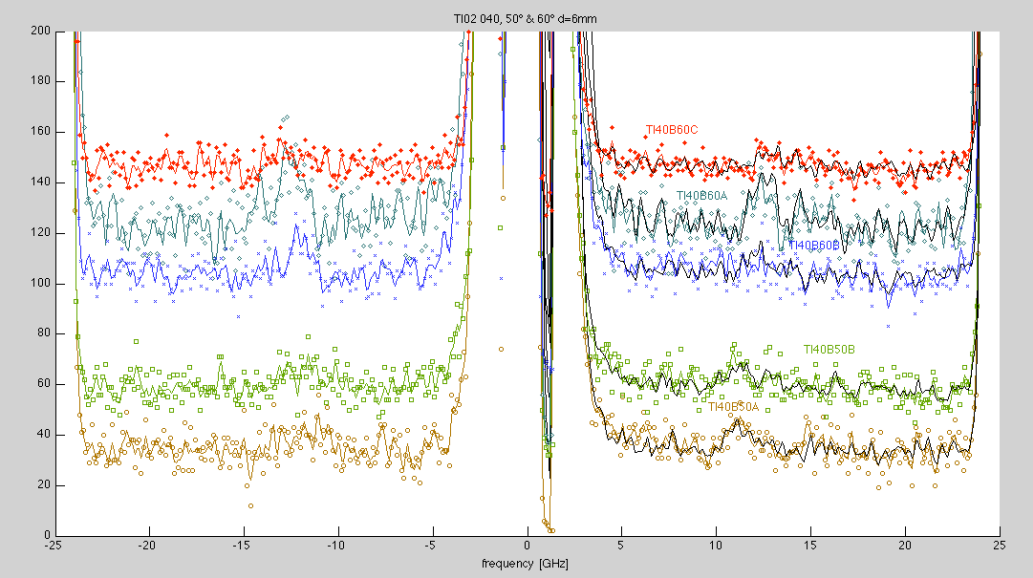


**Fig.5.14** $TiO_2$ 040, θ=50° and 60° and d=6 mm. This sample has been annealed at 500 °C for 2 hours.

The sample before annealing was not available so we cannot make a comparison between the two situations, before and after annealing. Also in these samples, there seems to be a weak peak at about 10-11 GHz. In this case its frequency tends to increase when the incidence angle increases.

The sample $TiO_2$ 041, produced at the same pressure of $TiO_2$ 137 and also annealed at 500 °C for 2 hours, offers the possibility of checking the results obtained on $TiO_2$ 137 after annealing. The results can be considered similar, but only because the spectra obtained from $TiO_2$ 041, like those obtained from Ti

137 after annealing, do not contain any reliably measurable peak. Again, the origin of this disappearance of peaks upon annealing is not clear.

## 5.3 Brillouin Spectra of $TiO_2$ films : second batch of samples

This section collects the measurements performed on the second group of samples, that have been produced in IIT laboratory. The following table shows the principal characteristics of these samples :

| Sample name | Pressure [Pa] | Thickness [μm] |
|---|---|---|
| TI 109 | 5 | 2,132 |
| TI 109 A | 5 | 2,113 |
| TI 110 | 7 | 2,262 |
| TI 111 | 10 | 2,312 |
| TI 112 | 15 | 2,253 |

**Table 5.7** Second group of analysed samples.

### 5.3.1 Spectra of $TiO_2$ 111 before annealing

Among the samples of this second group, $TiO_2$ 111, produced at the same pressure of $TiO_2$ 137 (10 Pa), was considered first. Figure 5.15 shows the spectra obtained from Brillouin measurements in backscattering geometry and with incidence angles from 20° to 70°. The spectra have been analysed, and the peaks fitted, by the same MATLAB tool 'Brillo' mentioned previously.

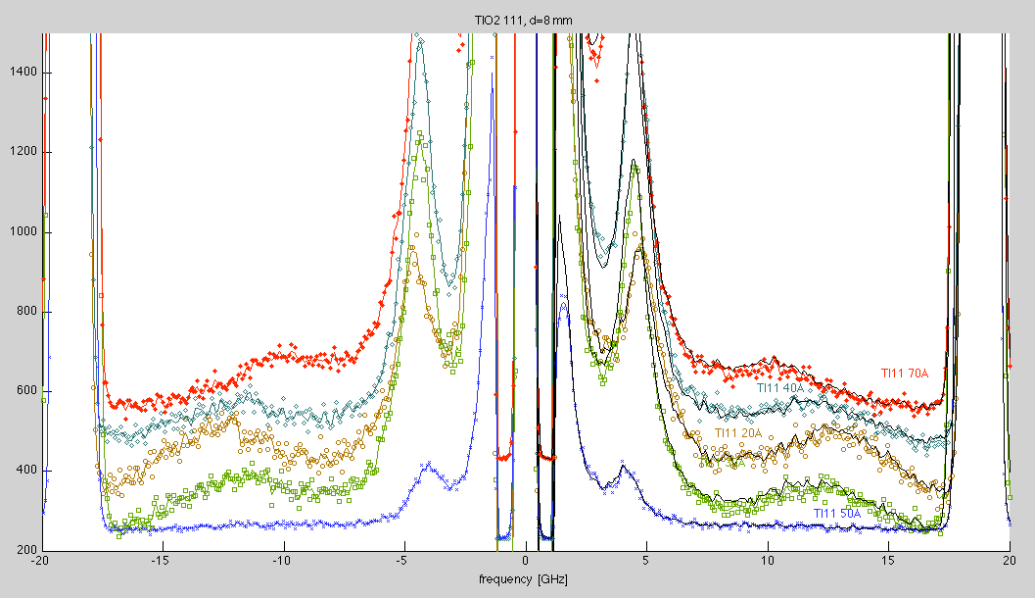


**Fig. 5.15** $TiO_2$ 111, θ= 20°÷70°and d=8 mm.

We can see that the two peaks found for Ti 137 (at about 4 GHz and at about 11 GHz) are still present, and even better defined. This confirms the reproducibility of results from samples produced at the same pressure. In the next chapter, we are going to show some SEM images of these samples to gain information about their morphological structure. Due to the similarity of the vibrational spectra, we expect similar structure and morphology. Table 5.8 presents the frequency shifts of the two peaks obtained by the fitting procedure.

| File name | Frequency [GHz] | Uncertainty [GHz] | Frequency [GHz] | Uncertainty [GHz] |
|---|---|---|---|---|
| TI11_20A | 4,71 | 0,48 | 12,46 | 0,41 |
| TI11_30A | 4,38 | 0,054 | 11,70 | 0,55 |
| TI11_40A | 4,51 | 0,057 | 11,68 | 0,61 |
| TI11_50A | 4,26 | 0,034 | 11,98 | 0,19 |
| TI11_70A | 3,66 | 0,053 | 10,44 | 0,20 |

**Table 5.8** Fitted frequencies of the first and the second peak of $TiO_2$ 111 spectra, with d=8 mm and θ from 20° to 70°.

The values of Table 5.8, and Figure 5.16, which replicates Fig. 5.15 but with a logarithmic scale, suggest a trend of the peaks' frequencies with the angles. This will be analysed in detail in the next chapter.

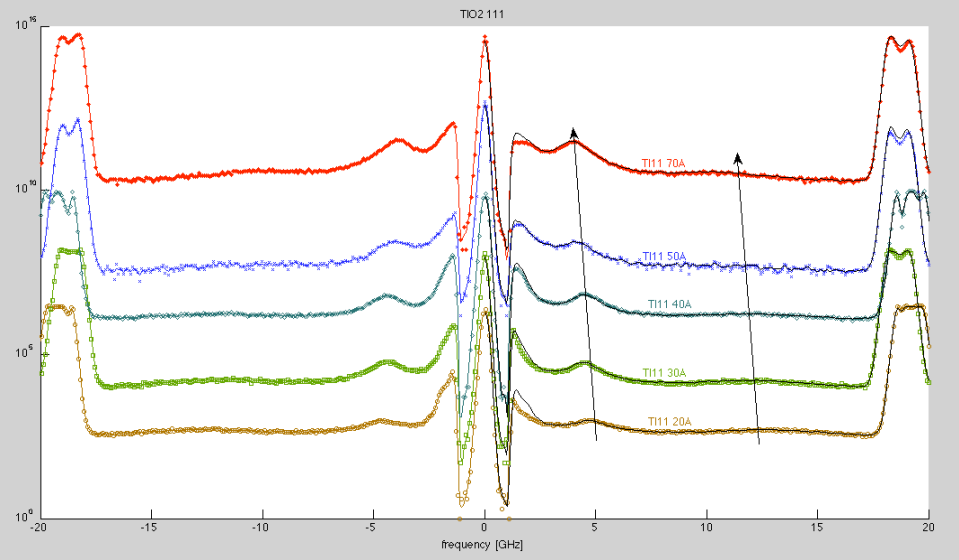


**Fig. 5.16** $TiO_2$ 111, with d=8 mm and θ= 20°÷70°. The black arrow helps to give an idea of the variation of the peak's position with θ.

### 5.3.2 Spectra of $TiO_2$ 110 before annealing

This sample, produced at 7 Pa, has been measured in the same conditions of $TiO_2$ 111, at different angles, θ=20°÷70°, and with a mirror spacing of 8 mm. In this sample, a well delimited zone was very clearly observable: this is a zone between interference fringes where the thickness and the structure should be very unifrom. Therefore, we decided to carry on our measurements in this zone, at about the sample center, as it shown in the sketch of figure 5.17:


**Fig.5.17** Sketch of the sample $TiO_2$ 110 where the arrows indicate the points of measure in the "saddle " between interference fringes.

In figure 5.18 we show the spectra obtained form Brillouin measurements on this sample.

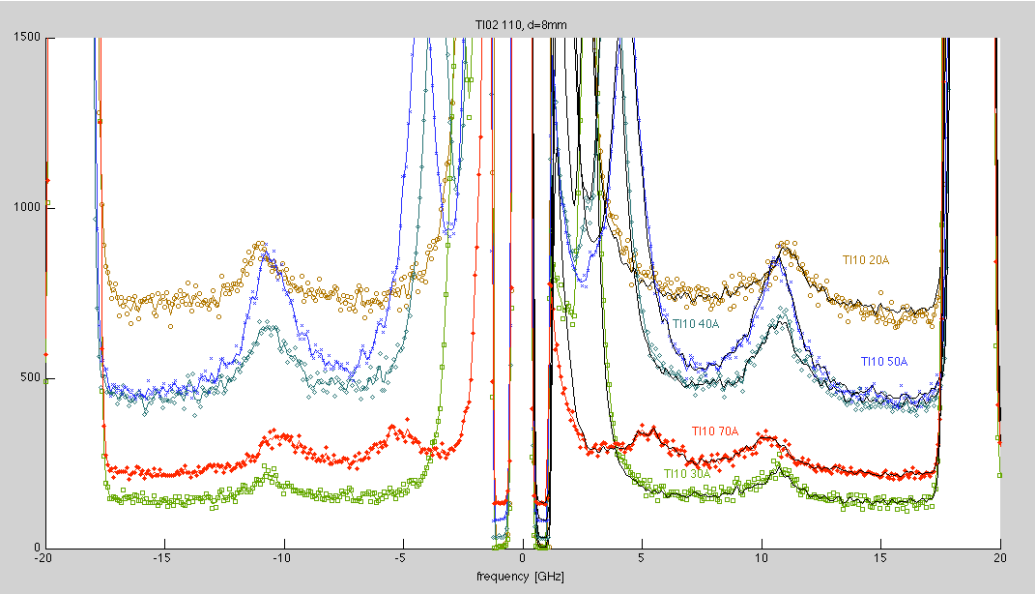


**Fig.5.18** $TiO_2$ 110, θ= 20°÷70° and d=8 mm.

Also in these spectra, the two peaks that we have seen in almost all the spectra discussed up to now are still visible. However, in this case the dependence of their frequencies on the incidence angles is different and more marked. This can be seen in Table 5.10, which presents the frequencies obtained from the fitting process, and in Fig. 5.18. This dependence will be analyzed in the next chapter. In particular, although $TiO_2$ 111 and $TiO_2$ 110 were produced at only slightly different pressures (10 Pa and 7 Pa respectively), the trends of frequency vs angle are almost opposed.

| File name | Frequency [GHz] | Uncertainty [GHz] | Frequency [GHz] | Uncertainty [GHz] |
|---|---|---|---|---|
| TI10_20A | / | / | 11,00 | 0,81 |
| TI10_30A | 2,78 | 0,091 | 10,67 | 0,22 |
| TI10_40A | 3,57 | 0,038 | 10,73 | 0,056 |
| TI10_50A | 4,29 | 0,98 | 10,61 | 0,030 |
| TI10_70A | 5,05 | 0,45 | 10,19 | 0,081 |

**Table 5.9** Fitted frequencies of the first and the second peak of $TiO_2$ 110 spectra, with d=8 mm and θ from 20° to 70°. In the spectrum (TI10_20A) the peak at about 4 GHz is not clearly visible.

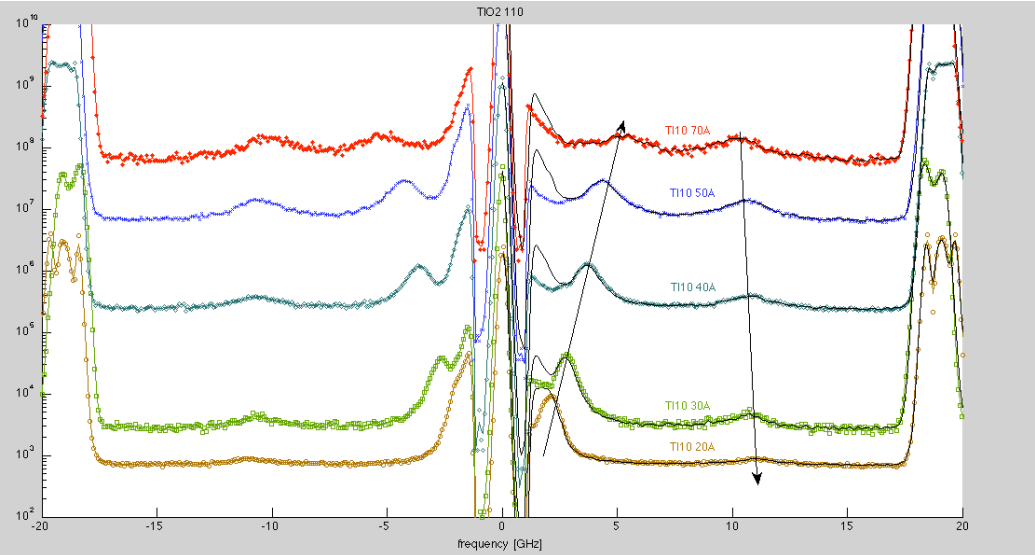


**Fig.5.19** $TiO_2$ 110, with d=8 mm and θ= 20°÷70°. The black arrows help to individuate if the trend is increasing or decreasing.

### 5.3.3 Spectra of $TiO_2$ 109 before annealing

As noted above, the two samples $TiO_2$ 111 (10 Pa) and $TiO_2$ 110 (7 Pa) show almost opposite trends of peak frequency vs angle. The sample $TiO_2$ 109, produced at 5 Pa, offers the possibility of further investigating this dependence.

First of all, we show a spectrum obtained with a very large FSR, with a mirror spacing of 0,8 mm. This allows to probe very high frequencies until 180 GHz. This allowed to observe the peak due to the longitudinal bulk mode of the Si substrate, at about 145 GHz that confirms the transparency of the film. Figure 5.20 shows the spectrum obtained by this measurement:

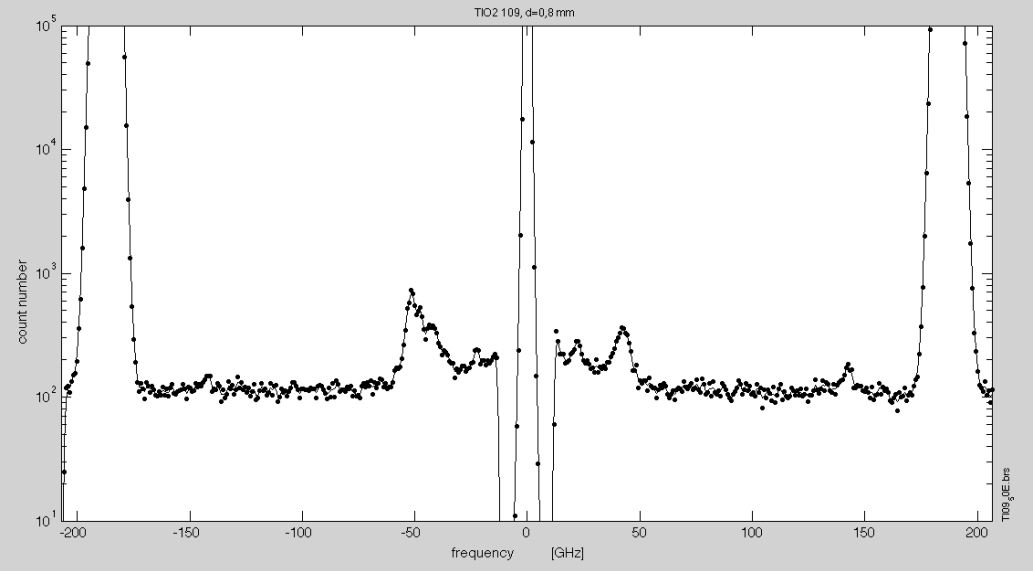


**Fig.5.20** $TiO_2$ 109 with d=0,8 mm and θ=50°. The peak at about 145 GHz of Si substrate is visible.

The peak at about 145 GHz that was fitted and gave a frequency shift of 142,36 GHz. Other peaks can be seen in this spectra; figure 5.21 shows these peaks expanded. Beside the doublets at around 20 GHz and 40 GHz, an asymmetric

peak at -50 GHz is clarly visible. As suggested by its complete asymmetry, this peak is a spurious instrumental artefact, which is known to be found with this specific spectrometer, and always at -50 GHz, when the intensity of the elastically scattered light is high. Since the peak at about 40 GHz is very close to this spurious peak (the two partially overlap), finding its frequency by the fit procedure was quite delicate. The results are shown in Table 5.10.

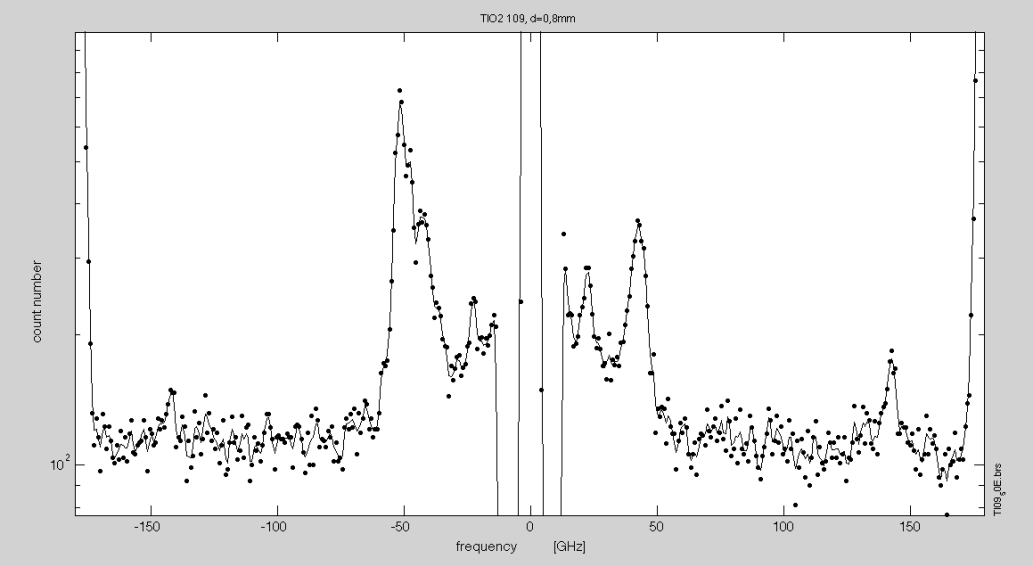


**Fig.5.21** $TiO_2$ 109, with d=0,8 mm. Zoom on the peaks.

| File name | Frequency [GHz] | Uncertainty [GHz] | Frequency [GHz] | Uncertainty [GHz] |
|---|---|---|---|---|
| TI09_50E | 22,51 | 1,79 | 42,49 | 1,92 |

**Table 5.10** Fitted frequencies of $TiO_2$ 109 first and second peak with d=0,8 mm.

In addition we show in the following figure the spectra obtained as in the previous cases, with θ ranging from 20° to 70°. In this case the FSR is larger to see if there are peaks of higher frequencies such as those seen in $TiO_2$ 109 spectra with d=0,8.

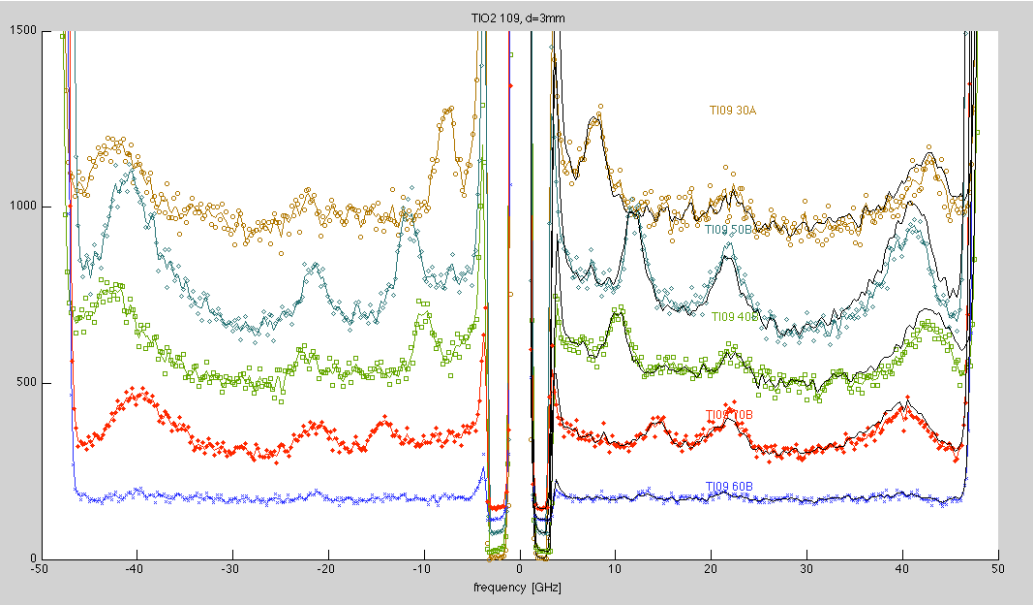


**Fig.5.22** $TiO_2$ 109, with d=3 mm and θ=30°÷70°.

Figure 5.22 shows three distinct peaks that are clearly visible. It must be noted that these peaks seem to have a non conventional shape, especially the third one (the one at about 40 GHz) which has an asymmetric shape. Anyway, in table 5.11 we present all the frequencies measured with Brillo of the three identified peaks. It is interesting to note that two peaks appear in the spectra, which were not present in the spectra discussed up to now.

| File name | Frequency [GHz] | Uncertainty [GHz] | Frequency [GHz] | Uncertainty [GHz] |
|---|---|---|---|---|
| TI09_30A | 7,95 | 0,38 | 26,45 | 1,42 |
| TI09_40B | 10,15 | 0,39 | 21,63 | 0,52 |
| TI09_50B | 11,78 | 0,30 | 21,82 | 0,39 |
| TI09_60B | 13,08 | 0,58 | 21,32 | 0,43 |
| TI09_70B | 14,31 | 0,53 | 21,69 | 0,50 |
| TI09_30A | 42,36 | 0,46 | | |
| TI09_40B | 41,21 | 0,24 | | |
| TI09_50B | 40,91 | 0,25 | | |
| TI09_60B | 40,01 | 1,49 | | |
| TI09_70B | 39,81 | 0,26 | | |

**Table 5.11** Fitted frequencies of $TiO_2$ 109 first, second and third peak with d=3 mm.

A clearer view of the trends of measured frequencies with the angle θ is given in figure 5.23, where, as we have done for the other spectra, the Y axis is logarithmic. Also this dependence will be analysed in the next chapter.

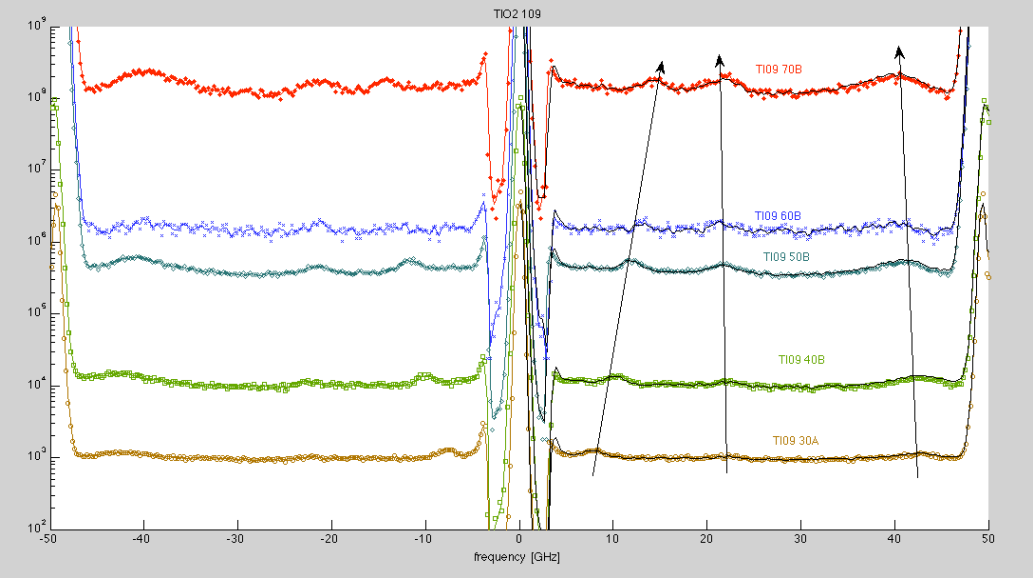


**Fig.5.23** $TiO_2$ 109, with d=3 mm and θ= 30°÷70°. The black arrows help to display if the trend is increasing or decreasing.

### 5.3.4 Spectra of $TiO_2$ 109 after annealing

Among the sample the second group, only $TiO_2$ 109 (5 Pa) presents the peaks at about 20 GHz and about 40 GHz. Since this is the sample produced at the lower pressure, and therefore more compact, we decided to perform measurements also on the same sample after annealing. Since annealing is expected to increase the compactness, it could be expected that the two peaks, observable only in the more compact film, would become even more marked.

Here we present the two measurements conducted on $TiO_2$ 109 A, with d=0,8 mm, to also explore the high frequencies, and with θ=50° and θ=65°. Figure 5.24 collects these two spectra:

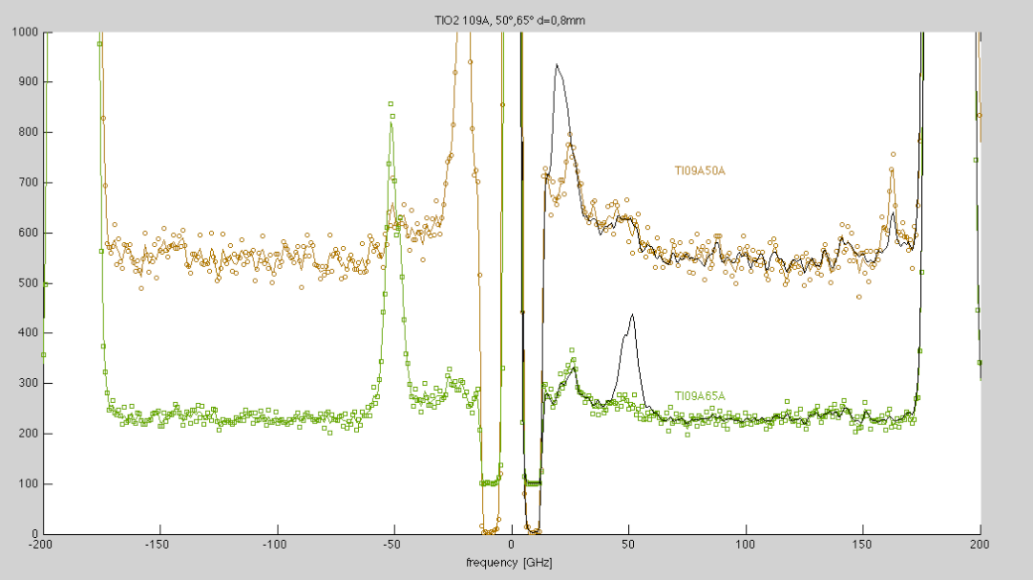


**Fig.5.24** $TiO_2$ 109 A, with d=0,8 mm and θ=50°, 65°.

Also in this case the spurious asymmetric peak at -50 GHz, due to strong elastic scattering, is clearly visible, and makes the fitting procedure difficult. However, we can see a symmetric peak at about 50 GHz and one at about 25 GHz. Interestingly, the peak at about 11 GHz, which we have clearly seen in $TiO_2$ 109 spectra, seems to disappear. Also in this case, with a wide FSR, we can see the peak at about 145 GHz due to the bulk longitudinal mode of the Si substrate.

### 5.3.5 Spectra of $TiO_2$ 112 before annealing

This paragraph presents the spectra obtained from Brillouin measurements on $TiO_2$ 112, which is the sample produced at the highest pressure, 15 Pa.

In figure 5.25 we collect the spectra obtained in the usual backscattering configuration with d=8 mm and θ ranging from 30° to 70°.

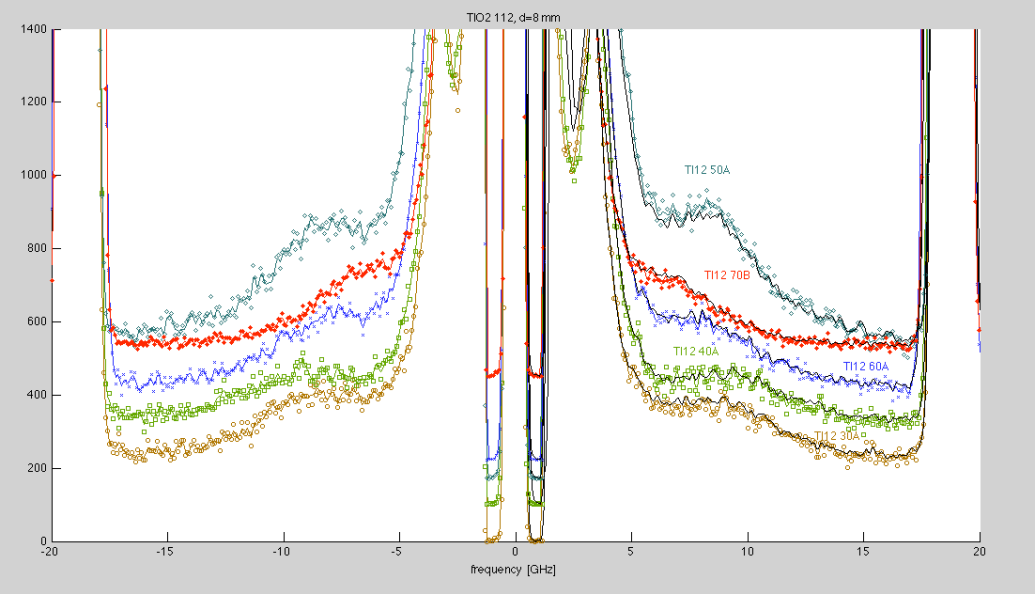


**Fig.5.25** $TiO_2$ 112, with d=8 mm and θ=30°÷70°.

Also in this case we found the two peaks observed in the previous paragraphs: the second one has a broader shape. Figure 5.26 shows the trends of the frequencies of the peaks with the angle θ while table 5.12 lists the fitted frequencies.

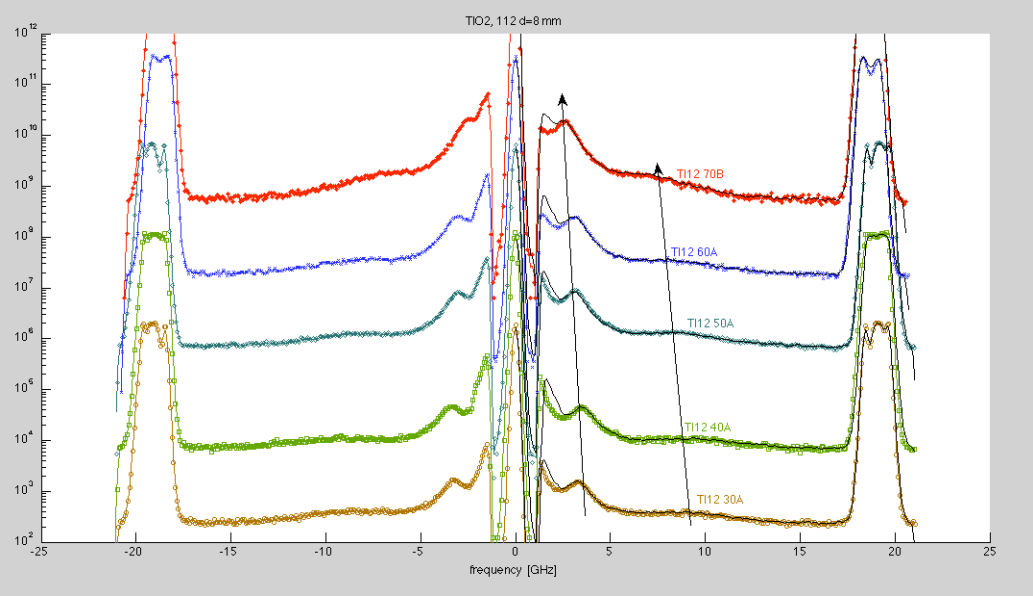


**Fig.5.26** $TiO_2$ 112, with d=8 mm and θ=30°÷70°. The Y axis in in logarithmic scale and the arrows are heplful to figure out the trends.

| File name | Frequency [GHz] | Uncertainty [GHz] | Frequency [GHz] | Uncertainty [GHz] |
|---|---|---|---|---|
| TI12_30A | 3,53 | 0,091 | 9,01 | 0,30 |
| TI12_40A | 3,49 | 0,26 | 9,72 | 0,48 |
| TI12_60A | 3,17 | 0,25 | 7,93 | 0,21 |
| TI12_50A | 3,20 | 0,44 | 7,67 | 0,79 |
| TI12_70B | ~3 | ~0,75 | 6,03 | 0,58 |

**Table 5.12** Fitted frequencies of $TiO_2$ 112 first and second peak with d=8 mm. TI12_70B has a peak of very low intensity and with a shape difficult to fit with a gaussian. We have inserted in the table an approximative value taken on the spectrum "more or less".

### 5.3.6 Analysis of the Spectra of all the Samples of $TiO_2$ at Different Angles

In this section we compare some spectra of all the samples of the second group taken at different angles. The following figures show the spectra of $TiO_2$ 109 (5 Pa), 110 (7 Pa), 111 (10 Pa) and 112 (15 Pa), each one at an incidence angle θ that goes from 30° to 70°. Here we are going to show only the part of the spectra which is in common between all the samples, cutting the peaks of $TiO_2$ 109 at higher frequencies. We have already shown the spectra of $TiO_2$ 109 with all the three observed peaks in the previous paragraph.

This analysis was taken in consideration to observe if there are evident differences between peaks frequencies of the samples probed at the same incidence angle. For example, here we show figure 5.27, that collects the spectra of $TiO_2$ 109, 110, 111 and 112 at θ=30° :

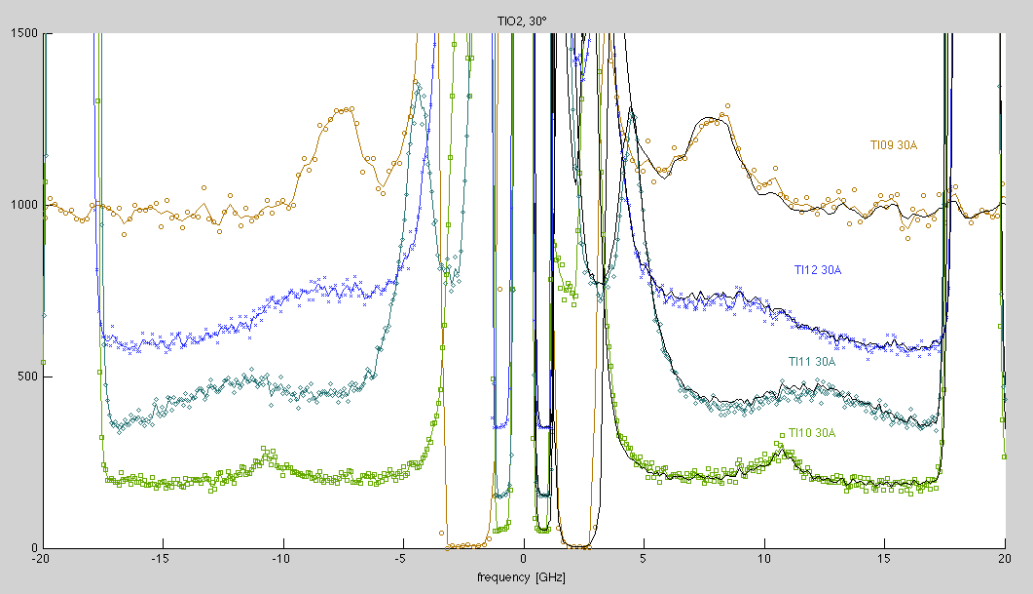


**Fig.5.27** $TiO_2$ 109, 110, 111, 112 taken at θ=30°. Mirror spacing is lower (d=3 mm) in the case of $TiO_2$ 109, to have a better resolution and to include also the peak at high frequency, visible only in this sample.

We can see that increasing the pressure of deposition, the peak at about 10 GHz becomes more dispersed and the peaks frequency seem to decrease increasing the pressure.

The following figures 5.28, 5.29 and 5.30 present the spectra of all the samples taken at θ=40°, θ=50° and θ=70°, respectively.

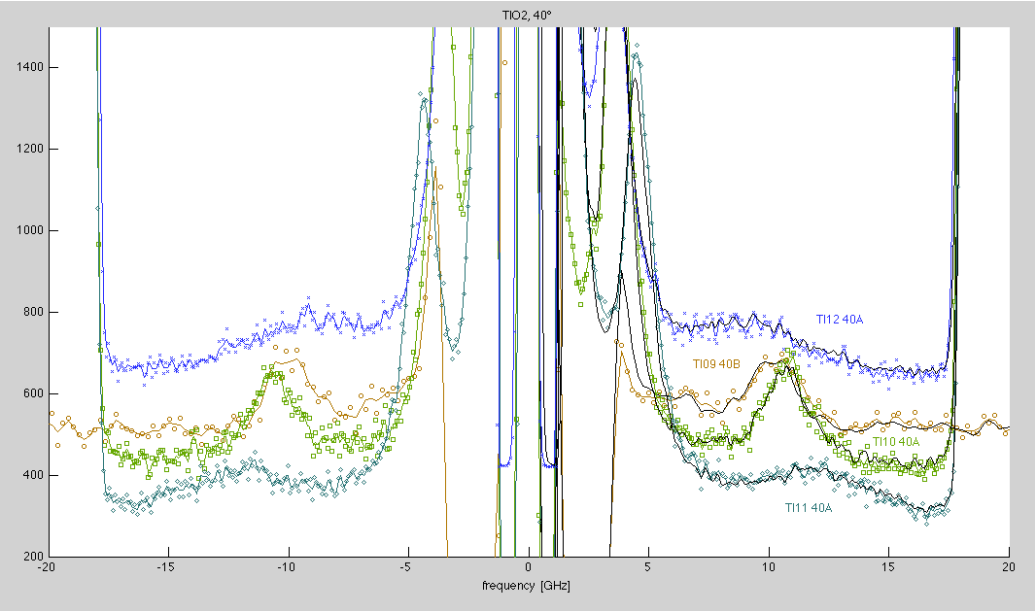


**Fig.5.28** $TiO_2$ 109, 110, 111, 112 taken at θ=40°. Mirror spacing is d=3 mm for TI09_40A and d=8 mm for the other three samples.

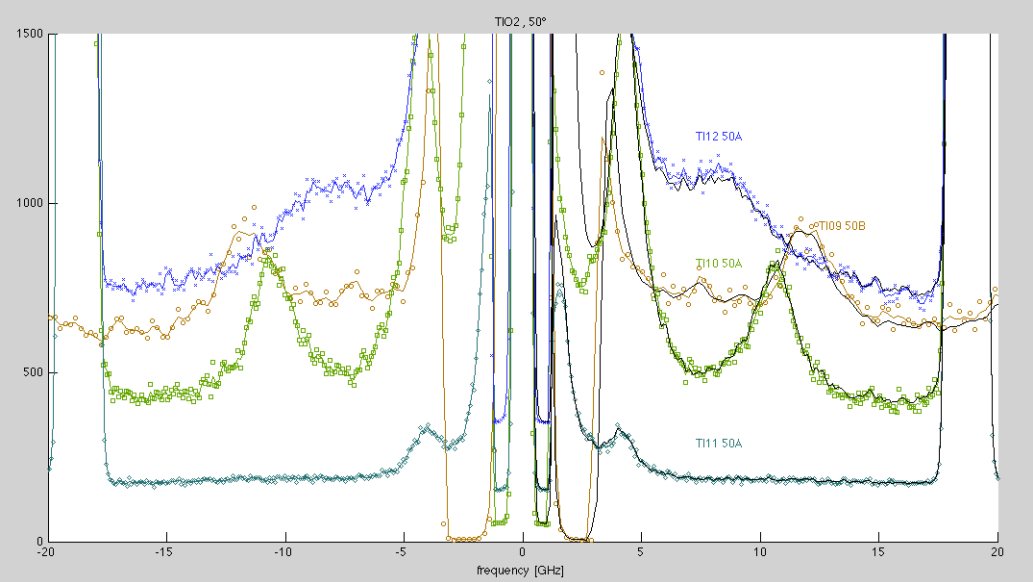


**Fig.5.29** $TiO_2$ 109, 110, 111, 112 taken at θ=50°. Mirror spacing is d=3 mm for TI09_40A and d=8 mm for the other three samples.

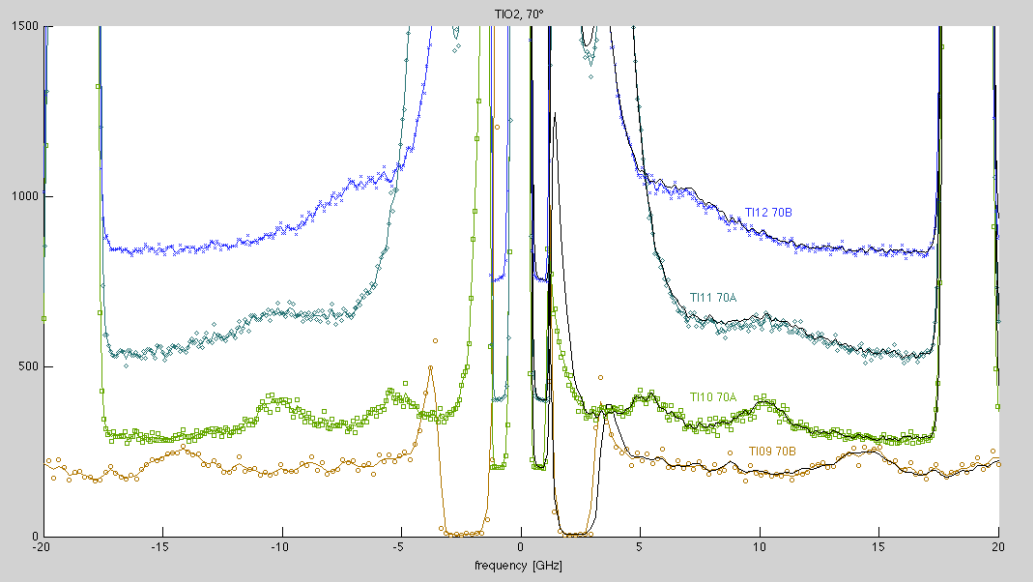


**Fig.5.30** $TiO_2$ 109, 110, 111, 112 taken at θ=70°. Mirror spacing is d=3 mm for TI09_40A and d=8 mm for the other three samples.

Looking at the figures above, we can see that for the two samole produced at higher pressures (15 Pa and 10 Pa) the two peaks appear to be more disperse, while in the case of $TiO_2$ 109 and 110, produced at 5 Pa and 7 Pa respectively, the peaks are more intense and sharply defined. We clearly see that peaks positions and, so peaks frequencies, slightly change from a sample to another taken at the same incidence angle. What kind of dependance there is between frequencies and $\theta$ or $\sin\theta$ will be the object of the following chapter, which is focused on the spectra analysis.

# Chapter 6

In this chapter we are going to present the results we have obtained in terms of variation of the peaks frequencies with the incidence angles. Our aim is to estabilish what kind of acoustic wave is associated to the peaks we found in the spectra.

In the first part we collect all the graphs that show the trends between the fitted frequencies and the incidence angles for all the samples of the second group. We have decided to focus on this batch of samples because they revealed to be more interesting from the vibrational point of view. As we have already noted, we found strong differences in the trends between frequencies and angles in samples produced at similar pressures (5 and 7 Pa) and with very similar microstructures. In this chapter we also show some SEM images of the samples to compare their morphological structures.

In the second part of the chapter, we present the attempts we have done to attribuite the peaks to certain acoustic waves, taking in consideration the trends presented in the prevuois section but also the SEM images, which could be helpful also to understand the vibrational behaviour.

## 6.1 Analysis of the Results

In this section we are going to discuss critically the results obtained from the Brilluoin spectroscopy measurements. We will focus on the peaks found in the spectra of the second group of samples taken at different angles and in particular we will try to evaluate which is the trend between frequencies (or also velocities) and the incidence angles (or their sine). In the case of the first batch of samples, we do not have many measurements at different angles because originally we focus our attention in the lateral exploration of the samples to try to “map” them changing everytime the position of measure.

### 6.1.1 Relation between Frequency and Incidence Angle

Here we carry out the analysis of the spectra starting form the trends of variation of frequency with the angle θ identified in an approximative way in the previous chapter. The following figures show some charts that we have done with excel. These charts represent frequency values, already collected in the tables of chapter 5, vs sinθ, but it could be interesting also to show the trends between velocities and angles.

First of all, we report some charts related to the first group of samples, where we consider the variation of the measured frequencies due to the change of the point of measure on the sample. In general, every excel chart is preceeded by the relative chart with the addition of error bars, to have an idea of the extent of uncertainties to make the trends more realistic. The uncertainties shown as error bars in the following figures are not only those derived from the fitting procedure applied on the peaks (that are generally fitted with gaussians) but are calculated with the "error propagation formula" through a MATLAB function (see par.3.2.4). If the graphs are presented as velocity vs θ or sinθ, the velocity must be converted into frequency and so the relative uncertainty:

$$v = \frac{\omega}{k_{\parallel}} = \frac{2\pi f}{2\frac{2\pi}{\lambda_0}\sin\theta} = \frac{\lambda_0 f}{2\sin\theta} \Rightarrow \Delta v = \Delta f \frac{\lambda_0}{2\sin\theta} \Rightarrow \Delta f = \Delta v \frac{2\sin\theta}{\lambda_0} \qquad \textbf{(6.1)}$$

where $\lambda_0$ is the laser wavelength, θ is the incidence angle and $\Delta v$ is the relative shift in velocity.

The so calculated uncertainty related to the frequency or velocity must take into account also another uncertainty. This is due to the geometrical imperfections of the scattering set-up. An analysis of the experimental procedure allows to estimate at 0,2 degrees the uncertainty $\sigma_\theta$ of the incidence angle θ. This adds to the total uncertainty a contribution given by:

$$\left(\frac{\sigma_\theta}{\tan\theta}\right)^2 \qquad \textbf{(6.2)}$$

First of all, we present the graphs related to the first group of samples, even if they reveal to be not very useful for our analysis. At the beginning of our campaign of measurements, we perform measurements on few samples, almost all produced at the same pressure (10 Pa), trying to "map" them to see if there were evident differences between different points of measure. We focused on the lateral exploration of the samples and not on the analysis of the vibrational behaviour changing the pressure of deposition. This has been done at different angles and we show the results obtained with θ=50° and θ=60° .

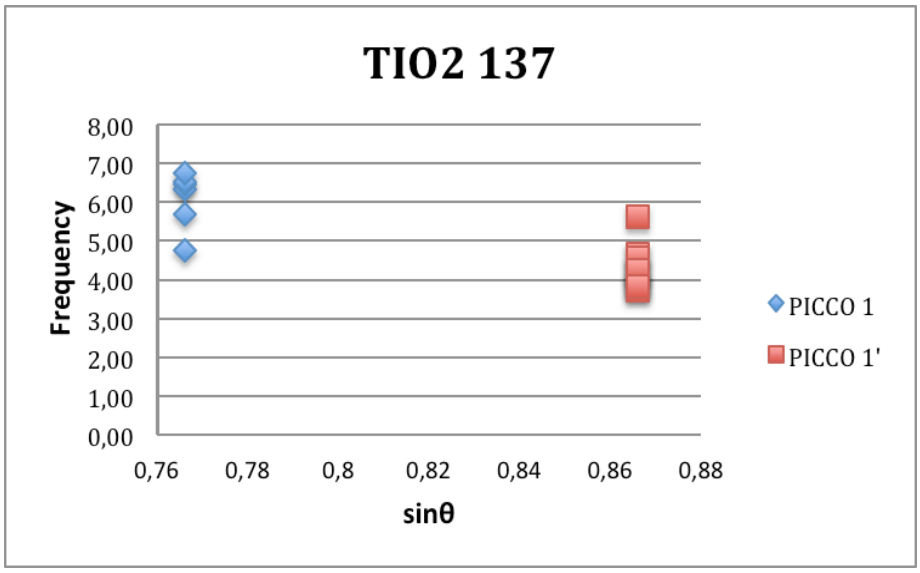


**Fig.6.1** Chart of the variation of the first peak frequencies, fitted on the spectra of $TiO_2$ 137, with θ, changing the position of the beam on the sample.

The graph, presented in figure 6.1, shows the fitted frequencies of the first

considered sample, $TiO_2$ 137 (10 Pa). Considering the cases of θ=50° and θ=60°, the relative variations of the measured frequencies are:

$$\frac{f_{max} - f_{min}}{f_{min}} = \frac{6,76 - 4,76}{4,76} = 0,42$$

$$\frac{f_{max} - f_{min}}{f_{min}} = \frac{5,73 - 3,73}{3,73} = 0,53$$

These variations are not negligible and are probably due to a not really uniform structure and/or to inhomogenities in the sample thickness. In the light of this result, for all the subsequent measurements the measurement zones were selected aiming at uniform thickness regions, which could be easily identified by the interference fringes.

The first case analysed after $TiO_2$ 137 (10 Pa), is the annealed sample produced at the same pressure $TiO_2$ 137 A (10 Pa). In this case, as we have already noted in the previous section, the spectra obtained from this sample are not so easy to fit and there are no clearly evident peaks. This could be explained as an effect of annealing which is the re-packing of the atomic structure. If the peaks visible in the spectra before annealing were due to travelling waves, the effect of annealing would be to make even more easy for this waves to travel along a more compact structure. An interpretation of this mismatch could be the fact that we probably haven't travelling waves but standing waves. Unfortunately, we cannot say much more about the characteristics of this kind of waves with the data collected from the spectra analysed until now. However, we can gain some qualitative information from the analysis of the SEM images of $TiO_2$ 137, presented in the following three figures:

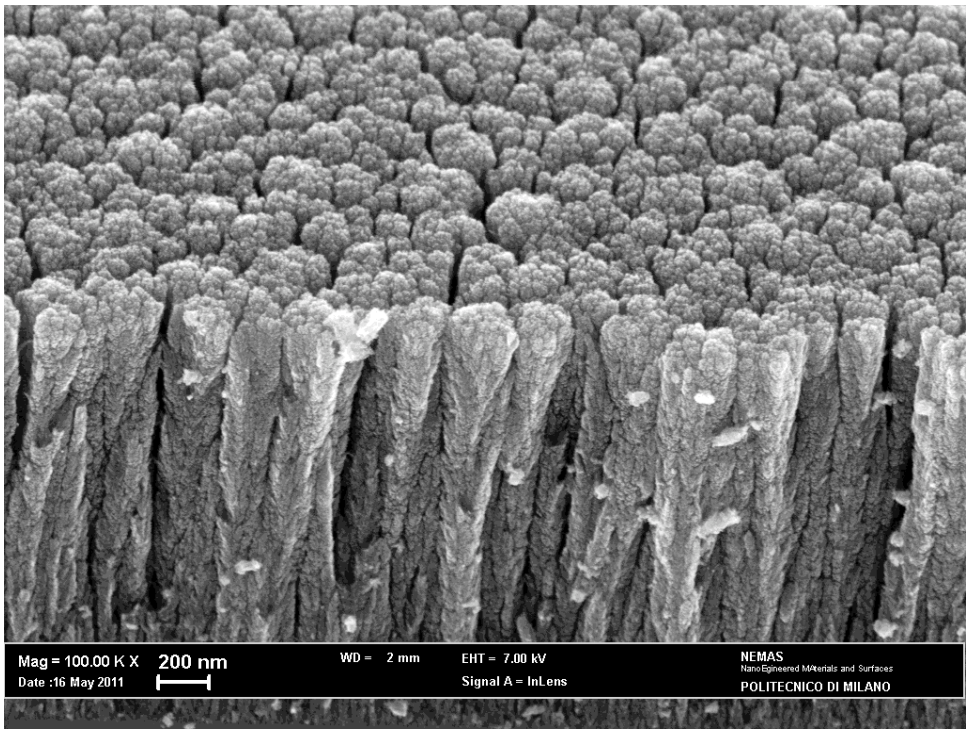
Mag = 100.00 K X
200 nm
Date :16 May 2011
WD = 2 mm
EHT = 7.00 kV
Signal A = InLens
NEMAS
NanoEngineered MAterials and Surfaces
POLITECNICO DI MILANO

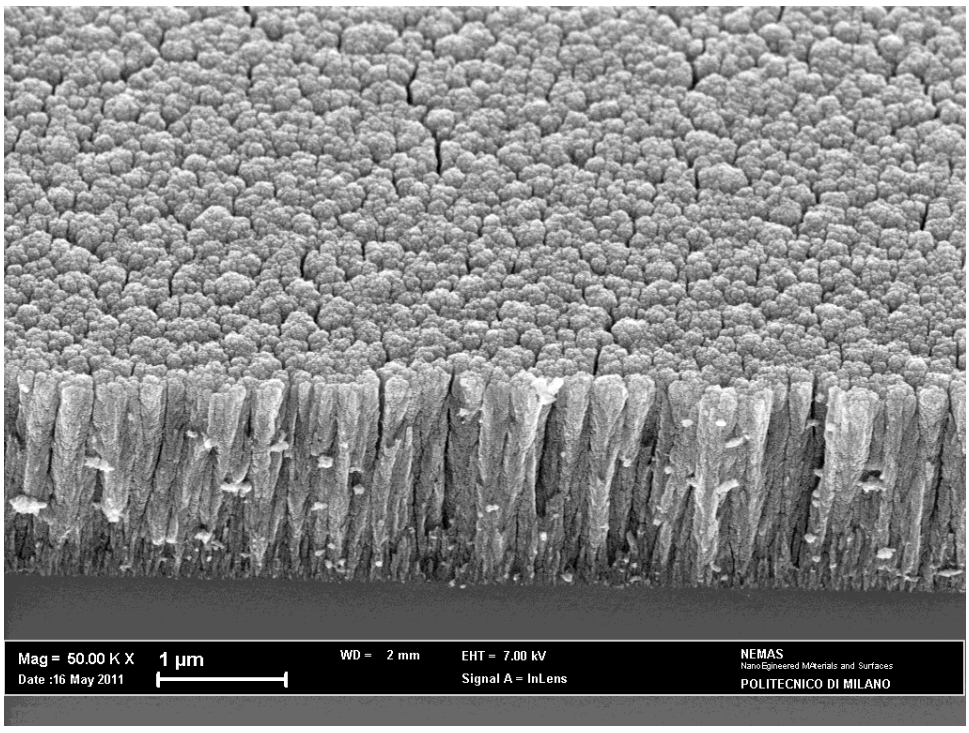
Mag = 50.00 K X
1 µm
Date :16 May 2011
WD = 2 mm
EHT = 7.00 kV
Signal A = InLens
NEMAS
NanoEngineered MAterials and Surfaces
POLITECNICO DI MILANO

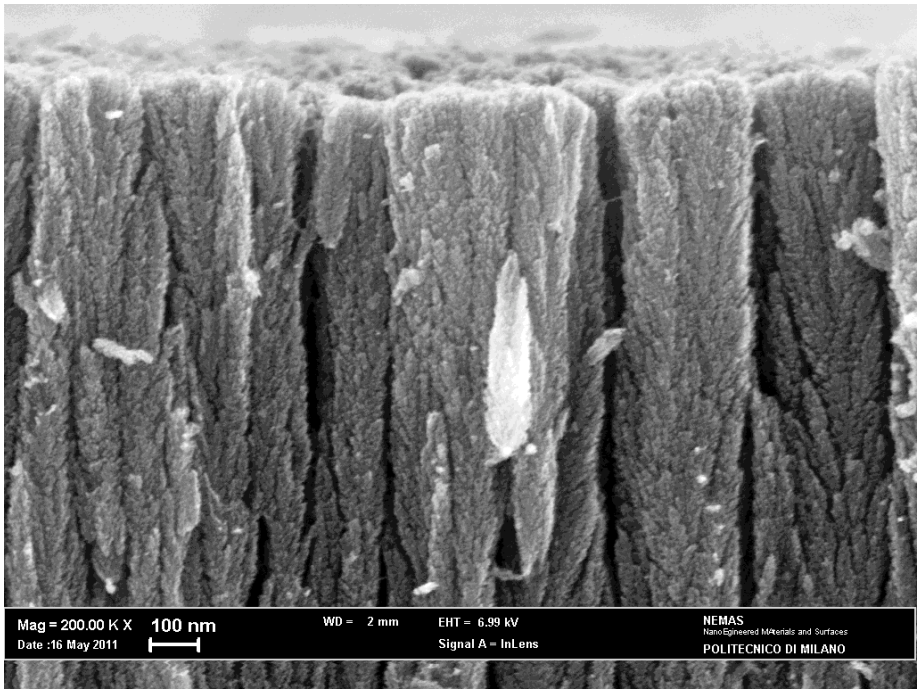


**Fig.6.2,3,4** SEM images of $TiO_2$ 137 (10 Pa): these can be helpful to make some considerations about the morphological structure and the vibrational behaviour.

These images show the $TiO_2$ 137 (10 Pa) sample microstructure before annealing. We can see that the film presents a strong "columnar" structure, made of many columns with a slightly cylindrical shape. The length of these columns is equal to the film thickness and the diameter is of the order of 100 nm. We can observe from figure 6.4 that these columns seem to be all "attached" at the bottom and tends to become more independent as their length increase. This is why we affirm that the structure of the columns is not really cylindrical but probably more conical: beside this fact, considering these structure as slighlty independent cylindrical rods can be a fair approximation. The broad shape of some peaks, which are not really intense and well-defined, probably accounts for this more dispersed structure, with conical rods that interact with each other. Figure 6.3 shows that this structure is almost uniform in the whole film.

The information that we can achieve from these images can be a proof of the fact that we are probably dealing with columnar modes which tend to disappear or to be more dispersed when the structure becomes more compact, for example after the heat treatment of annealing.

Even if we performed a lot of measurements on the first group of samples, the most interesting results are those shown by the second group of samples. For this group of samples, we have made many measurements on the same sample at different angles and so we are able to estabilish a more significative connection between frequenies and angles. Here we show the charts that represent the trends of variation of the fitted frequencies vs incidence angles for $TiO_2$ 109, 110, 111 and 112, produced at increasing pressure (5 Pa, 7Pa, 10 Pa and 15 Pa, respectively). All these charts have in the x-axis the sine of the incidence angles and in the y-axis the measured frequencies. The variation of the frequency with the angle is supposed to be linear and all the charts show the trendlines relative to each peak. As we have already introduced, we first show the graphs with the error bars added on the points and then the relative excel charts.

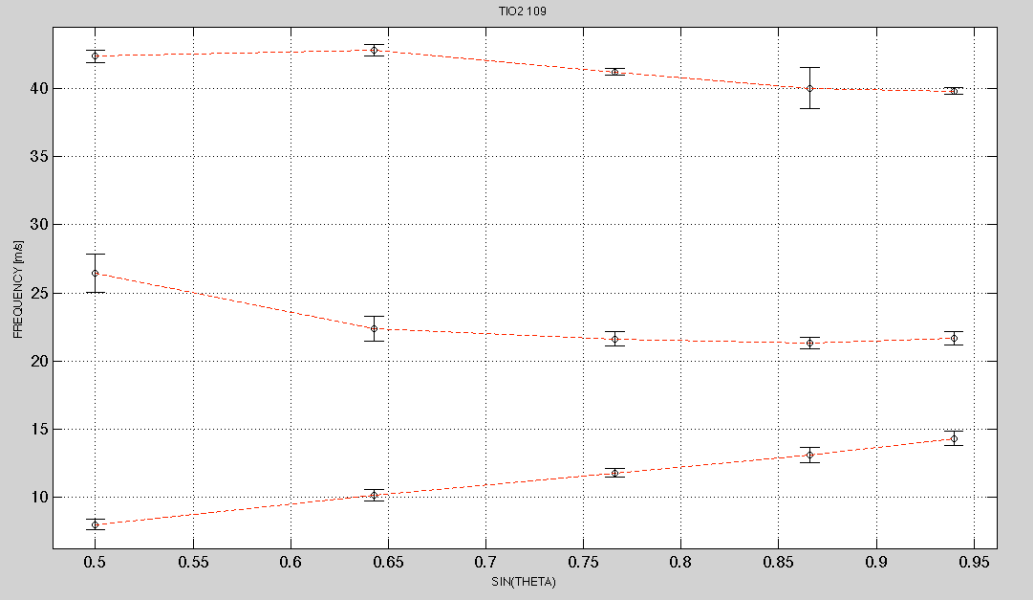


**Fig.6.5** Chart of the trends of the three peaks observed in $TiO_2$ 109 spectra with the error bars added on the points.

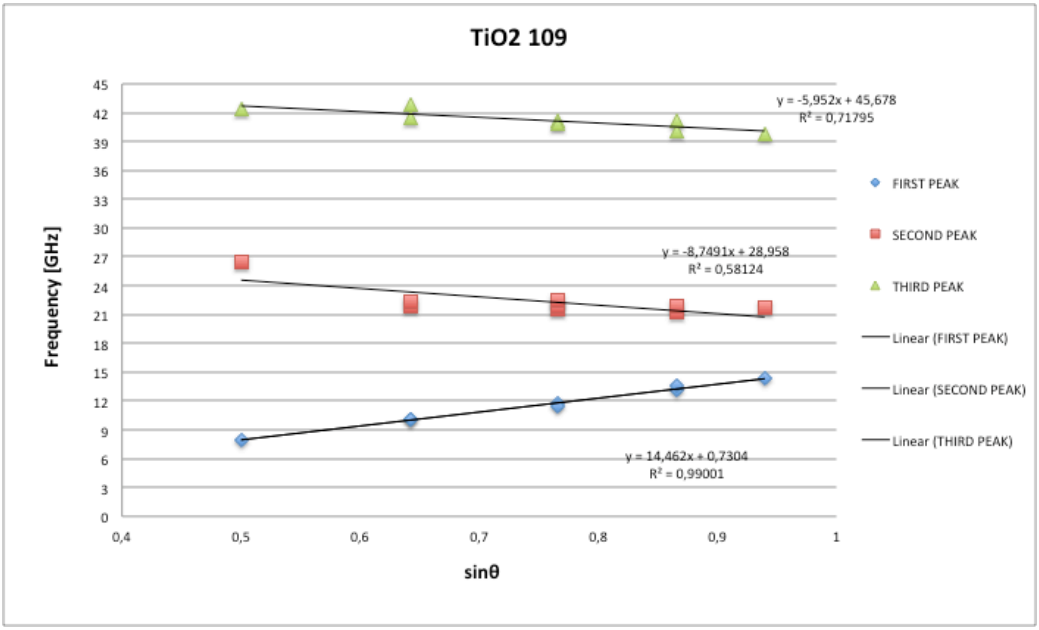


**Fig.6.6** Chart of $TiO_2$ 109 measured frequencies of all the three peaks in function of different θ ranging from 30 ° to 70°. In the figure are also shown the trendlines for each fitted peak.

The sample produced at the lowest pressure ($TiO_2$ 109, 5 Pa) was the only one with three evident peaks. The second and the third peak seem to have a slighlty decreasing trend, especially the second one. Actually, the third peak frequency seems to be almost constant with the angle, if we consider that the relative difference between the maximum frequency and the minimum one is of the order of 7%. We can observe in figure 6.5 that the error bars in the case of the peaks $TiO_2$ 109 (5 Pa) are almost all of the same order and are quite short: this means that the uncertainties associated to the fitting procedure are quite low. We could affirm this fact just after having observe the peak shape and intensity in the case of $TiO_2$ 109: these are the most well defined and probably the most intense between all the peaks of the various spectra we have collected.

After that, we present the same graphs for another sample, $TiO_2$ 110 produced at 7 Pa. Our aim is to compare the trends of the peaks to obtain information on the nature of the acoustic waves propagating in each film. The following figures show the graphs of the trends of frequency vs $\sin\theta$ for the two peaks of $TiO_2$ 110. Also in this case, we show the charts with the uncertainties added as error bars on the points and then we show the excel charts of the trends of the various peaks.

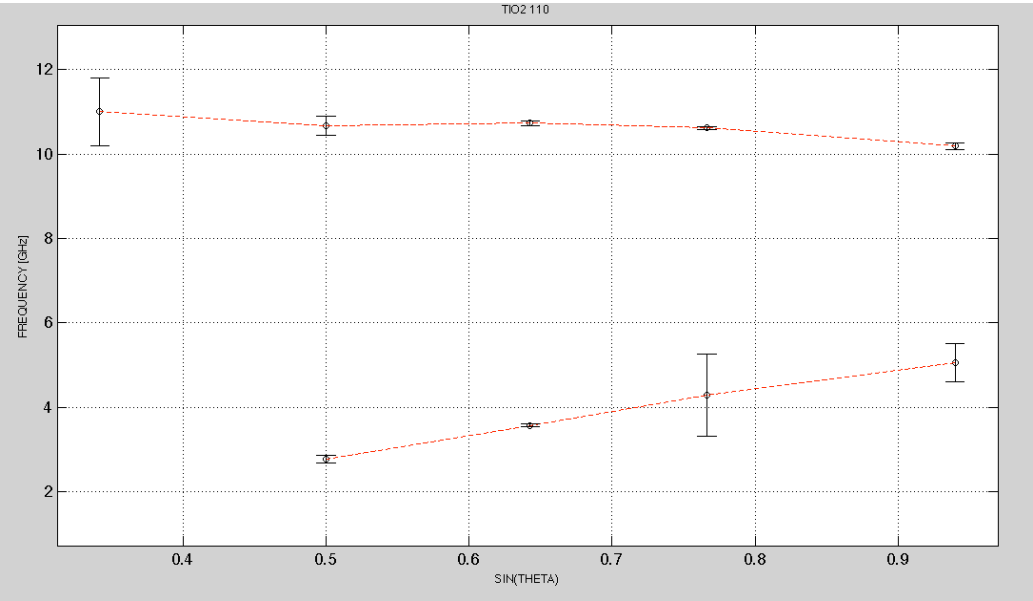


**Fig.6.7** Chart of the trends of the two peaks observed in $TiO_2$ 110 (7 Pa) spectra with the error bars added on the measured points.

For what concern uncertainties, we can note in figure 6.7, especially in the case of the second peak, a fact which has been already introduced in the paragraph of chapter 3 dedicated to the assesment of uncertainties. The error bars on the points of the measurements taken with lower angles (20° and 30°) seem to be larger than those on the other points. This is an effect of the finite collection angle that tends to increase when the scattering angle decreases.

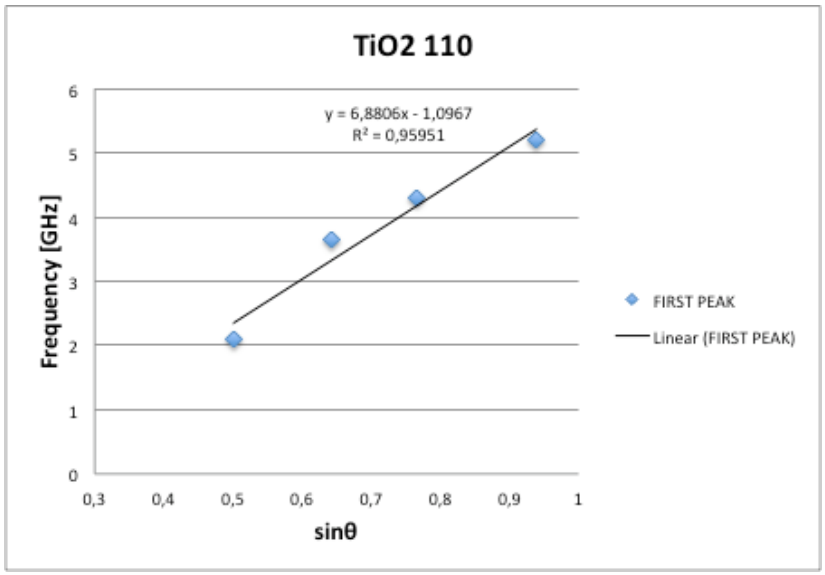


**Fig.6.8** Chart of $TiO_2$ 110 measured frequencies of the first peak in function of different θ ranging from 30 ° to 70°.

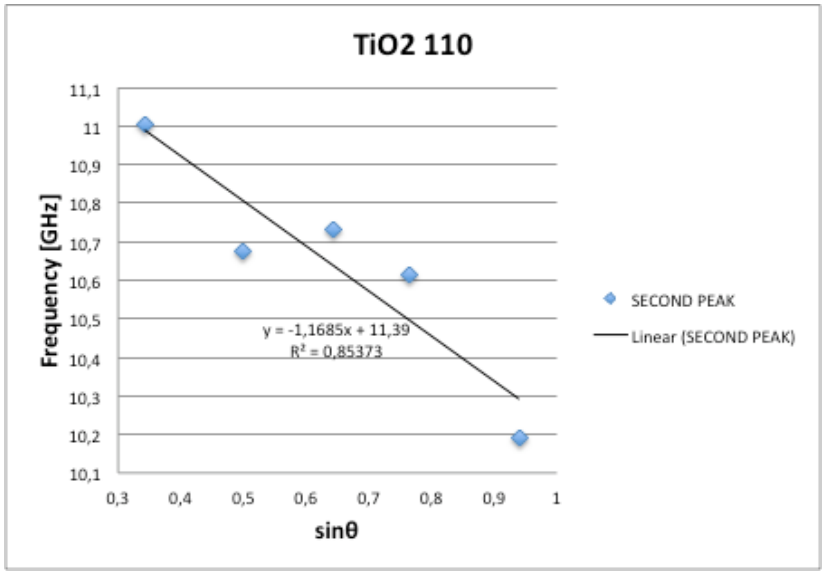


**Fig.6.9** Chart of $TiO_2$ 110 measured frequencies of the second peak in function of different θ ranging from 20 ° to 70°.

In the case of $TiO_2$ 110, the two peaks we have obtained show an almost opposite trend; the first one is essentially proportional to the sine of the incidence angle while the second one is slightly decreasing. An interesting thing that we can note looking at these charts is that the second peak of $TiO_2$ 110 (7 Pa) (see fig.6.9) and the first peaks of $TiO_2$ 109 (5 Pa) (see fig.6.6), which are both at about 11-12 GHz, have opposite trends. In fact, the former has a decreasing trend while the latter has an increasing trend with θ. This is a quite surprising phenomenon: a slight difference in pressure causes a very strong difference in the vibrational behaviour of the structure. Instead, the morphologies of the two samples as shown by the SEM images are not so different, as it can be seen in figures 6.10-14.

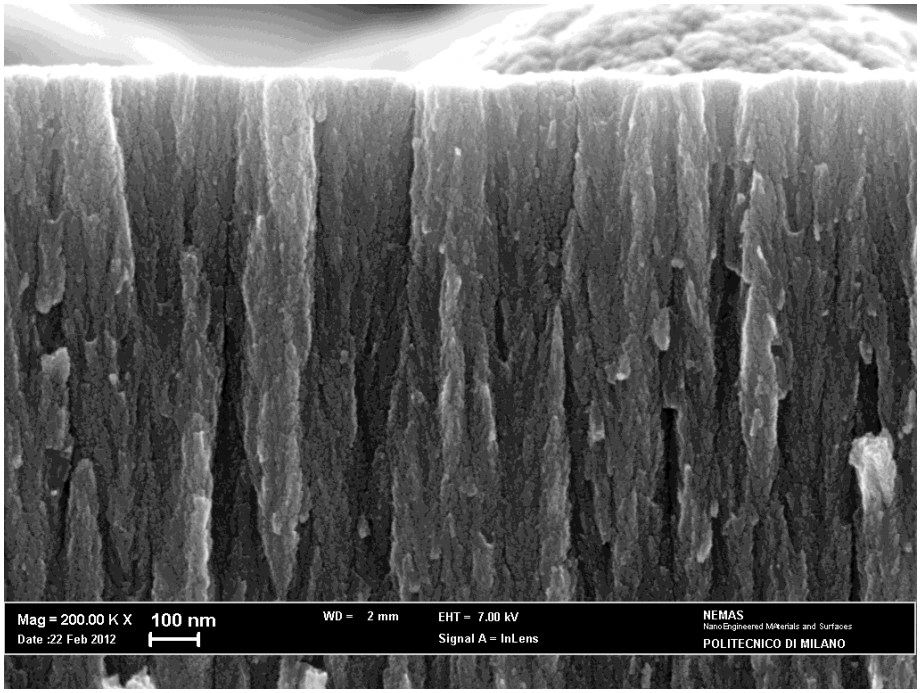

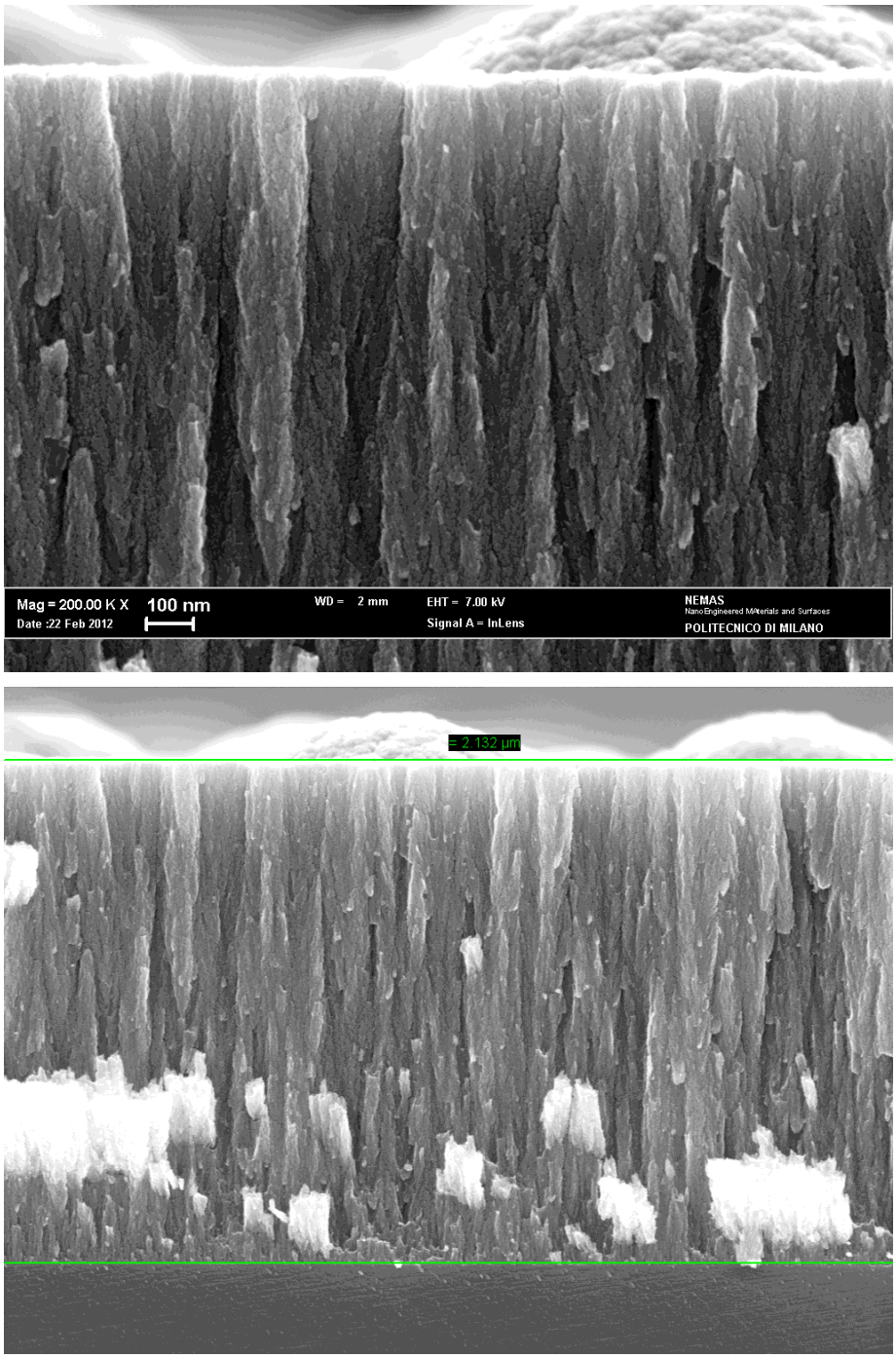


**Fig.6.10,11,12** SEM images of $TiO_2$ 109 (5 Pa). Figure 6.12 shows also the measured thickness of the film.

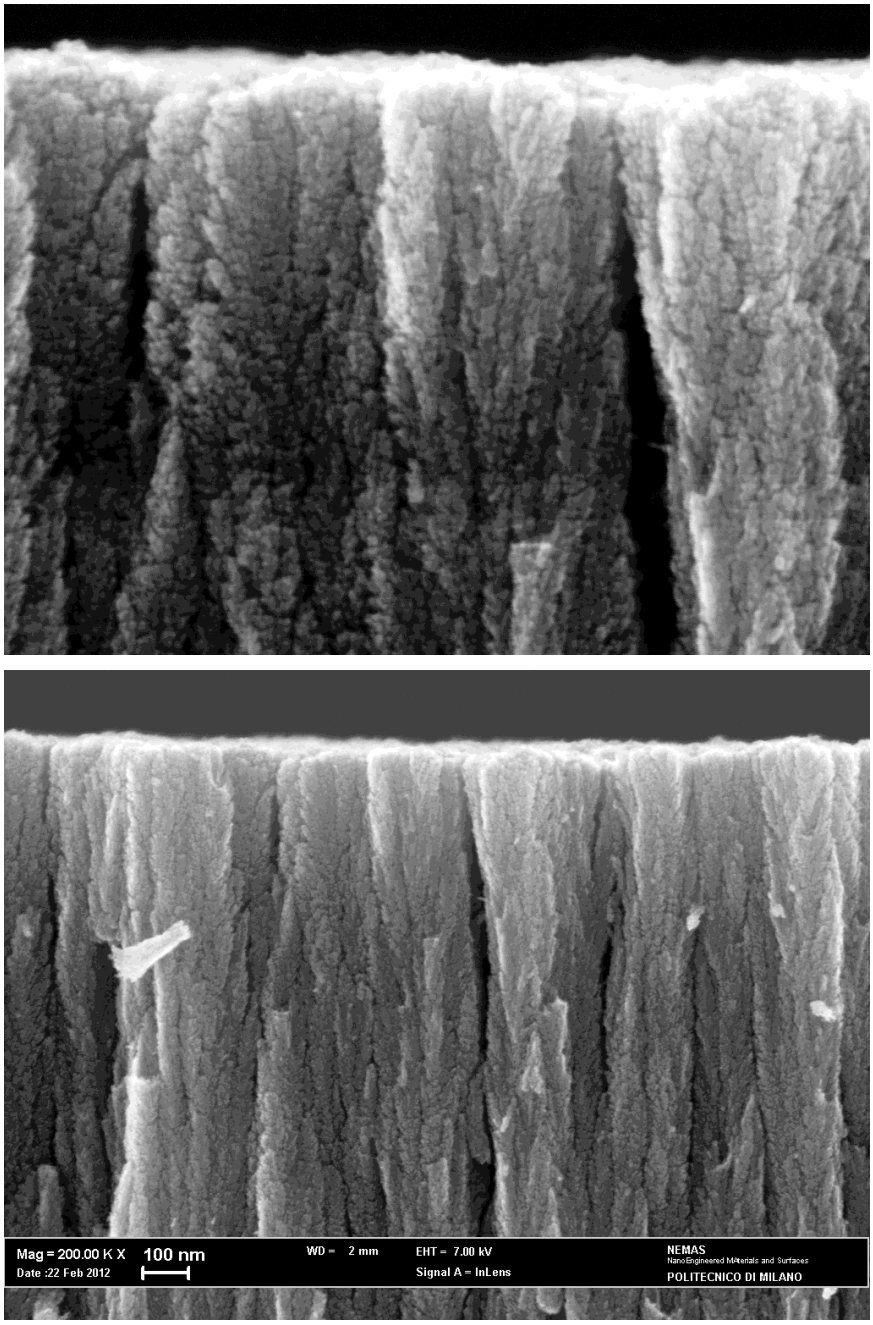


**Fig.6.13,14** SEM images of $TiO_2$ 110 (7 Pa). The columnar structure that we have already observed in the first sample analysed $TiO_2$ 137 is clearly visible. In figure 6.13 we can note that the column, of about 100 nm of diameter, begin to become more independent respect to the case of $TiO_2$ 109 (5 Pa).

In the case of $TiO_2$ 110, produced at a higher pressure (7 Pa), the columns tend to be more "separated" than in the case of $TiO_2$ 109 (5 Pa) but the overall structure do not present strong macroscopic differences. In both materials we have an extended columnar structure made of more or less cylindrical rods. This strongly different vibrational behaviour, in the absence of evident morphological differences is one of the most interesting results of this analysis. However the SEM images confirm that the sample $TiO_2$ 109 produced at 5 Pa has, as expected, the most compact structure.

We now consider the results obtained from the $TiO_2$ 111 (10 Pa) and $TiO_2$ 112 (15 Pa) samples. Also comparing the trends observed in $TiO_2$ 110 (7 Pa) and $TiO_2$ 111 (10 Pa) we meet unexpected results and interesting differences. The peak at around 4 GHz, that we named "first peak", has approximately the same frequency in the two samples, but with opposite variations with the incidence angle: in the former case, the frequency increases proportionally to $\sin\theta$ while in the latter case it is slightly decreasing with $\theta$.

We show below the dispersion relations and the SEM images. We find again the same columnar structure of the other samples, where the columns continue to become more independent as the deposition pressure increase (Fig.6.17 and 6.18). Figure 6.19 shows the not properly cylindrical but more conical shape of the columns.

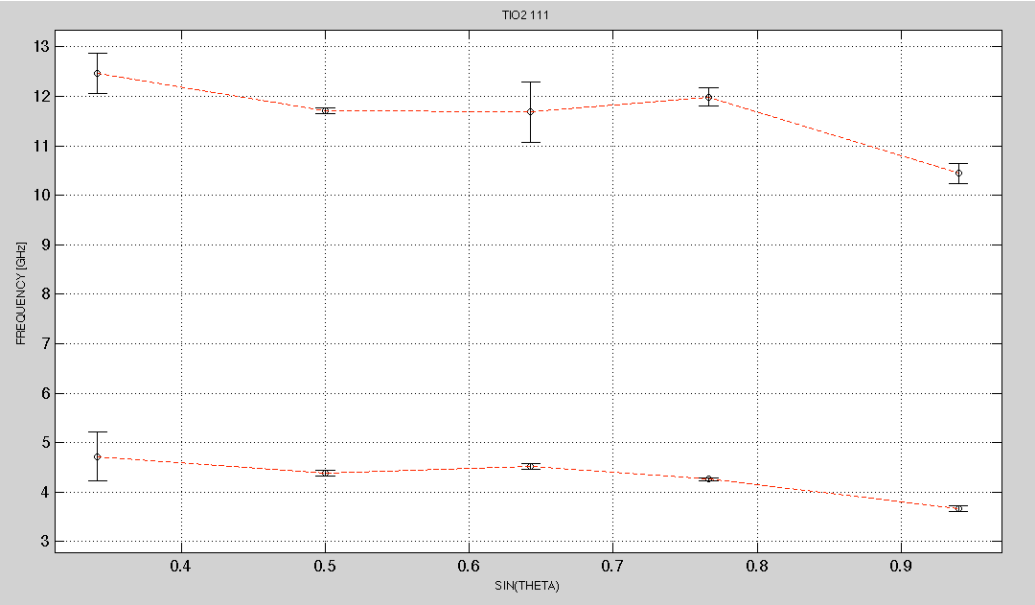


**Fig.6.15** Chart of the trends of the two peaks observed in $TiO_2$ 111 (10 Pa) spectra with the error bars added on the measured points.

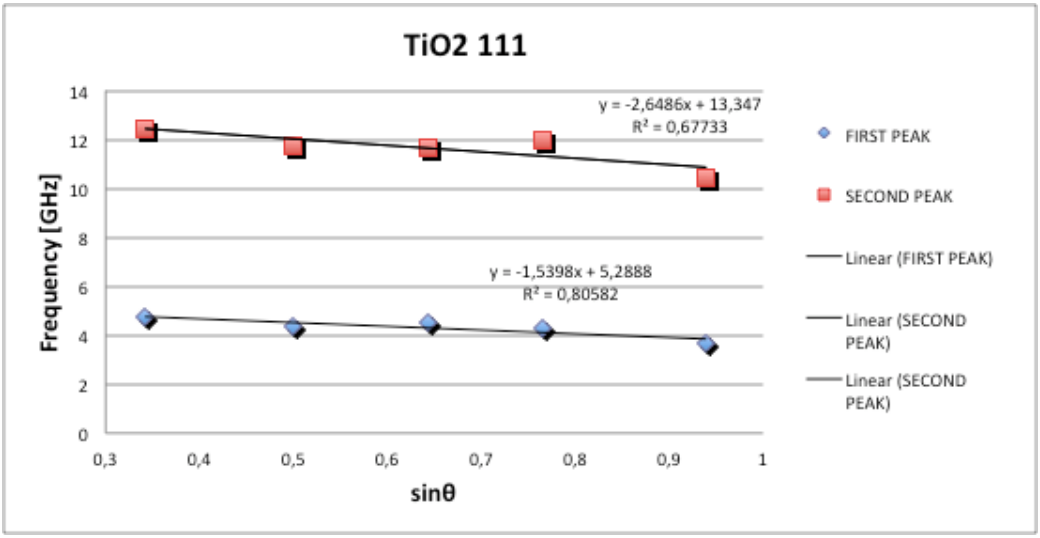


**Fig.6.16** Chart of $TiO_2$ 111 measured frequencies of both the two peaks in function of different θ ranging from 20 ° to 70°.

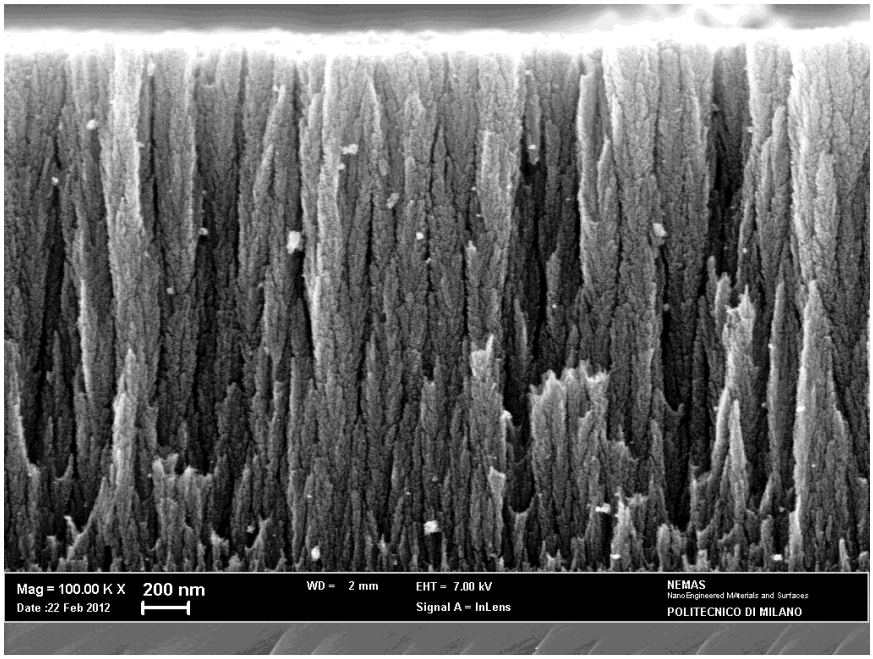


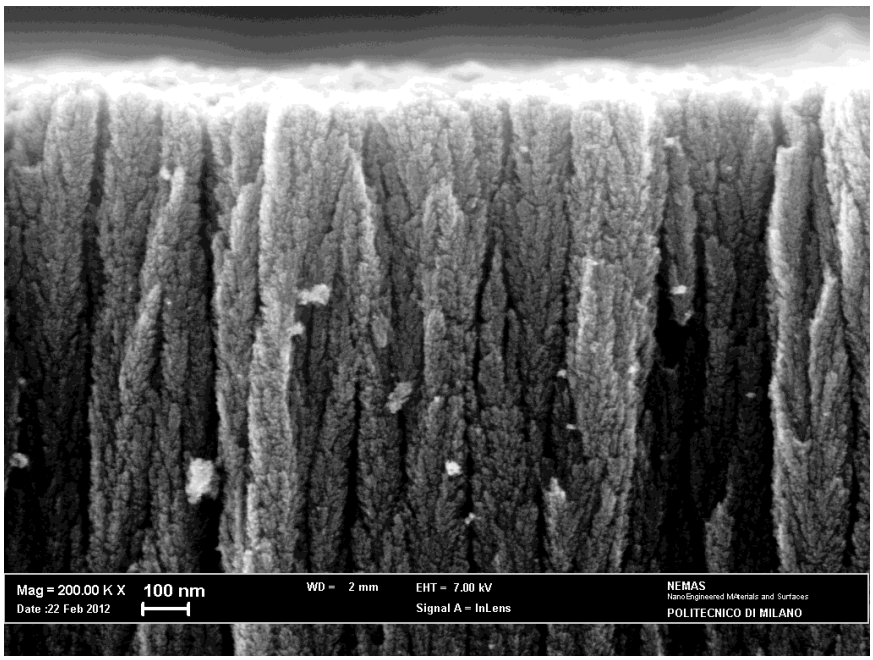


**Fig.6.17,18** SEM images of $TiO_2$ 111 (10 Pa) at different scales. Comparing figure 6.17 with figure 6.13 we can see that the columns become more separated (the empty spaces between them, in black, seem to increase and to become wider).

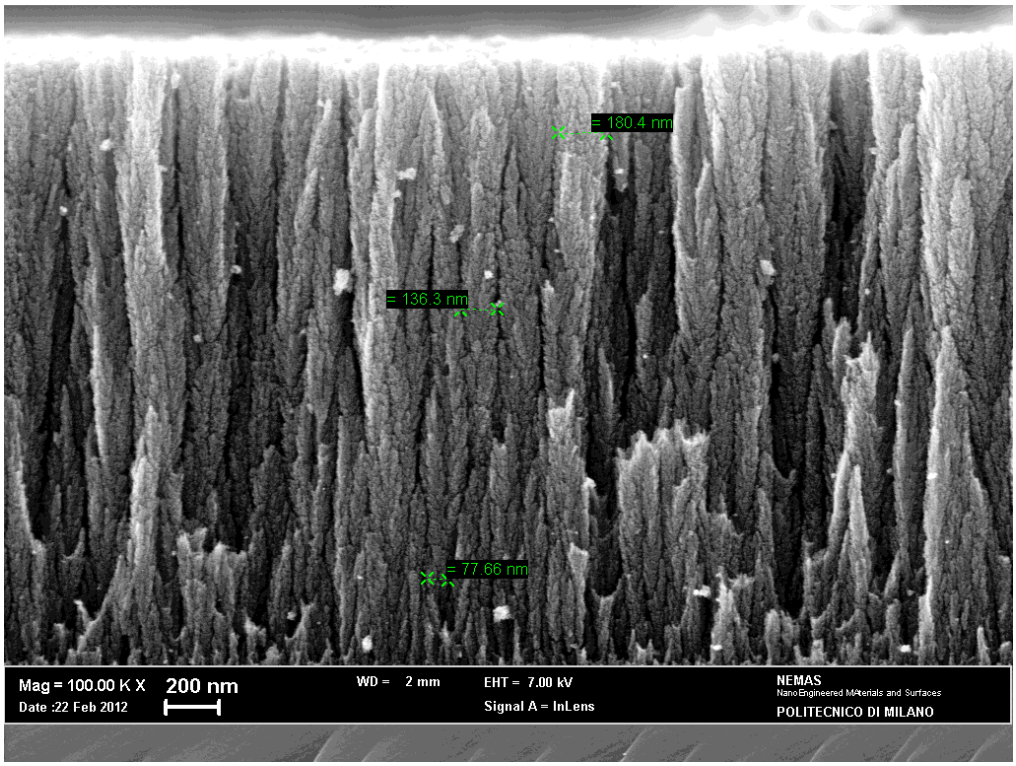


**Fig.6.19** SEM image of $TiO_2$ 111 focused on the concical shape of the columns. The width increases from about 78 nm at bottom to 180 nm at top.

Figure 6.20 and 6.21 show the dispersion relation for the two peaks observed on the sample $TiO_2$ 112 (15 Pa). The trends are essentially both decreasing with the incidence angle, as we have observed for the $TiO_2$ 111 (10 Pa). We can note that for this sample the frequencies uncertainties are larger than found in prevuious samples. This is due to the lower intensity of peaks and to the very low frequency of the first peak which is very close to the intense elastic peak.

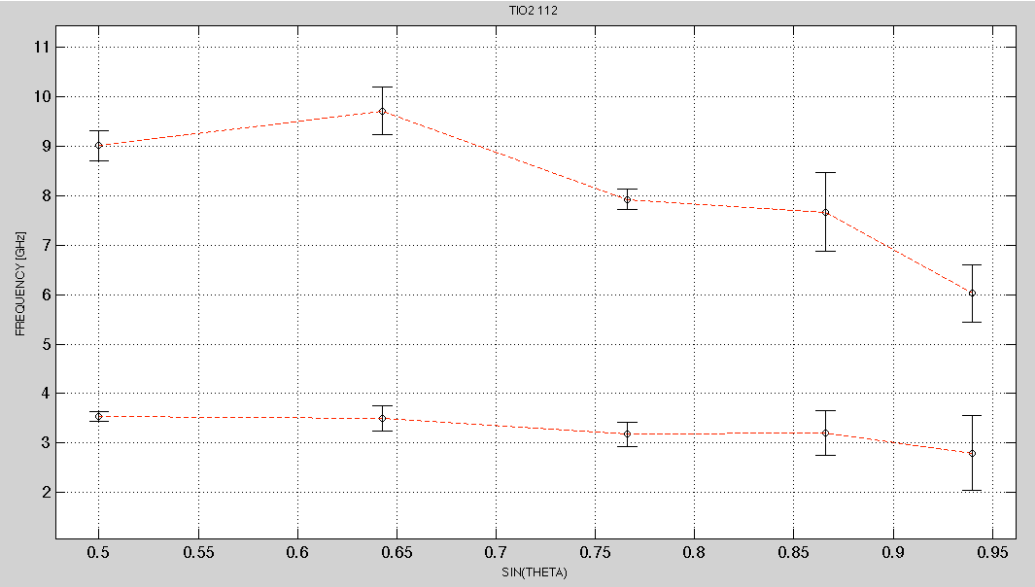


**Fig.6.20** Chart of the trends of the two peaks observed in $TiO_2$ 112 (15 Pa) spectra with the error bars added on the measured points.

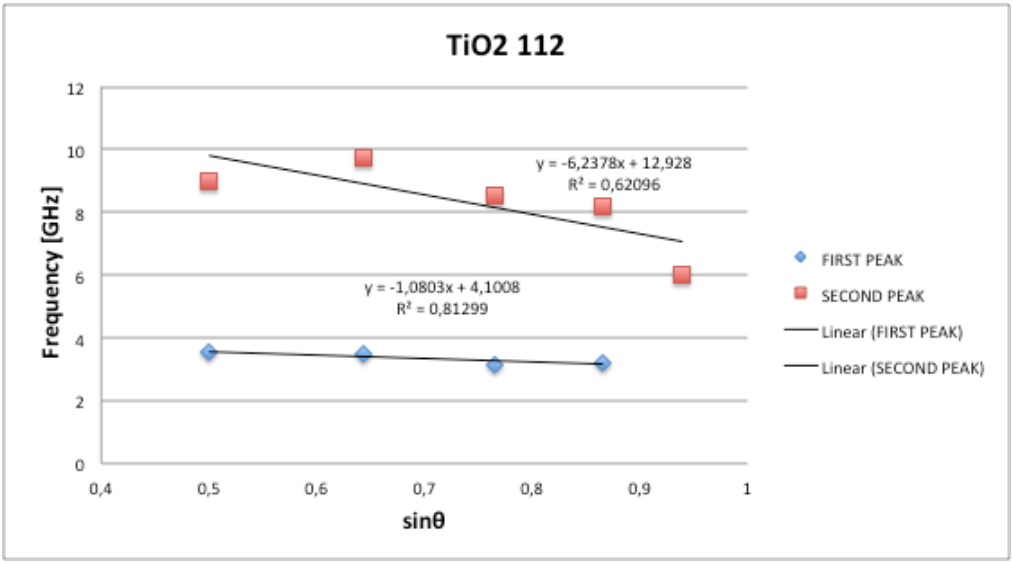


**Fig.6.21** Chart of $TiO_2$ 112 measured frequencies of both the two peaks in function of different θ ranging from 30 ° to 70°.

For the sake of completeness, we present also the SEM images of this sample. We can confirm that as the pressure increases the structure becomes less compact and the columns tend to separate even more, at least in the upper part of the column.

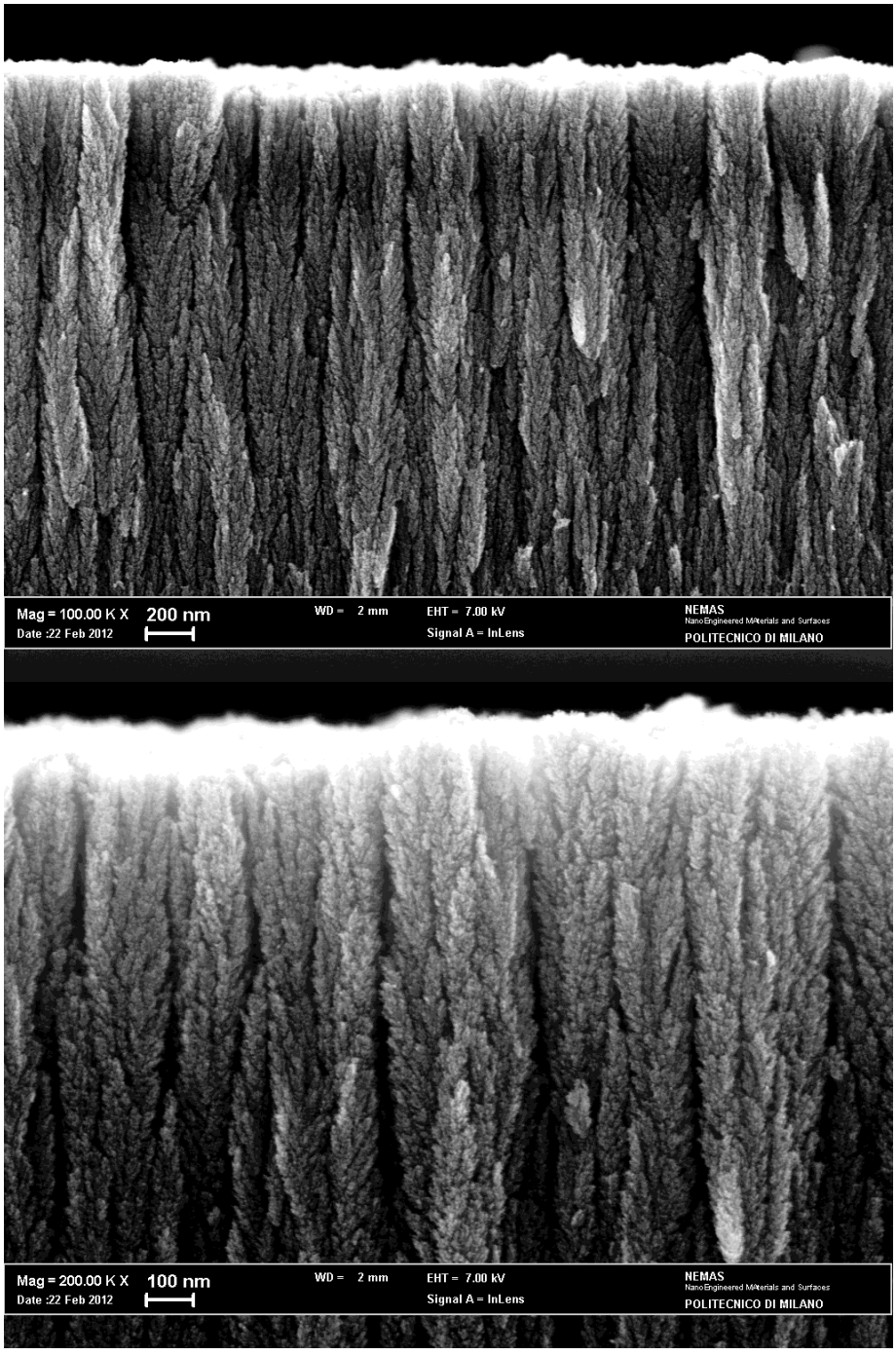

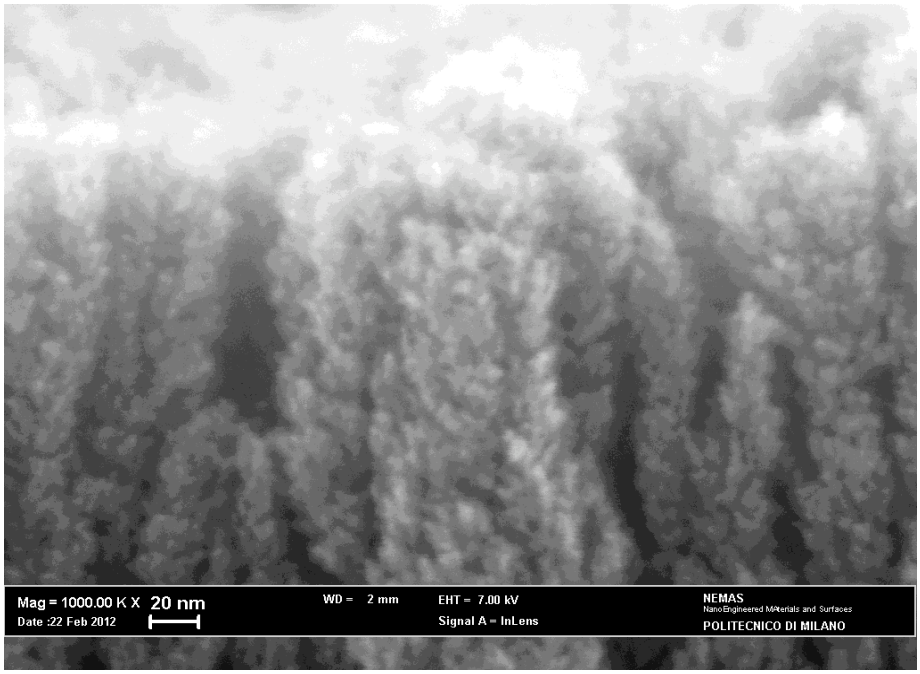


**Fig.6.22,23,24** SEM images of $TiO_2$ 112 (15 Pa). The images are taken at different length scales (200 nm, 100 nm and 20 nm). The first one shows the columnar structure whose columns are clearly distinct and visible.

## 6.2 Attempts of Peaks Attribution

In the former chapter we have presented the spectra obtained from Brillouin measurements on $TiO_2$ samples. The peaks in the spectra have been fitted and the so obtained frequencies or velocities have been correlated with the incidence angles to evaluate possible trends. We have discovered some surprising phenomena, such as the opposite trends of frequency vs angle between peaks at about the same frequency, from two samples with very similar morpholgies. This is the case of the $TiO_2$ 109 (5 Pa) first peak and of $TiO_2$ 110 (7 Pa) second peak, both at about 11 GHz, but also of the peaks at about 4 GHz of $TiO_2$ 110 (7 Pa) and $TiO_2$ 111 (10 Pa). Here we try to understand the origin of these peaks.

### 6.2.1 Peaks Classification from the Identified Trends

It has been already stated that there is an intrinsic difference between bulk acoustic waves and surface acoustic waves. In the case of bulk waves, both primary waves and secondary waves, the peak frequency does not depend on the incidence angle. Instead, in the case of surface waves, frequencies scale as the sine of the incidence angle and, in particular, we have

$$v = f\frac{2\pi}{k_{\parallel}} \tag{6.3}$$

where $v$ is the velocity of the surface wave, $f$ is the frequency of the peak and $k_{\parallel}$ is the wavevector parallel to the surface. In this case we have a wavevector that is proportional to sinθ,

$$k_{\parallel} \propto \sin\theta \tag{6.4}$$

Turning back to the figures 6.6, 6.7, 6.13 and 6.17 we find that in two cases the measured frequencies are almost directly proprotional to sinθ: this is the case of the first peak of $TiO_2$ 109 (5 Pa) and the first peak of $TiO_2$ 110 (7 Pa).

The figures below show the trends related to these two peaks. We suppose a relation like that expressed in equation 6.4 and so we can impose the trendline intercepts equal to zero, without committing an appreciable error (in both the situations the real intercepts are about 1,09 and 0,7).

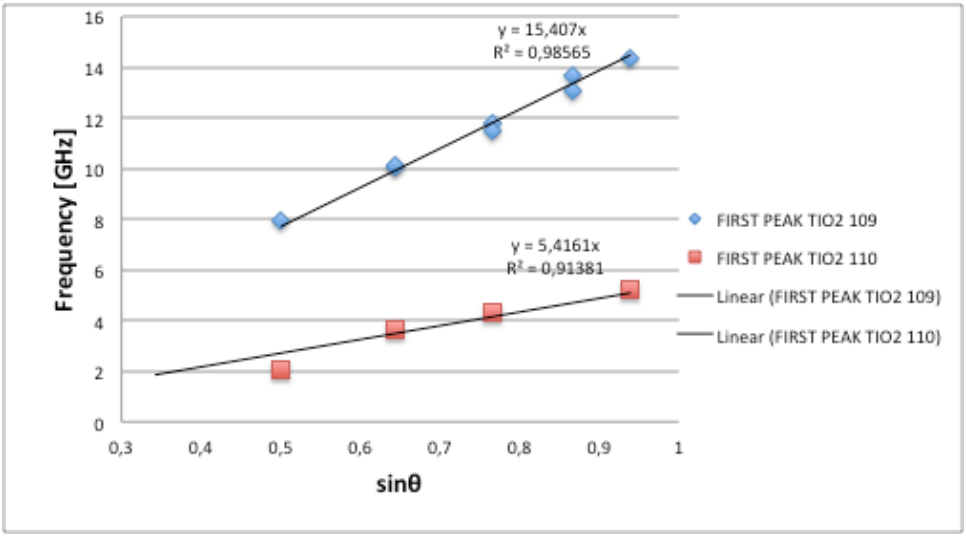


**Fig.6.25** Chart of the two peaks with the frequencies proporional to sinθ. We set the intercept of the trendlines to zero.

This behaviour corresponds to that of surface waves with a well defined velocity. The velocities derived from each incidence angle are slightly scattered as shown in table 6.1 and 6.2 and in figure 6.26 and 6.27.

| File name | Angle | Velocity [m/s] | Uncertainty [m/s] |
|---|---|---|---|
| TI10_20A | 20° | / | / |
| TI10_30A | 30° | 1432 | 24 |
| TI10_40A | 40° | 1473 | 44 |
| TI10_50A | 50° | 1478 | 88 |
| TI10_70A | 70° | 1451 | 104 |

**Table 6.1** Measured velocities of the first peak of $TiO_2$ 110 at different θ.

| File name | Angle | Velocity [m/s] | Uncertainty [m/s] |
|---|---|---|---|
| TI09_30A | 30° | 4047 | 126 |
| TI09_40A | 40° | 4076 | 65 |
| TI09_40B | 40° | 4050 | 159 |
| TI09_50B | 50° | 3916 | 84 |
| TI09_50C | 50° | 3774 | 82 |
| TI09_60B | 60° | 3879 | 1101 |
| TI09_60C | 60° | 3991 | 67 |
| TI09_70B | 70° | 3902 | 37 |

**Table 6.2** Measured velocities of the first peak of $TiO_2$ 109 at different θ.

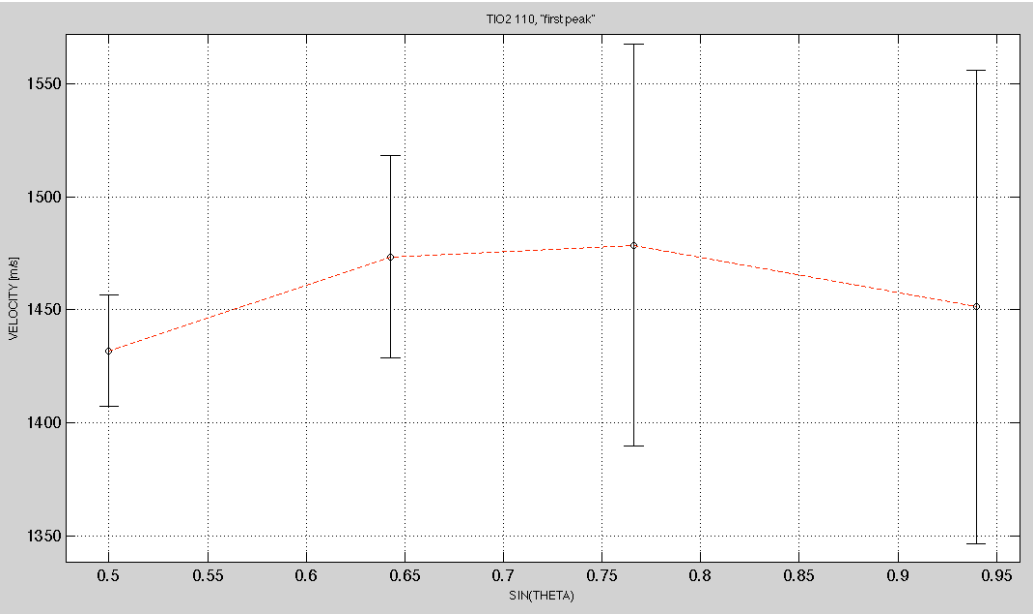


**Fig.6.26** Measured velocities for the first peak of $TiO_2$ 110.

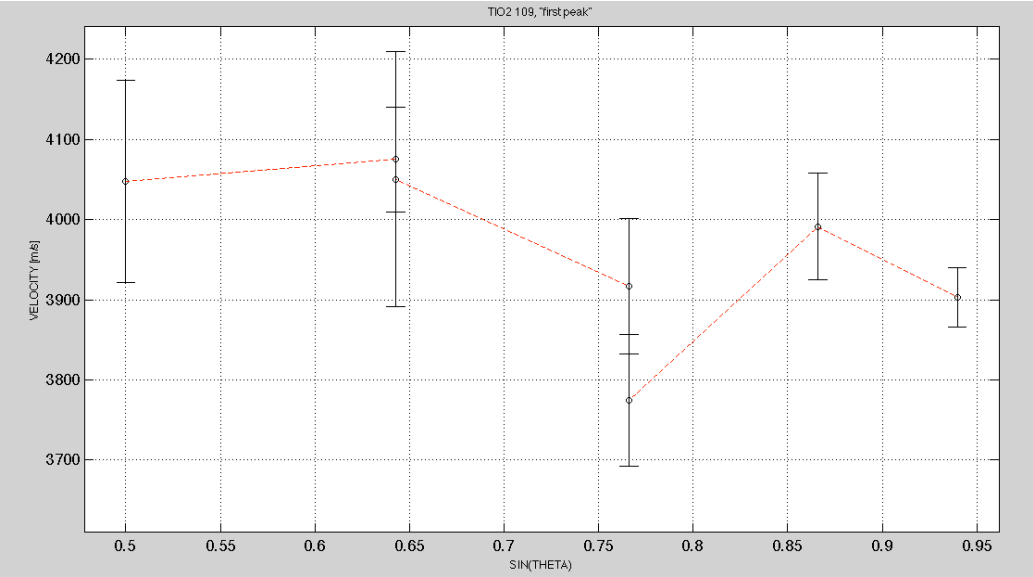


**Fig.6.27** Measured velocities for the first peak of $TiO_2$ 109.

Analysing the trends of the second peak of $TiO_2$ 110 (7 Pa) and $TiO_2$ 111 (10 Pa), we found that they both have a frequency which decreases when the incidence angle θ increases. The considerations we have done above are referred to peaks due to interaction with acoustic modes whose wavevector is parallel to the surface: the exchanged wavevector, and therefore also the frequency shift of the spectral peak, is proportional to sinθ. This is typically the case for surface waves. In fact, in backscattering configuration we have:

$$\vec{q} = \vec{k_s} - \vec{k_i} \Rightarrow q_{\parallel} = k_{s\parallel} - k_{i\parallel} = 2k_{i\parallel} \tag{6.5}$$

An opposite trend (frequency decreases while θ increases) can be related to the interaction with an acoustic mode that does not travel parallel to the surface but along the direction perpendicular to it. This could be the case for an acoustic mode traveling along the columns of the observed columnar structure. For an acoustic wavevector perpendicular to the surface the exchanged wavevector is proportional to the cosine of the angle θ between the wavevector direction and the normal to the surface, and would lead to a frequency proportional to cosθ:

$$k_{\perp} \propto \cos\theta \Rightarrow f \propto \cos\theta \tag{6.6}$$

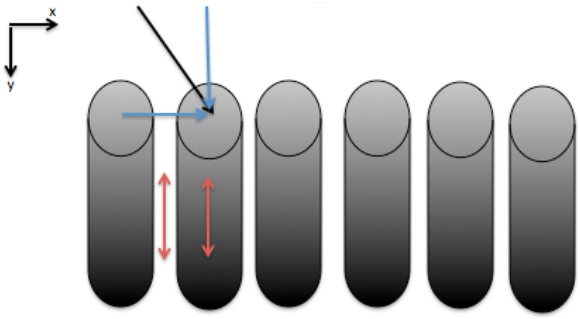


**Fig.6.28** Sketch of $TiO_2$ columnar structure with black arrows indicating the probed wavevector and blue arrows indicating its component. Red arrows indicate potential waves propagating in the y direction.

The columnar structure shown in figure 6.28 is made of ordered and independent cylindrical rods. As we have already said, this is only an approximation because the real microstructure of our samples is made of slightly conical rods which are connected at the bottom.

We indicate with $k_{\parallel 0}$ and $k_{\perp 0}$ the parallel and perpendicular components of the wavevector in the vacuum. In the same way, we indicate with $k_{\parallel f}$ and $k_{\perp f}$ the parallel and perpendicular components of the optical wavevector in the film (refractive index *n*).

The following relation is valid between those wavevector:

$$\sqrt{k_{\parallel f}^2 + k_{\perp f}^2} = n\sqrt{k_{\parallel 0}^2 + k_{\perp 0}^2} \tag{6.7}$$

The parallel components $k_{\parallel 0}$ and $k_{\parallel f}$ are the same: the parallel component remains unchanged upon refraction, while the perpendicular component $k_{\perp 0}$ becomes:

$$k_{\perp f} = k_f \cos\theta_f = nk_0 \cos\theta_f \tag{6.8}$$

where $\theta_f$ is the refraction angle in the film, related to the incidence angle $\theta_0$ in vacuum (air, $n_0$=1), by Snell's law:

$$\frac{\sin\theta_0}{\sin\theta_f} = \frac{n}{n_0} \Rightarrow \sin\theta_0 = n\sin\theta_f \tag{6.9}$$

We can compute $\cos\theta_f$ that appears in Equation 6.8 in the following way:

$$\cos\theta_f = \sqrt{1-\sin^2\theta_f} = \sqrt{1-\frac{\sin^2\theta_0}{n^2}} \tag{6.10}$$

If the exchanged wavevector $q_\perp$ is perpendicular to the surface (Equation 6.6) we have:

$$\begin{aligned} &f \propto k_{\perp f} \propto \cos\theta_f \Rightarrow f = vk_{\perp f} = vk_f\cos\theta_f = vk_f\sqrt{1-\frac{\sin^2\theta_0}{n^2}} = \\ &vnk_0\sqrt{1-\frac{\sin^2\theta_0}{n^2}} = vk_0\sqrt{n^2-\sin^2\theta_0} \Rightarrow \left(\frac{f}{k_0}\right)^2 = v^2\left(n^2-\sin^2\theta_0\right) \\ &f^2 = \left(k_0 v\right)^2\left(n^2-\sin^2\theta_0\right) \end{aligned} \tag{6.11}$$

The final relation written in Equation 6.11 can be rewritten as the equation of a line with negative slope, obtaining:

$$f^2 = \left(k_0 v\right)^2 n^2 - \left(k_0 v\right)^2 \sin^2\theta_0 = A - B\sin^2\theta_0 \tag{6.12}$$

where A and B are two constants whose values are

$$\begin{aligned} A &= \left(k_0 v\right)^2 n^2 \\ B &= \left(k_0 v\right)^2 \end{aligned} \tag{6.13}$$

Having observed that the considered trend is decreasing, we can fit the points with a linear trendline with an equation like the one of 6.12, knowing the values of the measured frequencies $f$ and the incidence angles $\sin\theta_0$. Figure 6.29 shows the graph obtained from the relation between $f^2$ and $\sin^2\theta$.

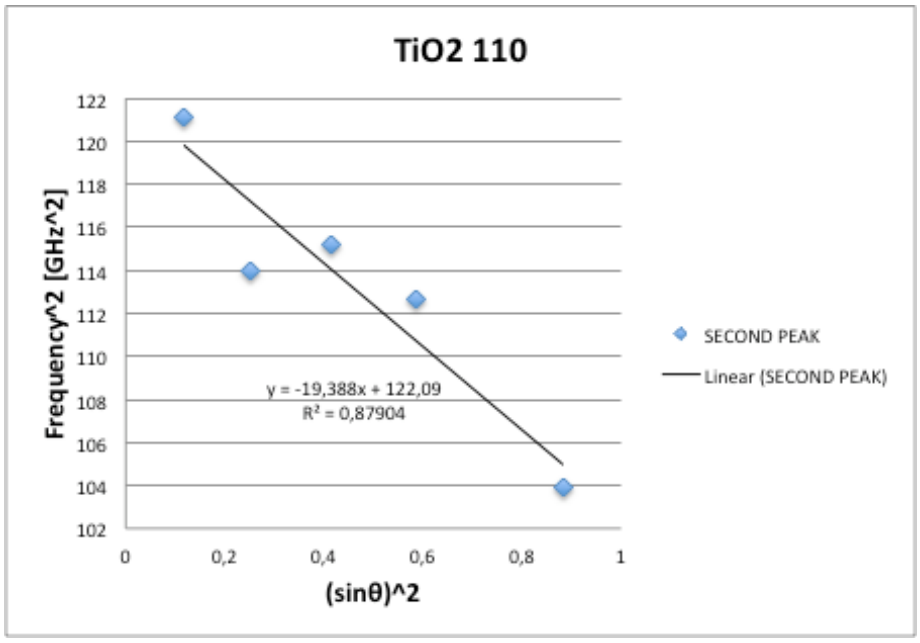


**Fig.6.29** Trend between squared measured frequencies and sinθ for $TiO_2$ 110 (see Equation 6.12).

From the trendline, which is of the kind of $f^2 = A\text{-}B\sin^2\theta$, we can extract the values of the constant A and B, of Equation 6.13, from which we can derive:

$$A = (k_0 v)^2 n^2 = Bn^2 \Rightarrow n^2 = \frac{A}{B} = \frac{122,09}{19,388} = 6,297 \Rightarrow n \cong 2,51$$

and

$$B = (2k_0 v / 2\pi)^2 \Rightarrow k_0 v = \pi\sqrt{B} \Rightarrow v = \frac{\pi}{k_0}\sqrt{B} = \frac{\lambda_0}{2}\sqrt{B} \Rightarrow$$

$$\Rightarrow v = \frac{514.5\ \text{nm}}{2} \times 4,40\ \text{GHz} = 1132\ \text{m/s}$$

We obtain a refractive index that is very similar to the one of $TiO_2$, the refractive indexes of rutile, anatase and brookite being 2,488, 2,53 and 2,61 respectively and a velocity of the acoustic mode which is of the same order of the acoustic

velocities in solids, but is lower, by a factor of about 4 than the probabale value of longitudinal bulk velocity in a reasonably compact film, as shown below. Free standing thin columns also support modes different from the purely compressive one, namely flexural modes, which are expected to have lower propagation velocities.

Also the trends of the peaks at about 10-11 GHz of both $TiO_2$ 111 and 112 in figures 6.16 and 6.21 seem to be decreasing, as shown in figure 6.30, and so probably associated to a wave which propagates along the column.

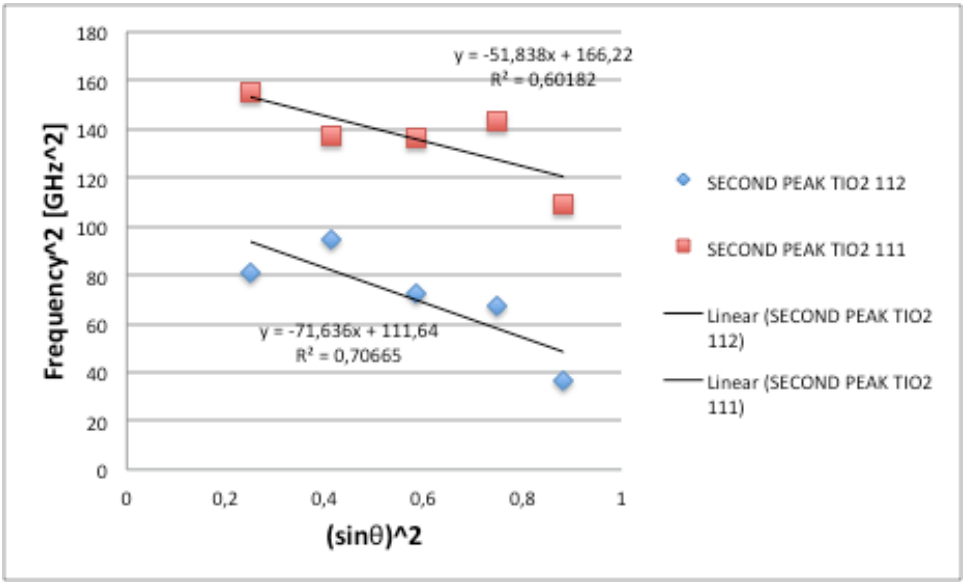


**Fig.6.30** Trend between squared measured frequencies and sinθ for $TiO_2$ 111 and $TiO_2$ 112 (see Equation 6.12).

Doing the same calculations that we have done for the case of $TiO_2$ 110, we obtain for $TiO_2$ 111:

$$A = (k_0 v)^2 n^2 = Bn^2 \Rightarrow n^2 = \frac{A}{B} = \frac{166,22}{51,838} = 3,21 \Rightarrow n \cong 1,80$$

and

$$B = (2k_0 v / 2\pi)^2 \Rightarrow k_0 v = \pi\sqrt{B} \Rightarrow v = \frac{\pi}{k_0}\sqrt{B} = \frac{\lambda_0}{2}\sqrt{B} \Rightarrow$$

$$\Rightarrow v = \frac{514.5 \text{ nm}}{2} \times 7,20 \text{ GHz} = 1852 \text{ m/s}$$

In the case of $TiO_2$ 112 we have:

$$A = (k_0 v)^2 n^2 = Bn^2 \Rightarrow n^2 = \frac{A}{B} = \frac{111,64}{71,636} = 1,56 \Rightarrow n \cong 1,25$$

and

$$B = (2k_0 v / 2\pi)^2 \Rightarrow k_0 v = \pi\sqrt{B} \Rightarrow v = \frac{\pi}{k_0}\sqrt{B} = \frac{\lambda_0}{2}\sqrt{B} \Rightarrow$$

$$\Rightarrow v = \frac{514.5 \text{ nm}}{2} \times 8,46 \text{ GHz} = 2176 \text{ m/s}$$

The refractive indexes obtained from this analysis tend to decrease as the pressure of deposition increases. This is a consistent result, because as the presure increases the film becomes less compact.

For what concerns the velocity values obtained, they tend to increase as the pressure of deposition increases. The reason of this trend is not clear. It must be remembered that in this analysis we are treating the film as an equivalent homogeneous film and the appropriateness of this model is questionable especially for the higher deposition pressures. Anyway, the orders of magnitude of the velocity values and of the refraction indexes are reasonable; a more detailed analysis would be obviously desirable.

In order to check the hypothesis of wave travelling along the columns, we performed a measurement in the symmetric forward scattering geometry (see chapter 3), in which the probed wavevector is exactly normal to the surface, but without managing to obtain meaningful results.

In the sample $TiO_2$ 109, a peak at high frequency, which could be associated to a bulk wave, has been observed. If we interpret it as due to a longitudinal bulk wave which propagates in the film (and we assume that the film is compact enough to support bulk waves travelling in any directions), we can evaluate the velocity of this wave as:

$$v = \frac{\omega}{k} = \frac{2\pi f}{2 \cdot \frac{2\pi n}{\lambda_0}} \Rightarrow vn = \frac{2\pi f \lambda_0}{2 \cdot 2\pi} = \frac{40 \times 10^9 (Hz) \cdot 514{,}5 \times 10^{-9} (m)}{2} = 10290 m/s$$

If we consider the value of $n \cong 2{,}51$ that we have just obtained, we have a velocity of the bulk wave of about 4000 m/s, close to those found in similar ceramic films.

### 6.2.2 Dispersion Relations

Unfortunately, it's not easy to say something certain about these peaks and their attribuition to acoustic waves, because we have seen that the trends of the same peak change between samples produced at different pressure, especially in the case of the fisrt peak (that is at about 3-4 GHz) and the second peak (that is at about 11 GHz).

Observing the trends of the peak at about 11 GHz of $TiO_2$ 109 (5 Pa) and of the first peak of $TiO_2$ 110 (7 Pa) in figure 6.25, we probably deal with surface waves, whose frequency depends on the incidence angle and scales as $\sin\theta$. We tried to derive dispersion relations of a film of $SiO_2$ with a Si substrate to compare it with those of a film of $TiO_2$ with a Si substrate. We use a tool of MATLAB program Brillo which, havig in input the density and the elastic constants of the material, gives as an output the dispersion relations of each mode supported by the film. The following figures show the results of this analysis: figure 6.31 and 6.32 contains the dispersion relation of a $SiO_2$ film on a Si substrate and figure 6.33 contains the dispersion relation of $TiO_2$ film on a Si

substrate. In the case of fugure 6.32 we show the dispersion relations of the Si substrate with a fictiscious film havig properties similar to $SiO_2$ but negligible stiffness.

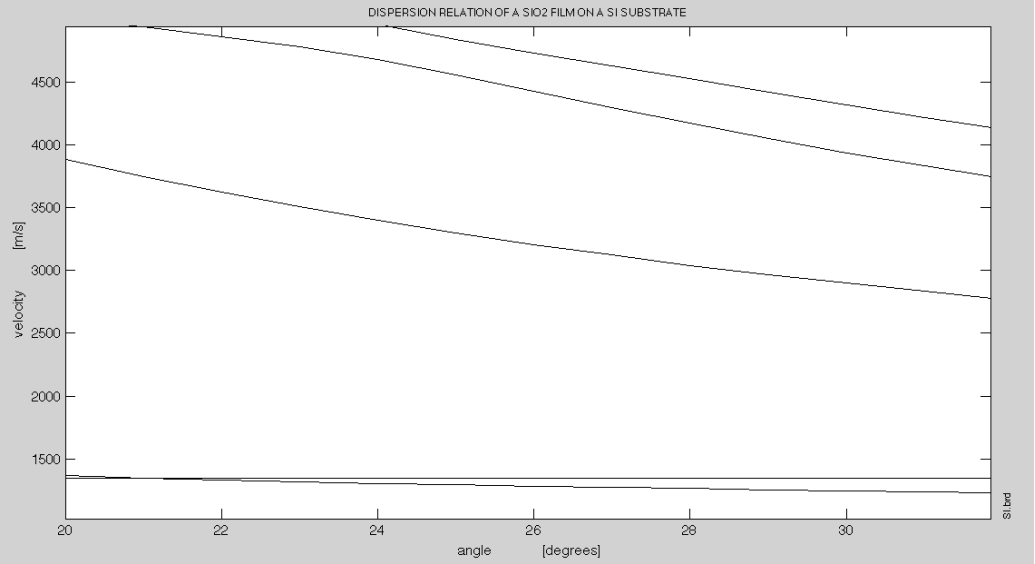


**Fig.6.31** Dispersion relation (velocity vs angle) of a film of $SiO_2$ (with negligible stiffness) on a Si substrate.

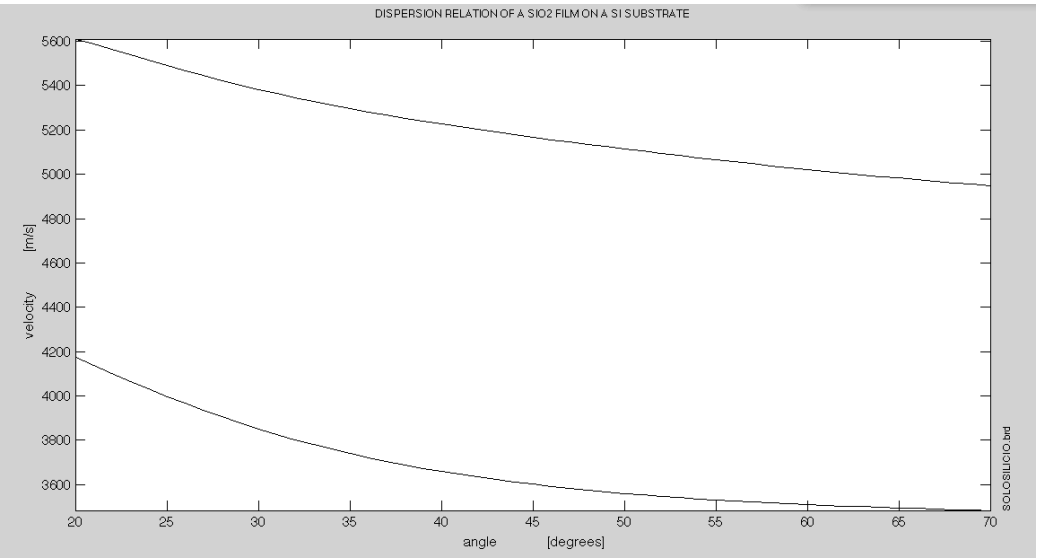

**Fig.6.32** Dispersion relation (velocity vs angle) of a film of $SiO_2$ on a Si substrate.

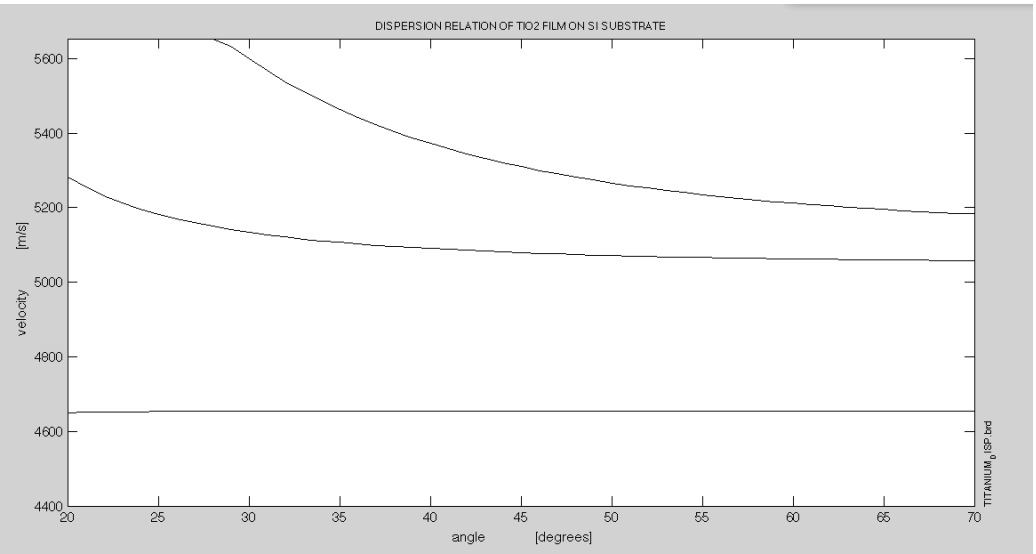


**Fig.6.33** Dispersion relation (velocity vs angle) of a film of $TiO_2$ on a Si substrate.

In the first two cases, we have a silica film and in the third case we have a $TiO_2$ film, whose elastic properties, E (GPa) and G (GPa), have been taken from the database of NIST (National Institute of Standards and Technology). Doing this operation we consider the films as isotropic and characterized by $C_{11}$, $C_{12}$ and $C_{44}$ constants. The relations between these constants are given by:

$$\begin{aligned} C_{44} &= G = \mu \\ C_{11} &= \lambda + 2\mu \\ C_{12} &= C_{11} - 2C_{44} \end{aligned} \qquad \textbf{(6.14)}$$

We obtain these constants knowing the relation between E, λ and μ, given below:

$$E = \frac{\mu(3\lambda + 2\mu)}{\lambda + \mu} \qquad \textbf{(6.15)}$$

In figure 6.31 we can observe a dispersion relation of the acoustic waves of the Si film whose velocities seem to be similar to those that we have measured in the analysis of the first peak sample $TiO_2$ 110 (7 Pa) of the order of 1400 m/s. We can think about the first peak of $TiO_2$ spectra as associated to a surface wave with lower velocity, as if this was the surface mode of silicon substrate but modified by a peculiar film. This film was modeled as a film having the mass denisty of a typical oxide but negliglible stiffness.

The next step could be the computation of the dispersion relations of an anisotropic film, with different properties in the three directions, in an hexagonal symmetry. If we think about our samples, they are more realistic anisotropic, with different properties between the directions parallel and perpendicular to the surface, being made of several columns slightly independent but all attacched at their bottom.

### 6.2.3 Polarizing the Light

Another attempt we made to estabilish the acoustic waves responsible of the observed peaks is focused on $TiO_2$ 109 (5 Pa), which is the only sample with three distinct peaks. The first peak at about 11 GHz has been the object of the analysis of the former paragraphs, and we think it is probably due to a surface wave. For what concerns the third peak at about 42 GHz, it has been observed only in this sample and has a high frequency that lead us to think that it could be related to a bulk wave. Anyway, we cannot affirm it for certain because this peak is not of sure attribuition, due to its unconventional width and shape and to the lack of similar peaks in other spectra.

This peak has a frequency which is relatively high and varies very little with the angle: both these characters point to a peak related to a bulk wave. The absence

of this peak in the spectra from the samples at higher pressure confirms our hypothesis. The sample at 5 Pa is the most compact one from the morphological point of view and it can support bulk waves, whose propagation becomes more difficult in less compact structures. We remember that SEM images taken on all the samples have shown that the columnar structure is made of almost cylindrical columns which are very close in $TiO_2$ 109 (5 Pa) but which tend to separate as the pressure of deposition increases.

Taking in consideration the second peak of $TiO_2$ 109, whose attribution is the most problematic one, we performed the polarization analysis of the scattered light by a polarizer filter.

We performed Brillouin measurements on $TiO_2$ 109 with the polarizer in "horizontal polarization" and in "vertical polarization", with respect to the direction of the eletric field. Since the incident light has a horizontal polarization (it is polarized in the incidence plane), detection of a peak whose polarization has changed to vertical would lead to attribuite this peak to scattering by a transverse wave. Peaks keeping the horizontal polarization are instead due to scattering by longitudinal waves.

Here we show the spectra obtained with the polarizer, in horizontal polarization and in vertical polarization respectively.

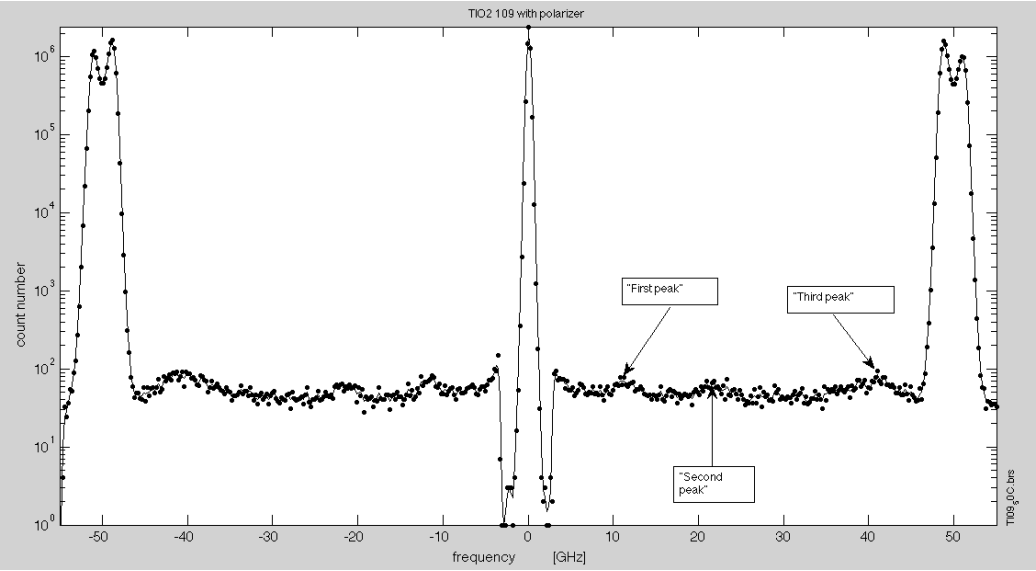


**Fig.6.34** $TiO_2$ 109 spectra obtained with the polarizer in horizontal position.

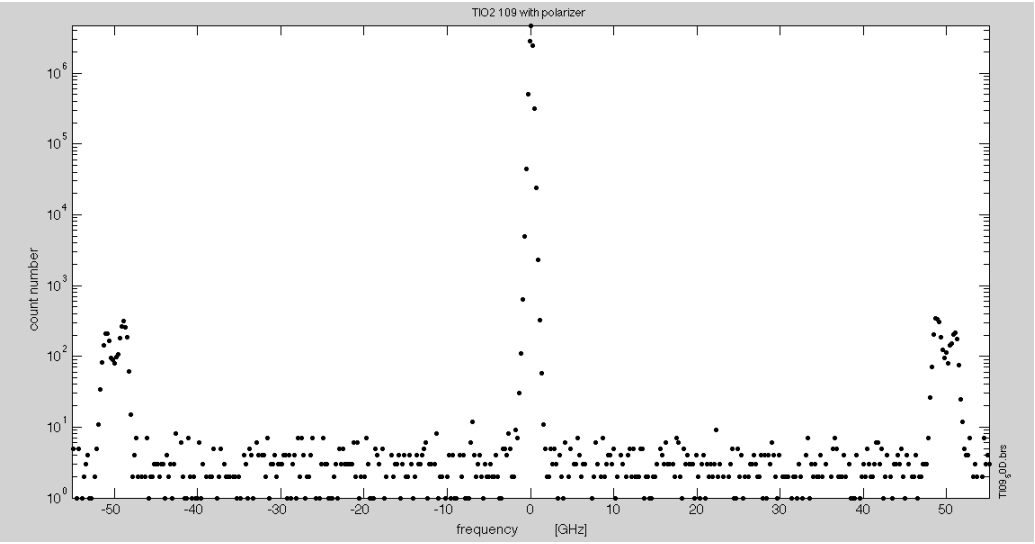


**Fig.6.35** $TiO_2$ 109 spectra obtained with the polarizer in vertical position.

Comparig the two figures above, it is easy to see that no peak has a transverse polarization because, changing the polarizer from horizontal to vertical polarization, none of the observed peaks survives. The acoustic waves coupled to both peaks seem to have longitudinal polarization but their nature is not clear.

Anyway, the most important fact we observed is that the two peaks at higher frequencies (those named here second and third peak) in $TiO_2$ 109 (5 Pa), disappear in the spectra recovered on the other samples produced at higher pressure. This macroscopic difference could be a proof of the fact that probably these peaks are coupled to bulk modes that can propagate in a compact structure such as that of $TiO_2$ 109 but not in a "broken" one such as that of the samples produced at higher pressure. In this latter case, in fact, the film structure becomes always more discontinuous in the direction parallel to the surface (the columns become more independent from each other).

### 6.2.4 Columnar Structure Modes: Approximation to Rod Vibration

The last observation of the previous chapter lead us to think about another possible explanation for the peaks we have observed. Having observed that our film has a columnar structure, the peaks at higher frequencies, especially the one at about 22 GHz, whose tentative of attribuition with the polarizer has given no results, could be associated with other kind of waves, not travelling waves but standing waves. In particular, in first approximation, we think about the natural vibrating modes, that can be both flexional and torsional, of a rod, an approximation of the column of the material structure. Actually, these aren't proper cylindrical columns but have a conical shape, as we have already mentioned above.

Considering the natural frequencies of vibration of a rod, we found in literature [23] their values calculated through the equation of motion. The results we report are referred to a circulr rod having a uniform cross section that can execute longitudinal and torsional vibrations. Also a lateral vibration is possible if the rod is long compared to its diameter. Our columns do not present a unifrom

cross section but we consider them as if they were rods with a diameter of about 100 nm and a length of 2 μm (that is more or less the thickness of our films). The solutions of equations of motion, that have the same form for longitudinal and torsional modes, are derived in the conditions of a fixed end and of a free end. This means that the boundadry conditions for this problem are $u$=0 (for a fixed end the dispalcement is zero ) and $u$'=0 (for a free end the stress is zero).

The calculated longitudinal and torsional vibrations are expressed in the following equations:

$$\omega_n = n\frac{\pi}{2l}\sqrt{\frac{Eg}{\rho}}$$
$$\omega_n = n\frac{\pi}{2l}\sqrt{\frac{Gg}{\rho}} \qquad \textbf{(6.16)}$$

where n=1,3,5,7,9…etc.

For a comparison purpose, we choose values for the elastic constants of $TiO_2$ from the site of NIST (National Institute of Standards and Technology): E=245 GPa, G=102 GPa. The mass density of $TiO_2$ ranges from 3800 to 4100 kg/m$^3$, depending on the relative percentages of rutile, anatase and brookite in the material composition. We don't know with precision these values for our sample, so we choose again the mass density given by the database of NIST: ϱ=4032 kg/m$^3$.

Table 6.3 and 6.4 below show the results obtained substituting our data in Equations 6.16:

| N | FREQ. LONG. [rad/s] | FREQ. LONG.[GHz] |
|---|---|---|
| 1 | 1,24E+10 | 1,97 |
| 3 | 3,71E+10 | 5,91 |
| 5 | 6,19E+10 | 9,85 |
| 7 | 8,66E+10 | 13,78 |
| 9 | 1,11E+11 | 17,72 |
| 11 | 1,36E+11 | 21,66 |
| 13 | 1,61E+11 | 25,60 |
| 15 | 1,86E+11 | 29,54 |
| 17 | 2,10E+11 | 33,48 |
| 19 | 2,35E+11 | 37,41 |
| 21 | 2,60E+11 | 41,35 |
| 23 | 2,85E+11 | 45,29 |
| 25 | 3,09E+11 | 49,23 |
| 27 | 3,34E+11 | 53,17 |
| 29 | 3,59E+11 | 57,11 |

**Table 6.3** Natural longitudinal frequencies of a vibrating rod with l=2x10$^{-6}$m. To pass from rad/s to GHz we use this conversion: $f$(Hz)= [$f$(rad/s)/(2*π)]*10$^{-9}$.

| N | FREQ. TOR. [rad/s] | FREQ. TOR. [GHz] |
|---|---|---|
| 1 | 1,92E+10 | 3,05 |
| 3 | 5,75E+10 | 9,16 |
| 5 | 2,88E+11 | 45,78 |
| 7 | 2,01E+12 | 320,45 |
| 9 | 1,81E+13 | 2884,03 |

**Table 6.4** Natural torsional frequencies of a vibrating rod with l=2x10$^{-6}$m. To pass from rad/s to GHz we use this conversion: $f$(Hz)= [$f$(rad/s)/(2*π)]*10$^{-9}$.

We underline in yellow the frequency values that are similar to those obtained from the fitting procedure we performed on the peaks. The values that approach

better the frequencies we have measured are those of the 11-, 13-,21- and 23-th mode of the longitudinal frequencies and that of 5-th mode of the torsional ones. Actually, the values of frequencies of the third peak of $TiO_2$ 109 (5 Pa) are centred around 41-42 GHz and those of the second peak are at about 22 GHz, so the most realistic values seem to be only those of the 11-th longitudinal mode (21,7 GHz) and the 21-th longitudinal mode (41,4) GHz.

It must be pointed out that these calculations are only useful to give an idea of the orders of magnitude of the natural frequencies of a vibrating rod to see if they are similar to the frequency values obtained from the fitting procedure performed on the spectra. We cannot explain why a mode or another should scatter and the other natural modes shouldn't. The interpretation in terms of the modes of a free standing column seems therefore not appropriate. It must also be rembered that SEM images show columns which are not ordered and independent but are instead conical and seem to be attached one to another at least at their bottom. So, there will be an interaction between columns that should be taken in consideration for a more precise and realistic calculation.

# Chapter 7

## Conclusions

This work is based on a measurement campaign conducted on two batches of nanostructured $TiO_2$ samples. These samples have been produced by the pulsed laser deposition (PLD) technique, with various level of background pressure in the deposition chamber (from 5 to 15 Pa). Their morphology, analysed by SEM images, is of the type expected for these deposition condition: a "columnar" structure, with columns of slightly conical shape. This structure has the expected dependence on the deposition pressure: with higher the pressure the columns progressively become more separate and independent, with less compact surfaces.

The vibrational characterization was performed by Brillouin scattering. A first set of measurements, performed on samples deposited with the same pressure of 10 Pa, checked the lateral uniformity of samples. The well known non uniform thickness of films produced by PLD without substrate motion was confirmed by the quantitative details, namely the spectral frequencies, of spectra which however remain very similar when the measurement position scans the specimen surface.

The second set of measurements aims at identifying the difference in the vibrational behaviour of the $TiO_2$ samples produced at different background pressures: $TiO_2$ 109 at 5 Pa, $TiO_2$ 110 at 7 Pa, $TiO_2$ 111 at 10 Pa and $TiO_2$ 112 at 15 Pa. In this limited range of pressure the morphology of the samples show gradual evolution, without qualitative changes. Strong differences were instead found in the vibrational behaviour, measured by Brilluoin spectroscopy.

The richest spectrum was found for the sample $TiO_2$ 109, deposited at the lowest considered pressure, 5 Pa. It is obviously the most compact of the considered samples, and its spectra present three distinct peak, at about 11 GHz, 22 GHz and 42 GHz. The two higher frequency peaks have an unusual shape, broad and asymmetric. Their frequency is almost insensitive to the incidence angle, and

the disappear in all the samples produced at higher pressures. These characters suggest that the film deposited at 5 Pa is still compact enough to support the bulk waves of a homogeneous medium, while the lower connection of films deposited at higher pressures no longer supports such waves. However the presence of two such peaks remains unexplained, also because polarization analysis showed that these peaks have the same polarization.

The lowest frequency peak of this spectrum, at about 11 GHz, is present also in all the other spectra. A further peak, at about 4 GHz, is also present in all the other spectra. In order to investigate the attribution of such peaks, their dependence on the incidence angle was investigated, finding surprising results.

The peak at about 11 GHz of $TiO_2$ 109 (5 Pa) and that at about 4 GHz of $TiO_2$ 110 (7 Pa), have a frequency which is almost proportional to $\sin\theta$. This is the peculiar signature of an acoustic mode travelling parallel to the surface. For the 11 GHz peak of the 5 Pa specimen, it can be proposed that the structure is compact enough to support bulk waves (giving the two peaks at higher frequency) and also a surface wave (giving this peak). For the 4 GHz peak of the 7 Pa specimen it was shown that it is compatible with a surface wave of the silicon substrate, modified by the deposited film, which having a low connectivity, adds significant contribution to inertia but a small contribution to stiffness. In both cases the measurements at different incidence angles give several measurements of essentially the same velocity.

Interestingly, the peaks appearing at almost the same frequencies in the other samples have a different dependence on the incidence angles, suggesting that they might be different origins, only accidentally giving peaks at similar frequencies.

The peaks at about 11 GHz of $TiO_2$ 110 (7 Pa), $TiO_2$ 111 (10 Pa) and $TiO_2$ 112 (15 Pa) all show a decreasing trend between frequency and incidence angle. This trend could be associated to a wave that does not travel parallel to the surface (whose frequencies scale as $\sin\theta$) but that travels along the columns, in a direction perpendicular to the sample thickness (in this case, frequencies would be proportional to $\cos\theta$, which decreases with the angle). Starting from this assumption, it was possible to establish a relation between the measured frequencies $f$ and the sine of the incidence angle $\theta$ which allows us to estimate

the refractive index *n*. We have obtained acceptable estimations of the refractive index of titanium dioxide, in particular in the case of $TiO_2$ 110 (7 Pa). The other two samples gave values of the refractive index lower than that obtained in the case of 7 Pa sample, but still reasonable. In particular we have observed a decreasing trend of the refractive index with the increase of pressure, a thing that agrees with the fact that, as pressure increases, the samples become less compact. The meaning of the velocitiues determined by this procedure is less clear, although their magnitudes are of the expected order of magnitude.

For both the samples $TiO_2$ 111 (10 Pa) and $TiO_2$ 112 (15 Pa) the peak at about 4 GHz has a frequency which depends only weakly on incidence angle suggesting an association to not travelling modes.

The complexity of the vibrational behaviour of a nanostructured film has made the peak attribution difficult, and many questions remain still open. However, even if the peak attribution is not completely certain, we have presented the efforts we have performed for the peaks attribution, which are based on the observed trends between frequencies and angles, the SEM images and the dispersion relations.

The most important thing that emerges from the performed measurements and from their analysis is the extreme sensitivity of Brillouin spectroscopy, which is able to detect evident differences in the vibrational behaviour of nanostructured films with only small differences in the pressure of deposition.

Brillouin spectroscopy could therefore be exploited to detect the consequences of small alterations of the parameters in the productive process, such as, in PLD, the pressure of deposition. This is a very challenging feature that renders this technique interesting in the analysis and characterization of those materials used in all the technological devices whose function and performance is strongly dependent on the morphological structure.

This work has highlighted interesting phenomena which could be developed in future works, investigating the strong connection between the vibrational behaviour and the sample structure.

# References

[1] T.Kundu, Ultrasonic nondestructive Evaluation, CRC Press (2005)

[2] Auld, B.A. Acoustic fields and waves in solids, R.E. Krieger Publishing Company (1990)

[3] Loudon et al., Comins (2001)

[4] M. G. Beghi, F. Di Fonzo, S. Pietralunga, C. Ubaldi and C. E. Bottani: *Precision and accurancy in film stiffness measurements by brillouin Spectroscopy*; Review Of Scientific Instruments 82, 000000 (2011)

[5] M.G. Beghi, A.G. Avery, V.Prakapenka, P.V. Zinin, Measurements of the Elastic Properties of Solids by Brillouin Spectroscopy, Ultrasonic nondestructive Evaluation, CRC Press (2005)

[6] Tandem Fabry Perot Interferometer Manual, JRS Scientific Instruments

[7] Ulrike Diebold: *The surface science of titanium dioxide;* Surface Science Reports 48, pp.53-229 (2003)

[8] A. Fujishima, K. Hashimoto, T. Watanabe: *TiO2 Photocatalysis: Fundamentals and Applications*; BKC Tokyo (1999)

[9] Marius Stamate, Gabriel Lazar: *Application Of Titanium Dioxide Photocatalysis To Create Self-Cleaning Materials*; Mocm 13, Volume 3, Romanian Technical Sciences Academy (2007 )

[10] K. Hashimoto,Hiroshi and Akira Fujishima: *TiO2 Photocatalysis: A Historical Overview and Future Prospects*; Japanese Journal of Applied Physics,Vol. 44, No. 12, pp. 8269–8285 (2005)

[11] S. A. Bilmes, P. Mandelbaum, F. Alvarez and N. M. Victori: *Surface and Electronic Structure of Titanium Dioxide Photocatalysts;* J. Phys. Chem. B 104, pp. 9851-9858 (2000)

[12] Daniel M. Blake, Pin-Ching Maness, Zheng Huang, Edward J. Wolfrum, and Jie Huang: *Application Of The Photocatalytic Chemistry Of Titanium Dioxide To Disinfection And The Killing Of Cancer Cells*; Separation and Purification Methods Volume 28(1), pp. 1-50 (1999)

[13] T.Watanabe, k.Hashimoto, A.Fujishima: *Photocatalytic purification and treatment of water and air*; Ed.D.F Oliis and H.Al-Ekabi (Elsevier , Amsterdam 1993)

[14] T.Watanabe, K.Hashimoto, K.Sunada: Environ.Sci.Technol.37 (2003) 4785

[15] T.Sugiura, T.Yoshida and H.Minoura: Electrochemistry 67 (1999) 1243

[16] Akira Fujishima, Tata N. Rao, Donald A. Tryk*: Titanium dioxide photocatalysis;* Journal of Photochemistry and Photobiology C: Photochemistry Reviews 1, pp.1–21 (2000)

[17] U. Diebold, M. Li, O. Dulub, E.L.D. Hebenstreit, W. Hebenstreit, Surf. Rev. Lett. 5±6 (2000) 613

[18] Yongxiang Li, Jürgen Hagen, Winfried Schaffrath, Peter Otschik, Dietrich Haarer: *Titanium dioxide films for photovoltaic cells derived from a sol–gel process*; Solar energy materials and solar cells, Vol. 56, Issue 2, pp. 164-175 (1999)

[19] Mingdeng Wei, Yoshinari Konishi, Haoshen Zhou, Masatoshi Yanagida, Hideki Sugihara and Hironori Arakawa: *Highly efficient dye-sensitized solar cells composed of mesoporous titanium dioxide*, *J. Mater. Chem.*, 16, pp.1287-1293 (2006)

[20] F.Huang, Y. Wang, J.Wu and X. Lu, Solar collectors and panels, Titanium dioxide nanomaterials: Basics and design, Synthesis and Application in solar energy utilization Techniques

[21] M.Gratzel: *Dye-sensitized solar cells*; Journal of Photochemistry and Photobilogy C: Photochemistry Rewiews, 4 pp. 145-153 (2003)

[22] C.E. Bottani, A. Li Bassi, M.G. Beghi, A. Podestà, P. Milani, A. Zakhidov, R. Baughman, D.A. Walters, R.E. Smalley: *Dynamic light scattering from acoustic modes in a single-walled carbon nanotubes*; Physical Rewiew B 67, 155407 (2003)

[23] W.F. Stokey Shock and Vibration Handbook (Ed C.M. Harris), Ch. 7, McGraw-Hill, New York (1996)